



Delft University of Technology

MASTER OF SCIENCE IN APPLIED GEOPHYSICS

RESEARCH THESIS

Imaging Angle-Dependent Reflectivity using the Marchenko Method

Hassan Saud Alfaraj

August 3, 2020

Imaging Angle-Dependent Reflectivity using the Marchenko Method

MASTER OF SCIENCE THESIS

for the degree of Master of Science in Applied Geophysics at
Delft University of Technology
by

Hassan Saud Alfaraj

August 3, 2020



Delft University of Technology

Copyright © 2020 by Delft University of Technology.

All rights reserved.

No part of the material protected by this copyright notice may be reproduced or utilized in any form or by any means, electronic or mechanical, including photocopying or by any information storage and retrieval system, without permission from this publisher.

Printed in The Netherlands

MASTER OF SCIENCE IN APPLIED GEOPHYSICS

Delft University of Technology, The Netherlands

Dated: *August 3, 2020*

Supervisor(s):

Prof. Kees Wapenaar

Joeri Brackenhoff

Committee Members:

Prof. Kees Wapenaar

Dr. Eric Verschuur

Dr. Deyan Draganov

Abstract

When reflection images are studied, often only the zero-offset reflectivity is considered, however, taking into account the angle-dependent reflectivity can add additional information about the Earth's subsurface. This additional information can be used to extract the properties of the subsurface using the amplitude variation with offset (AVO) analysis techniques. However, the presence of a complex overburden can significantly deteriorate the AVO response, especially for deep targets. To overcome this problem, the overburden effects can be removed by redatuming the reflection response at a depth level below the overburden. The Marchenko method has the potential to correctly retrieve the angle-dependent reflectivity in acoustic media without distortions due to multiple scattering caused by the overburden. The method estimates the downgoing and upgoing Green's functions of a virtual source located in the subsurface from surface reflection data and an estimate of the direct arrival from the location of the virtual source. The estimated Green's functions represent accurate upgoing and downgoing wavefields as they contain all orders of internal multiple reflections of the subsurface. These internal multiple reflections contribute to retrieving the reflectivity accurately in the redatumed reflection response. By deconvolving the retrieved upgoing Green's function with the downgoing Green's function, a new reflection response is obtained, with virtual sources and virtual receivers in the subsurface. The resultant reflection response is free of spurious events related to internal multiples in the overburden and contains the correct amplitudes. The angle-dependent reflectivity of the redatumed response can be obtained by summing the reflection coefficients along lines of constant ray parameter or angle. Potentially, the retrieved angle-dependent reflection coefficients obtained by this method can be used as input in a subsequent inversion process to obtain the velocity and density of the subsurface.

Acknowledgements

First, I would like to express the deepest appreciation to my supervisors Professor Kees Wapenaar and Joeri Brackenhoff, who gave me the opportunity to do this work, which also helped me in doing a lot of research and I came to know about so many new aspects in the field of Applied Geophysics. I am really thankful to them. Special thanks of gratitude to Joeri Brackenhoff, who have been very friendly and easy to communicate. You have been very supportive of my work and were helpful whenever I was stuck.

I also thank my parents, who always encourage me to continue my study, and also my wife who has been very supportive and patient during my study at TU Delft. Without their encouragement and support I could not achieve my goal. I would also like to thank my sponsor, Saudi Aramco, for giving me the opportunity to pursue a Master's Degree in Geophysics.

I also owe many thanks to Professor Evert Slob who helped me in designing my own self-composed Applied Geophysics program, which allowed me to extend my thesis into one year. I also thank Dr. Jan Thorbecke and Dr. Deyan Draganov, who allowed me to have discussion with them about the codes they developed.

Delft University of Technology

Hassan Saud Alfaraj

August 3, 2020

Table of Contents

Abstract	v
Acknowledgements	vii
1 Introduction	1
2 Marchenko method	7
2-1 Notations and Fourier transforms	7
2-2 Green's function	7
2-3 Focusing function	11
2-4 The coupled Marchenko equations	15
2-5 Marchenko redatuming	18
3 Imaging angle-dependent reflectivity	23
3-1 Properties of the angle-dependent reflectivity	23
3-2 Imaging principle	27
4 Numerical examples	35
4-1 Imaging reflectivity in the presence of a complex overburden	36
4-2 Imaging reflectivity in a medium with varying velocity and density	40
4-3 Imaging reflectivity in the presence of a low-velocity layer.	52
4-4 Imaging reflectivity using an inaccurate density model	53
4-5 Imaging reflectivity using an inaccurate velocity model	53
4-6 Imaging reflectivity using smooth velocity and density models	65
4-7 Imaging reflectivity in the presence of random noise	69
4-8 Imaging reflectivity in an invisible medium	69
4-9 Imaging reflectivity in the presence of a dipping interface	72

5 Discussion and Conclusion	81
Bibliography	83
A Derivation	87
A-1 Derivation of the Shuey approximation in acoustic media	87
B Monopole-to-dipole conversion	89
C Deconvolution and stabilization	91
D Amplitude picking procedure	95
E Matlab scripts	97
E-1 1D Marchenko	97
E-1-1 Marchenko redatuming in 1D	97
Forward modelling	97
Ricker wavelet	98
1D Marchenko	99
E-2 Imaging angle-dependent reflectivity	99
E-2-1 Mapping the wavenumber into the angle domain	99
E-2-2 Mapping the wavenumber into the ray parameter domain	101
E-2-3 Imaging condition	103

List of Figures

1-1	Estimated acoustic AVO response in two cases: a homogeneous overburden (Column A) and a high-contrast overburden (Column B). Top row: density model with a background velocity of 1500 m/s. The source (white star) and receivers (black triangles) are located at the surface. The target is located at 1100 m. Middle row: surface reflection response. Note that the yellow arrow in case (B) indicates the primary reflection of the target which corresponds to the one in case (A). Bottom row: AVO response of the target, obtained by estimating the envelope.	3
1-2	Marchenko redatuming in 1D with a constant velocity of 1800 m/s. The dashed line represents the redatuming level. (A) Density model. (B) Reflection response with a source and receiver located at the surface. A Ricker wavelet has been used as a source wavelet with a peak frequency of 10 Hz. (C) Zoomed version of the zone of interest in (B). (D) Marchenko-based redatumed response (dashed red), standard-based redatumed response (dotted blue), and direct modeling (dashed black). Both redatumed responses were obtained by deconvolution.	5
1-3	Image of the zone of interest in Figure 1-2. The image was produced by extracting the zero-time component from the redatumed response at every depth level, with a step size of 1 m. (A) Marchenko imaging. (B) Standard imaging. The red arrows indicate the effects of the overburden. Note that these effects have been removed by the Marchenko method. Also, the amplitude is preserved at the depth of each reflector.	5
2-1	Classic Green's function. (A) The causal Green's function. The star represents a source point located at \mathbf{x}''_0 whereas the triangle represents an observation point (receiver) located at \mathbf{x} . The medium is enclosed by boundary S . The arrows represent the direction of the wavefields. (B) The anti-causal Green's function obtained by the principle of time reversal. Here, location \mathbf{x} is interpreted as a source point while location \mathbf{x}''_0 is interpreted as an observation point.	9
2-2	Single-sided acquisition surface, with a source point (white star) located at \mathbf{x}''_0 and receivers (black triangles) at \mathbf{x}_0 . The black dashed line on the top represents the transparent surface whereas the dotted line represents the arbitrary depth level.	9
2-3	Single-sided Green's function in an inhomogeneous medium due to a source point (star) located at \mathbf{x}''_0 . The Green's function is described by four components as shown here. The solid black lines represent interfaces. Note that the dashed arrows above the source represent the field propagating to the homogeneous half-space.	10
2-4	Illustration of the two states that are explained in the main text. (A) State A. (B) state B.	13

2-5	Illustration of the focusing function in the truncated medium. The black dashed and dotted lines represent $\partial\mathbb{D}_0$ and $\partial\mathbb{D}_i$, respectively. The black solid lines represent interfaces. (A) Initiating f_1^+ by sending f_{1d}^+ (cyan) from the surface to the focal point (solid circle) at \mathbf{x}'_i . (B) Generation of f_1^- (purple) as the response of the truncated medium to f_{1d}^+ . (C) Generation of spurious events (dashed purple and cyan) due to the propagation of f_1^- . (D) Scattering coda M^+ (yellow) is sent to cancel these spurious events. The focusing function f_1^+ is composed of the cyan and yellow events.	14
2-6	The Green's function $G^{-,+}$ (green) as the response of f_1^+ (cyan+yellow). The purple arrows represent f_1^-	14
2-7	The Green's function $G^{-,-}$ (red) and the time-reversed f_1^+ (cyan+yellow) as the response of the time-reversed f_1^- (purple). Note that the dashed (cyan+red) arrows represent the overlap between $G^{-,-}$ and the time-reversed f_1^+	15
2-8	The definition of the mute window Θ . The vertical dotted lines represent the arrival time t_d while the vertical dashed lines represent the limits of the mute window Θ after applying the positive constant ϵ . Note that the difference between the dashed and dotted lines is half the duration of the wavelet. The wavelet used here is a Ricker wavelet with a peak frequency of 10 Hz. In this case, the operator Θ will mute f_{1d}^+ (cyan), $G^{-,-}$ (red), $G^{-,+}$ (green) and pass f_1^- (purple) and M^+ (yellow).	16
2-9	Illustration of the stationary points. (A) Reflection response (blue) due to a source (white star) located at $\partial\mathbb{D}_0$. The triangles represent the acquisition surface at $\partial\mathbb{D}_0$. The black solid circles represent focal points at $\partial\mathbb{D}_i$, while the purple ones represent stationary points at $\partial\mathbb{D}_0$ that are outside the acquisition surface. (B) The retrieved parts (solid green) and lost parts (dotted green) of function $G^{-,+}$	17
2-10	Source-receiver reciprocity theorem. (A) $G^{-,+}$ (green) and $G^{-,-}$ (red) are the responses of a source point located at \mathbf{x}'_i and observed at \mathbf{x}''_0 . (B) $G^{-,+}$ (green) and $G^{+,+}$ (red) are the responses of source points located at \mathbf{x}''_0 and observed at \mathbf{x}'_i	20
2-11	Illustration of the source-receiver redatuming using MDD. (A) Surface reflection response. (B) Redatumed reflection response. Note that the overburden has been completely removed.	21
3-1	Reflection of an incident downgoing plane wave at an interface (horizontal line) between two acoustic homogeneous half-spaces. The arrow represents the path of the wave. The vertical dashed line represents the normal. Snell's law describes the relationship between the angles of incidence θ_1 and transmission θ_2	24
3-2	A refracted wave that enters and leaves a high-velocity medium at the critical angle is known as a head wave. Here, the angle of refraction approaches 90^0 , at which the refracted ray becomes parallel to the interface. Beyond the critical angle, the lower half-space supports an evanescent wave only.	24
3-3	Reflection coefficient in angle domain. (A) Angle-dependent reflectivity with $c_1 < c_2$. Note that the evanescent wave occurs after θ_c with amplitude of 1. (B) Angle-dependent reflectivity with $c_1 > c_2$. Only the moduli have been plotted.	25
3-4	Reflection operator in the wavenumber-frequency domain with $c_1 < c_2$. (A) The modulus of \tilde{r} for a single-frequency of $f = 70$ Hz. The total reflection occurs for $k_2 < k_x < k_1$ with amplitude of 1. The evanescent wavefield occurs for all $ k_x > k_1$. (B) Wavenumber-frequency spectrum of the reflection operator. Note that the total reflection occurs within the yellow area with amplitude of 1. Only the moduli have been plotted.	26
3-5	Reflection operator in the wavenumber-frequency domain with $c_1 > c_2$. (A) The modulus of \tilde{r} for a single-frequency of $f = 70$ Hz. The total reflection occurs for $k_1 < k_x < k_2$ with amplitude of 1. The evanescent wavefield occurs for all $ k_x > k_2$. (B) Wavenumber-frequency spectrum of the reflection operator. Note that the total reflection occurs within the yellow area with amplitude of 1. Only the moduli have been plotted.	26

3-6	Reflection operator in the ray-parameter domain. (A) The modulus of \check{r} with $c_1 < c_2$. The total reflection occurs for $1/c_2 < p < 1/c_1$ with amplitude of 1. The evanescent wavefield occurs for all $ p > 1/c_1$. (B) The modulus of \check{r} with $c_1 > c_2$. The total reflection occurs for $1/c_1 < p < 1/c_2$ with amplitude of 1. The evanescent wavefield occurs for all $ p > 1/c_2$	27
3-7	Mapping the variable k_x into ray parameter p using a linear interpolation process. (A) Wavenumber-frequency domain with $c_1 = 1500$ m/s, $c_2 = 2000$ m/s, $\rho_1 = 1000$ kg/m ³ , and $\rho_2 = 1500$ kg/m ³ . (B) Ray-parameter-frequency domain obtained by the mapping process explained in the main text. Only the moduli have been plotted.	30
3-8	Mapping the variable k_x into angle θ using a linear interpolation process. (A) Wavenumber-frequency domain with $c_1 = 1500$ m/s, $c_2 = 2000$ m/s, $\rho_1 = 1000$ kg/m ³ , and $\rho_2 = 1500$ kg/m ³ . (B) Angle-frequency domain obtained by the mapping process explained in the main text. Only the moduli have been plotted.	31
3-9	Summation of all positive frequency components along lines of constant (A) wavenumber and (B) ray parameter. Note that the reflectivity is preserved in (B) whereas it is distorted in (A). These results are based on Figure 3-7.	31
3-10	Summation of all positive frequency components along lines of constant (A) wavenumber and (B) angle. Note that the reflectivity is preserved in (B) whereas it is distorted in (A). These results are based on Figure 3-8.	32
3-11	Imaged angle-dependent reflectivity for a two-layer acoustic medium with $c_1 = 1500$ m/s, $c_2 = 2000$ m/s, $\rho_1 = 1000$ kg/m ³ , and $\rho_2 = 1500$ kg/m ³ . The reflector is located at 400m. The imaging process has been applied with a depth step of 5m. (A) Image of the real part. Note that the polarity is positive. (B). Image of the imaginary part. (C) Image of the moduli.	32
3-12	Estimated angle-dependent reflectivity obtained by picking procedure along the event in Figure 3-11C. The polarity is derived from Figure 3-11A. Note that the estimated reflectivity (dashed red) matches the exact one (solid black) very well up to the critical angle.	33
4-1	The workflow of imaging angle-dependent reflectivity using the Marchenko method. (A) Imaging based on the MDD. (B) Imaging based on the spectral division. Note that FFT stands for fast Fourier transform.	37
4-2	Source wavelet with a flat frequency spectrum between $f_{min} = 5$ Hz and $f_{max} = 80$ Hz. (A) Time domain. (B) Frequency domain.	38
4-3	A Laterally invariant medium with a complex overburden. (A) Density model. (B) Velocity model. Note that the velocity is constant here.	38
4-4	Modeled reflection data $R(\mathbf{x}''_0, \mathbf{x}_0, t)$ of the medium in Figure 4-3 with a source located at the surface and (A) $x = -2500$ m, (B) $x = 0$ m, and (C) $x = 2500$ m.	39
4-5	Modeled direct arrivals $G_d(\mathbf{x}''_0, \mathbf{x}'_i, t)$ from (I) $z_i = 400$ m, (II) $z_i = 700$ m, and (III) $z_i = 1100$ m. The (A) density model and (B) velocity model are extracted from the models in Figure 4-3. The red asterisks and blue triangles indicate the locations of the sources and receivers, respectively. Note that the truncated velocity media are the same as the actual medium because the velocity is homogeneous in this example. (C) Source located at $x = -2500$ m. (D) Source located at $x = 0$, (E) Source located at $x = 2500$ m.	41
4-6	Focusing functions estimated in a medium with a complex overburden. The focal point is located at $x = 0$ and (I) $z_i = 400$ m, (II) $z_i = 700$ m, and (III) $z_i = 1100$ m. (A) $G_d(\mathbf{x}''_0, \mathbf{x}'_i, -t)$. (B) $f_1^+(\mathbf{x}''_0, \mathbf{x}'_i, t)$. (C) $f_1^-(\mathbf{x}''_0, \mathbf{x}'_i, t)$. The horizontal dashed line indicates $t = 0$. Note that $f_1^+(\mathbf{x}''_0, \mathbf{x}'_i, t)$ in (III-B) consists of two events which correspond to G_d and M^+	42

- 4-7 Comparison between the Marchenko and standard methods in estimating the Green's functions with a complex overburden. The focal point is located at $x = 0$ and (I) $z_i = 400$ m, (II) $z_i = 700$ m, and (III) $z_i = 1100$ m. (A) Marchenko $G^{\rightarrow,+}$. (B) Standard $G^{\rightarrow,+}$. (C) Marchenko $G^{\rightarrow,-}$. (D) Standard $G^{\rightarrow,-}$. Note the desired events obtained by the Marchenko method and the artefacts existing in the standard method. For deeper reflectors, the Marchenko method retrieves more than one event in $G^{\rightarrow,-}$ 43
- 4-8 The redatumed reflection response $R(\mathbf{x}_i, \mathbf{x}'_i, t)$ in the presence of a complex overburden. The virtual source is located at $x = 0$ and (I) $z_i = 400$ m, (II) $z_i = 700$ m, and (III) $z_i = 1100$ m. (A) Marchenko redatuming. (B) Standard redatuming. (C) AVO response obtained by estimating the envelope from (A) and (B). 44
- 4-9 Applying the mapping process on $R(\mathbf{x}_i, \mathbf{x}'_i, t)$ which is estimated in a medium with a complex overburden. The focal point is located at $x = 0$ and (I) $z_i = 400$ m, (II) $z_i = 700$ m, and (III) $z_i = 1100$ m. (A) Wavenumber-frequency domain. (B) Angle-frequency domain. (C) Ray parameter-frequency domain. Only the moduli have been plotted. . . . 45
- 4-10 The angle-dependent reflectivity obtained by the Marchenko and standard redatuming methods in a medium containing a complex overburden. (I) $z_i = 400$ m. (II) $z_i = 700$ m. (III) $z_i = 1100$ m. (A) Reflectivity as a function of angle. (B) Reflectivity as a function of ray parameter. 46
- 4-11 The angle-dependent reflectivity at $z_i = 1100$ with different iteration numbers. Note that the reflectivity is correctly retrieved at $k = 10$, which represents the maximum iteration number at this depth level. 47
- 4-12 Estimated $G^{\rightarrow,+}$ in a medium with a complex overburden. (A) $\mathbf{x}'_i = (-1500 \text{ m}, 1100 \text{ m})$. (B) $\mathbf{x}'_i = (0, 1100 \text{ m})$. (C) $\mathbf{x}'_i = (1500 \text{ m}, 1100 \text{ m})$. Note that $G^{\rightarrow,+}$ is completely retrieved in (B), while it is not in (A) and (C) due the stationary points. The yellow arrows indicate the missing parts. 47
- 4-13 Applying the mapping process on $G^{\rightarrow,+}$ and $G^{\rightarrow,-}$ which are estimated in a medium with a complex overburden. The focal point is located at $x = 0$ and (I) $z_i = 400$ m, (II) $z_i = 700$ m, and (III) $z_i = 1100$ m. (A) First arrival of $\tilde{G}^{\rightarrow,+}(k_x, z_i, \omega)$. (B) First arrival of $\tilde{G}^{\rightarrow,-}(k_x, z_i, \omega)$. (C) Spectral division. (D) Angle-frequency domain. (E) Ray parameter-frequency domain. Only the moduli have been plotted. 48
- 4-14 The angle-dependent reflectivity obtained by the spectral division and MDD in a medium containing a complex overburden. (I) $z_i = 400$ m. (II) $z_i = 700$ m. (III) $z_i = 1100$ m. (A) Reflectivity as a function of angle. (B) Reflectivity as a function of ray parameter. 49
- 4-15 The effect of the mute window Θ (yellow dashed hyperbola) on the retrieval of $G^{\rightarrow,-}(\mathbf{x}''_0, \mathbf{x}'_i, t)$. (A) $\mathbf{x}'_i = (-2500 \text{ m}, 1100 \text{ m})$. (B) $\mathbf{x}'_i = (0, 1100 \text{ m})$. (C) $\mathbf{x}'_i = (2500 \text{ m}, 1100 \text{ m})$ 50
- 4-16 Real part of the angle-dependent reflectivity as a function of depth with the presence of a complex overburden. (A) First reflector. (B) Second reflector. (C) Third reflector. Note that the real part shows the polarity of the reflectivity, with white as a negative polarity and black as a positive polarity. 50
- 4-17 Imaginary part of the angle-dependent reflectivity as a function of depth with the presence of a complex overburden. (A) First reflector. (B) Second reflector. (C) Third reflector. . . . 51
- 4-18 Modulus of the angle-dependent reflectivity as a function of depth with the presence of a complex overburden. (A) First reflector. (B) Second reflector. (C) Third reflector. Note that the first and second reflectors show very high contrasts associated with the complex overburden. 51
- 4-19 A Laterally invariant medium with varying density and velocity. (A) Density model. (B) Velocity model. 52
- 4-20 Modeled reflection data $R(\mathbf{x}''_0, \mathbf{x}_0, t)$ of the medium in Figure 4-19 with a source located at the surface and (A) $x = -2500$ m, (B) $x = 0$ m, and (C) $x = 2500$ m. The yellow arrows highlight the head waves, observed from around $t = 1$ s and $x = \pm 850$ m. . . . 53

4-21	Estimated Green's and focusing functions in a medium with varying density and velocity. The focal point is located at $x = 0$ and (I) $z_i = 400$ m, (II) $z_i = 700$ m, and (III) $z_i = 1100$ m. (A) $f_1^-(\mathbf{x}_0'', \mathbf{x}_i', t)$. (B) $f_1^+(\mathbf{x}_0'', \mathbf{x}_i', t)$. (C) $G^{-,+}(\mathbf{x}_0'', \mathbf{x}_i', t)$. (D) $G^{-,-}(\mathbf{x}_0'', \mathbf{x}_i', t)$. The horizontal dashed line indicates $t = 0$	54
4-22	Applying the mapping process on $R(\mathbf{x}_i, \mathbf{x}_i', t)$ which is estimated in a medium with varying density and velocity. The focal point is located at $x = 0$ and (II) $z_i = 700$ m, and (III) $z_i = 1100$ m. (A) Wavenumber-frequency domain. (B) Angle-frequency domain. (C) Ray parameter-frequency domain. Only the moduli have been plotted. Note that in (I) and (III) the spectra are not flat because of the velocity contrasts.	55
4-23	The angle-dependent reflectivity obtained by the Marchenko and standard redatuming methods in a medium with varying density and velocity. (I) $z_i = 400$ m. (II) $z_i = 700$ m. (III) $z_i = 1100$ m. (A) Reflectivity as a function of angle. (B) Reflectivity as a function of ray parameter.	56
4-24	Applying the mapping process on $G^{-,+}$ and $G^{-,-}$ which are estimated in a medium with varying density and velocity. The focal point is located at $x = 0$ and (I) $z_i = 400$ m, (II) $z_i = 700$ m, and (III) $z_i = 1100$ m. (A) First arrival of $\tilde{G}^{-,+}(k_x, z_i, \omega)$. (B) First arrival of $\tilde{G}^{-,-}(k_x, z_i, \omega)$. (C) Spectral division. (D) Angle-frequency domain. (E) Ray parameter-frequency domain. Only the moduli have been plotted.	57
4-25	The angle-dependent reflectivity obtained by the spectral division and MDD in a medium with varying density and velocity. (I) $z_i = 400$ m. (II) $z_i = 700$ m. (III) $z_i = 1100$ m. (A) Reflectivity as a function of angle. (B) Reflectivity as a function of ray parameter.	58
4-26	Real part of the angle-dependent reflection coefficient as a function of depth in a medium with varying density and velocity. (A) First reflector. (B) Second reflector. (C) Third reflector. The vertical dashed line indicates the critical angle.	59
4-27	Imaginary part of the angle-dependent reflection coefficient as a function of depth in a medium with varying density and velocity. (A) First reflector. (B) Second reflector. (C) Third reflector. The vertical dashed line indicates the critical angle.	59
4-28	Modulus of the angle-dependent reflection coefficient as a function of depth in a medium with varying density and velocity. (A) First reflector. (B) Second reflector. (C) Third reflector. The vertical dashed line indicates the critical angle.	60
4-29	A Laterally invariant medium with a low-velocity layer. (A) Density model. (B) Velocity model.	60
4-30	The angle-dependent reflectivity obtained by the spectral division and MDD at the low-velocity layer. (A) Reflectivity as a function of angle. (B) Reflectivity as a function of ray parameter.	61
4-31	Image of the angle-dependent reflectivity for a reflector located above a low-velocity layer. (A) Real part. (B) Imaginary part. (C) Modulus.	61
4-32	The models from which the reflection data are modeled in section 4-4. (A) Correct density model. (B) Correct velocity model.	62
4-33	The models from which the truncated media are extracted in section 4-4. (A) Wrong density model. (B) Correct velocity model.	62
4-34	Comparison between the direct arrivals estimated from the wrong density model and correct density model. (A) The response of the direct arrival. (B) The AVO response of the direct arrival. The focal point is located at $x = 0$ and (I) $z_i = 400$ m, (II) $z_i = 700$ m, (III) $z_i = 1100$ m. Note that there is a significant difference in amplitude between the correct and wrong direct arrivals.	63
4-35	The angle-dependent reflectivity obtained using the direct arrivals modeled in the wrong density model and correct density model. The virtual source is located at (I) $z_i = 400$ m, (II) $z_i = 700$ m, and (III) $z_i = 1100$ m. (A) Reflectivity as a function of angle. (B) Reflectivity as a function of ray parameter.	64
4-36	The models from which the truncated media are extracted in section 4-5. (A) Correct density model. (B) Wrong velocity model.	65

4-37 Comparison between the direct arrivals estimated from the wrong velocity model and correct velocity model. The focal point is located at $x = 0$ and $z_i = 1100$ m. (A) Direct arrival based on a correct velocity model. (B) Direct arrival based on a wrong velocity model. (C) Projection of the travel time from (A) and (B). The blue curve refers to the incorrect velocity model while the red curve refers to the correct velocity model. (D) Amplitude of the direct arrival as a function of offset.	66
4-38 Real part of the angle-dependent reflection coefficient as a function of depth obtained using direct arrivals modeled from a wrong velocity model. (A) First reflector. (B) Second reflector. (C) Third reflector. The horizontal yellow dashed line represents the true depth of the reflector.	66
4-39 Imaginary part of the angle-dependent reflection coefficient as a function of depth obtained using direct arrivals modeled from a wrong velocity model. (A) First reflector. (B) Second reflector. (C) Third reflector. The horizontal yellow dashed line represents the true depth of the reflector.	67
4-40 Modulus of the angle-dependent reflection coefficient as a function of depth obtained using direct arrivals modeled from a wrong velocity model. (A) First reflector. (B) Second reflector. (C) Third reflector.	67
4-41 The angle-dependent reflectivity obtained using the direct arrivals modeled in the wrong velocity model and correct velocity model. (I) First reflector. (II) Second Reflector. (III) Third reflector. (A) Reflectivity as a function of angle. (B) Reflectivity as a function of ray parameter.	68
4-42 Smooth version of the density and velocity models in Figure 4-19. A moving average filter of length 100 m has been applied. (A) Density model. (B) velocity model.	69
4-43 Real part of the angle-dependent reflection coefficient as a function of depth obtained using direct arrivals modeled from smooth density and velocity models. (A) First reflector. (B) Second reflector. (C) Third reflector. The horizontal yellow dashed line represents the true depth of the reflector. Note that at the second reflector, the event starts curving up at the very fat angles, while it is curving down in the third reflector. Also, the third reflector is located 10 m below the true depth.	70
4-44 Modulus of the angle-dependent reflection coefficient as a function of depth obtained using direct arrivals modeled from smooth density and velocity models. (A) First reflector. (B) Second reflector. (C) Third reflector. The vertical dashed line indicates the critical angle. 70	70
4-45 The angle-dependent reflectivity obtained using the direct arrivals modeled in the smooth models and correct models. (I) First reflector. (II) Second Reflector. (III) Third reflector. (A) Reflectivity as a function of angle. (B) Reflectivity as a function of ray parameter.	71
4-46 The modeled reflection response in Figure 4-20 after adding noise with SNR of 20 dB and Gaussian distribution. The source is located at the surface and (A) $x = -2500$ m, (B) $x = 0$, and (C) $x = 2500$ m.	72
4-47 The angle-dependent reflectivity in the presence of random noise. (I) $z_i = 400$ m. (II) $z_i = 700$ m. (III) $z_i = 1100$ m. (A) Reflectivity as a function of angle. (B) Reflectivity as a function of ray parameter.	73
4-48 Invisible medium with a constant layer thickness of 200 m. (A) Density model. (B) velocity model.	74
4-49 The modeled reflection response of the invisible medium. Note that only the primary reflection of the first two reflectors are visible. The source is located at the surface and (A) $x = -2500$ m, (B) $x = 0$, and (C) $x = 2500$ m.	74
4-50 Redatumed reflection response $R(\mathbf{x}_i, \mathbf{x}'_i, t)$ obtained by the Marchenko method in the invisible medium. The virtual source is located at $x = 0$ and (A) $z_i = 200$ m, (B) $z_i = 400$ m, (C) $z_i = 600$ m, (D) $z_i = 800$ m, (E) $z_i = 1000$ m, and (F) $z_i = 1200$ m.	75
4-51 Angle-dependent reflectivity obtained by the Marchenko method in the invisible medium. (A) $z_i = 200$ m, (B) $z_i = 400$ m, (C) $z_i = 600$ m, (D) $z_i = 800$ m, (E) $z_i = 1000$ m, and (F) $z_i = 1200$ m.	75

4-52	Dipping interface in a medium with constant velocity and varying density. (A) Density model. (B) velocity model.	76
4-53	The modeled reflection response in the presence of a dipping interface (see Figure 4-52). The source is located at the surface and (A) $x = 2500\text{m}$, (B) $x = 0$, and (C) $x = 2500\text{m}$. Note the reflection response is asymmetric and the zero-offset travel time is not the same for these three shot records.	76
4-54	Modeled direct arrivals $G_d(\mathbf{x}_0'', \mathbf{x}_i', t)$ from sources (red asterisks) located along the dipping interface and recorded by receivers (blue triangles) at the surface. The (A) density model and (B) velocity model are extracted from the models in Figure 4-52. (C) $\mathbf{x}_i' = (-2500 \text{ m}, 400 \text{ m})$. (D) $\mathbf{x}_i' = (0 \text{ m}, 600 \text{ m})$. (E) $\mathbf{x}_i' = (2500 \text{ m}, 800 \text{ m})$	77
4-55	Angle-dependent reflectivity in the presence of a dipping interface with constant velocity and varying density. (I) First reflector. (II) Second reflector. (III) Third reflector. (A) Density model. (B) Velocity model. (C) Angle-dependent reflectivity. Bear in mind that the effects of the layers above the redatuming level are removed by the MDD process.	78
4-56	Dipping interface in a medium with a varying velocity and density. (A) Density model. (B) velocity model.	79
4-57	Angle-dependent reflectivity in the presence of a dipping interface with varying velocity and density. (I) First reflector. (II) Second reflector. (III) Third reflector. (A) Density model. (B) Velocity model. (C) Angle-dependent reflectivity.	80
C-1	The result of the deconvolution process before applying stabilization. (A) The redatumed reflection response after mapping into the angle-frequency domain. Note the artifacts at the very low frequency and very high frequency. Also, there are artifacts at the very far angles (at the left edge of the panel). (B) The frequency domain for $\theta = 0$. The dotted red ellipses highlight the artifacts.	92
C-2	The impact of the stabilization parameter e on the deconvolution result. (A) The redatumed reflection response after applying stabilization using $e = 10^{-5}$. Note the artifacts are reduced notably except the very low frequency. (B) The frequency domain for $\theta = 0$ before and after adding e . Note the impact on the high frequencies.	92
C-3	The impact of using a larger value of e on the deconvolution result. (A) The redatumed reflection after applying stabilization using $e = 10^{-4}$. Note the the very high frequency are reduced significantly and the very low frequency are also reduced to some extent. (B) The frequency domain for $\theta = 0$ after increasing e . Note that the other frequencies (7Hz to 80Hz) have slightly decreased.	93
C-4	Defining the limits of the band-pass filter. (A) The redatumed reflection response in the angle-frequency domain with no stabilization. The horizontal black dashed lines represent the limits of the band-pass filter in the frequency domain while the vertical red dashed lines indicate the limits of the band-pass filter in the angle domain. (B) The frequency domain for $\theta = 0$. The vertical black dashed lines represent the limits of the band-pass filter.	93
C-5	The impact of the band-pass filter. (A) The redatumed reflection response after applying the band-pass filter. Note that the artifacts in both low and high frequencies are eliminated except small artifacts in the far angles. (B) The frequency domain for $\theta = 0$ after applying the band-pass filter.	94
C-6	The impact of combining the stabilization parameter e and filtering. (A) The redatumed reflection response after applying e and filtering. Note that the small artifacts in Figure C-5A are removed after adding $e = 10^{-6}$. (B) The frequency domain for $\theta = 0$. Note that the other frequencies are not affected by the stabilization parameter e	94
D-1	Amplitude picking procedure on a flat event, with $c_1 = 1800 \text{ m/s}$, $c_2 = 2300 \text{ m/s}$, $\rho_1 = 1000 \text{ kg/m}^3$, and $\rho_2 = 3000 \text{ kg/m}^3$. (A) Image of the reflector (modulus). (B) The envelope for every depth level (solid thin curves with different colors) and maximum envelope (red dashed curve). The maximum envelope represents the modulus of the angle-dependent reflectivity. (C) Plotting the maximum envelope with the exact reflectivity.	96

- D-2 Amplitude picking procedure on a non-flat event, with $c_1 = 1800$ m/s, $c_2 = 2300$ m/s, $\rho_1 = 1000$ kg/m³, and $\rho_2 = 3000$ kg/m³. (A) Image of the reflector (modulus). (B) The envelope for every depth level (solid thin curves with different colors) and maximum envelope (red dashed curve). The maximum envelope represents the modulus of the angle-dependent reflectivity. (C) Plotting the maximum envelope with the exact reflectivity. 96



Chapter 1

Introduction

One of the objectives of exploration geophysicists is to image the Earth's subsurface and identify its physical properties in order to locate resources and monitor reservoir rocks. This can be achieved by transmitting seismic wavefields into the subsurface and measuring the reflected wavefields with receivers at the surface. The amplitudes of the reflected wavefields are associated with the reflectivities which describe the variations of the physical properties across the boundary (Bacon and Simm, 2014). When reflection images are studied, often only the zero-offset reflectivity is considered (Claerbout, 1978), however, the zero-offset reflectivity can only provide limited information about the subsurface (i.e. zero-incidence acoustic impedance only). In order to obtain more details about the subsurface, the angle-dependent reflectivity has to be taken into account (Castagna and Backus, 1993). This additional information can be used to extract the detailed medium parameters such as velocity and density using the conventional amplitude variation with offset (AVO) analysis techniques (Bortfeld, 1961; Aki, K. and Richards, 1980; Shuey, 1985). These techniques use equations that link the reflectivity to the medium parameters based on a linear approximation of the Zoeppritz expressions (Zoeppritz, 1919). One of these equations is the well-known Shuey approximation (Shuey, 1985) that can be expressed in acoustic media as (see section A-1 for derivation)

$$A(\theta) = A_0 + B \tan^2(\theta), \quad (1-1)$$

where A is the reflection amplitude coefficient at a certain angle of incidence θ (degree), A_0 is the zero-incidence reflection amplitude coefficient, also known as the intercept, and B is the gradient that describes how A varies with θ . The intercept and gradient are known as the AVO attributes from which the velocity and density can be estimated using a subsequent inversion process (Castagna and Backus, 1993; Cambois, 2000). These attributes are given by

$$A_0 = \frac{1}{2} \left(\frac{\Delta c}{c} + \frac{\Delta \rho}{\rho} \right), \quad (1-2)$$

$$B = \frac{1}{2} \left(\frac{\Delta c}{c} \right), \quad (1-3)$$

where Δc is the difference of compressional velocity across the boundary (m/s), $\Delta\rho$ is the difference of density across the boundary (kg/m^3), \bar{c} is the average compressional velocity across the boundary (m/s), and $\bar{\rho}$ is the average density across the boundary (kg/m^3). The Shuey approximation assumes that the velocity and density contrasts across the layer boundary are small and propagation angles are below the critical angle. In practice, the angle-dependent reflectivity is obtained by estimating the AVO response from normal moveout (NMO) corrected prestack data after correcting for source directivity and geometrical spreading (Yu, 1985; Yilmaz, 2001). The information is then used as input in Equation 1-1. However, obtaining the reflectivity correctly from the AVO response can be challenging. When seismic wavefields travel into the subsurface, they can be distorted due to the presence of a strongly complex overburden (Van Der Neut et al., 2014). The effect can be illustrated using the example in Figure 1-1, where two cases are considered. The first case indicates a target located below a homogeneous overburden and another case where the target is located below a high-contrast layer (i.e. an approximation of the strongly complex overburden). The reflection responses for both cases have been modeled using a finite-difference scheme (Thorbecke and Draganov, 2010) with a dipole source and monopole receivers at the surface. The source wavelet used to model the reflection response is a Ricker wavelet with a peak frequency of 25 Hz. The free-surface multiples have not been modeled and the direct wave has been removed from the modeled data. By estimating the AVO of the target for each case, it can be seen that the presence of a strongly complex overburden can produce anomalous AVO responses. This could be explained by the gross transmission losses in the overburden (Hatchell, 2000). As a result, this may lead to a false estimation of the medium parameters when using the anomalous AVO in Equation 1-1. Additionally, the primary reflections may be misinterpreted when they interfere with the internal multiples in the overburden. As such, the internal multiples should be handled before any AVO analysis is applied (Castagna and Backus, 1993; Avseth et al., 2005; Yilmaz, 2001; Chopra, S., Castagna, 2014).

In order to overcome these problems, the overburden effects can be removed by redatuming the surface reflection response to a depth level below the overburden. De Bruin et al. (1990) showed that for an inhomogeneous lossless medium, the angle-dependent reflectivity could be correctly retrieved by means of prestack migration. The approach involves redatuming the surface reflection response to the target using wavefield extrapolation (Wapenaar and Berkhout, 1989) and then estimating the angle-dependent reflectivity by adding all frequency components along lines of constant ray parameter or angle (De Bruin, 1992). Compared to conventional AVO techniques, the approach produced good results up to the critical angle. This suggests that seismic redatuming can potentially recover the reflectivity for each reflector in the subsurface. In standard imaging, the surface reflection response is redatumed using approximations of the downgoing and upgoing wavefields in the subsurface (Wapenaar et al., 2014b). However, this requires a detailed model of the medium between the acquisition surface and target zone, which is not always available in practice.

The Marchenko redatuming method is a novel technology that estimates the downgoing and upgoing Green's functions related to a virtual source located in the subsurface from a surface reflection response with limited information about the medium (Broggini and Snieder, 2012; Wapenaar et al., 2014b,a). These estimated Green's functions represent accurate upgoing and downgoing wavefields as they contain all orders of internal multiple reflections of the subsurface. This gives the Marchenko method an advantage over standard imaging. The Marchenko method also estimates the focusing functions which serve as redatuming operators in the method (Wapenaar et al., 2014a; Slob et al., 2014). The retrieval of the Green's and focusing functions is achieved by solving the coupled Marchenko equations using, for example, an iterative substitution scheme (Wapenaar et al., 2014a; van der Neut et al., 2015). The scheme requires the surface reflection response and direct arrival of the inverse transmission

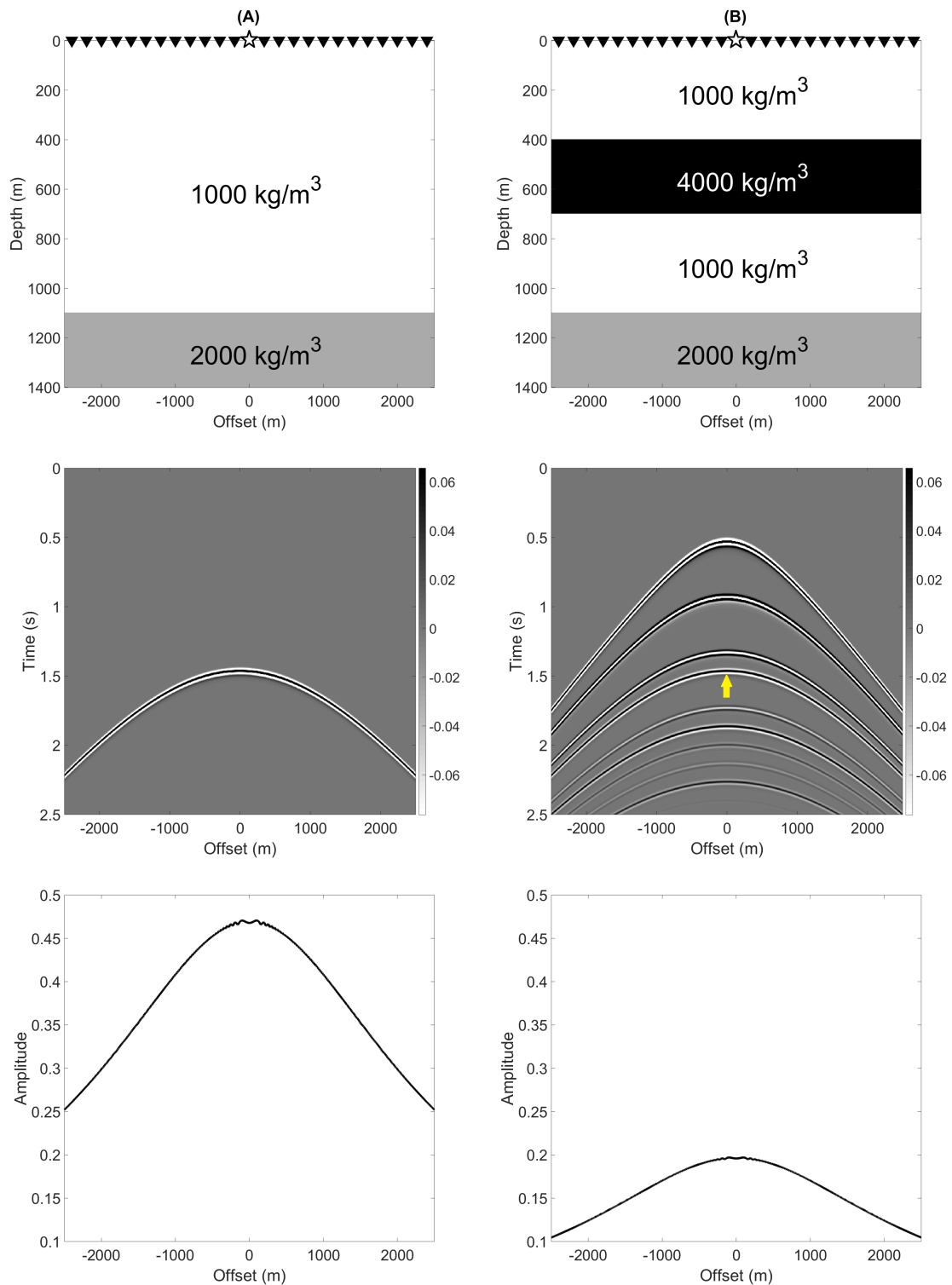


Figure 1-1: Estimated acoustic AVO response in two cases: a homogeneous overburden (Column A) and a high-contrast overburden (Column B). Top row: density model with a background velocity of 1500 m/s. The source (white star) and receivers (black triangles) are located at the surface. The target is located at 1100 m. Middle row: surface reflection response. Note that the yellow arrow in case (B) indicates the primary reflection of the target which corresponds to the one in case (A). Bottom row: AVO response of the target, obtained by estimating the envelope.

response of the overburden as input. In practice, the latter is unknown but can be approximated by the time reversal of the direct arrival from the virtual source, modelled in a smoothed version of the correct velocity model (Wapenaar et al., 2014b). This approximation introduces errors to the AVO response of the Green's functions which are proportional to the transmission losses at the interfaces. Mildner et al. (2019) has shown that this problem can be overcome by determining the AVO transmission losses in a laterally invariant overburden using an augmented Marchenko method (Dukalski et al., 2018). This approach corrects the direct arrival that is estimated from a smooth velocity model. By using this correct direct arrival, the true AVO response of the Green's functions is obtained. However, the effect of the density model on the AVO response is not considered in this approach.

In contrast to Mildner et al. (2019), the error in the direct arrival can be significantly eliminated by deconvolving the retrieved upgoing Green's function with the downgoing Green's function (Wapenaar et al., 2014b) without correcting the direct arrival. The result is a new reflection response, free of spurious events related to internal multiples in the overburden and contains true amplitudes. This can be demonstrated using the 1D numerical example in Figure 1-2 where a target is located below a high-contrast overburden. Here, the Marchenko method and standard method are used to redatum the reflection response using deconvolution. The standard redatuming is applied using only the direct arrival as the focusing function. Compared to direct modelling, the Marchenko method was able to reconstruct the reflection response perfectly in the zone of interest, unlike standard redatuming which did not resolve the overburden effects. The redatumed reflection response obtained by the Marchenko method can be used for reflection imaging in the zone of interest. Because the reflection response has been correctly reconstructed at the redatumed level, the image will represent the zone of interest correctly. See Figure 1-3. This 1D example has shown that the Marchenko method is capable of removing the overburden effects (i.e. internal multiples and transmission losses) and compensates for the error in the direct arrival using deconvolution. In practice, however, the angle-dependent reflectivity requires at least 2D data.

Following a similar approach as De Bruin et al. (1990), the Marchenko method will be evaluated for imaging angle-dependent reflectivity in 2D laterally invariant acoustic media using deconvolution. In chapter 2, the theory of the Marchenko method will be explained in 2D according to Wapenaar et al. (2014b) and van der Neut et al. (2015). First, the classic Green's function representation will be reviewed according to Wapenaar and Berkhout (1989) and how this representation can be replaced by a single-sided Green's representation in an inhomogeneous lossless medium. Next, the focusing functions will be explained and how they can be constructed in a truncated version of the actual medium. Then, it will be shown how the coupled Marchenko equations work and how these equations can be solved for the focusing and Green's functions using an iterative substitution scheme. After that, the Marchenko redatuming will be covered. In chapter 3, the properties of the angle-dependent reflectivity in angle domain, wavenumber domain, and ray parameter domain will be explained and how these three different domains can be related to each other. Then, the estimation of angle-dependent reflectivity using the Marchenko method will be explained and how the reflectivity can be presented in terms of $z - p$ gathers (i.e. ray-parameter reflection information as a function of depth), and in terms of $z - \theta$ gathers (i.e. angle reflection information as a function of depth). In chapter 4, the imaging process will be demonstrated with numerical examples. Each numerical example introduces a particular problem for which the Marchenko method is tested and compared to standard imaging. Finally, chapter 5 gives the conclusions and some final remarks.

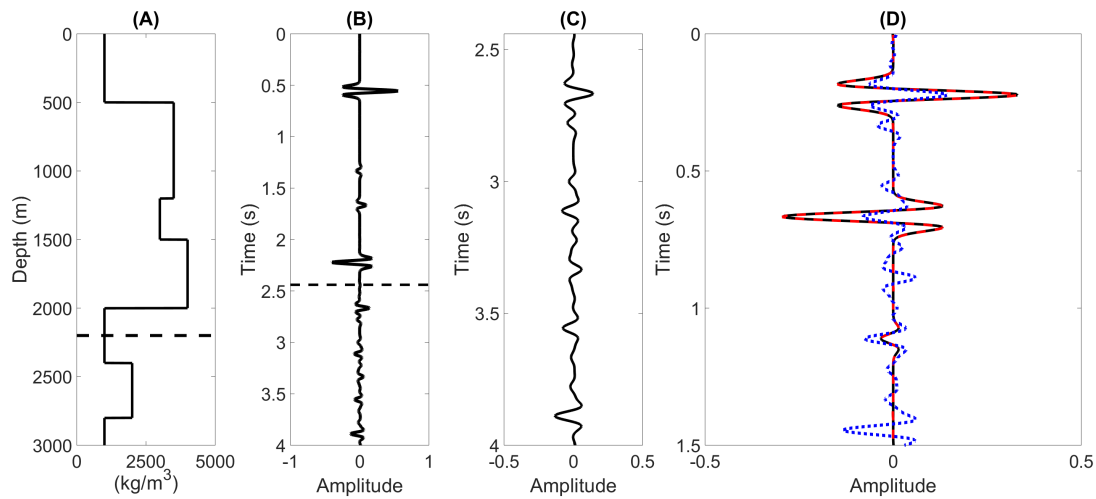


Figure 1-2: Marchenko redatuming in 1D with a constant velocity of 1800 m/s. The dashed line represents the redatuming level. (A) Density model. (B) Reflection response with a source and receiver located at the surface. A Ricker wavelet has been used as a source wavelet with a peak frequency of 10 Hz. (C) Zoomed version of the zone of interest in (B). (D) Marchenko-based redatumed response (dashed red), standard-based redatumed response (dotted blue), and direct modeling (dashed black). Both redatumed responses were obtained by deconvolution.

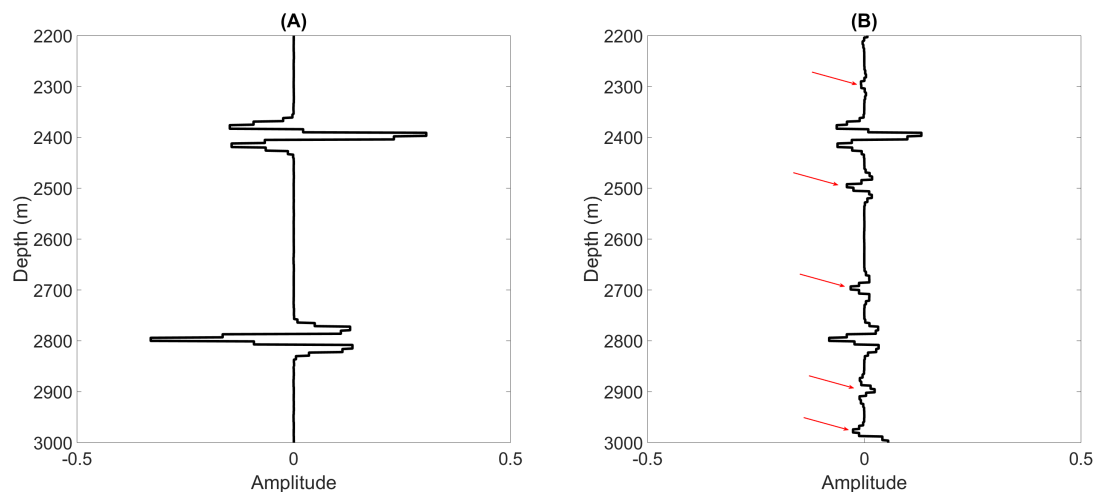


Figure 1-3: Image of the zone of interest in Figure 1-2. The image was produced by extracting the zero-time component from the redatumed response at every depth level, with a step size of 1 m. (A) Marchenko imaging. (B) Standard imaging. The red arrows indicate the effects of the overburden. Note that these effects have been removed by the Marchenko method. Also, the amplitude is preserved at the depth of each reflector.

Chapter 2

Marchenko method

2-1 Notations and Fourier transforms

In a 2D medium, the space vector is denoted by $\mathbf{x} = (x, z)$ with x as the horizontal coordinate and z as the vertical coordinate pointing downward. The temporal Fourier transform of a space- and time-dependent real-valued function $u(\mathbf{x}, t)$ is defined as

$$\hat{u}(\mathbf{x}, \omega) = \int_{-\infty}^{\infty} \exp(-j\omega t) u(\mathbf{x}, t) dt, \quad (2-1)$$

where t is time, j is the imaginary unit, and ω is the angular frequency. The inverse of $\hat{u}(\mathbf{x}, \omega)$ is defined as

$$u(\mathbf{x}, t) = \frac{1}{2\pi} \int_{-\infty}^{\infty} \exp(j\omega t) \hat{u}(\mathbf{x}, \omega) d\omega. \quad (2-2)$$

The two-dimensional Fourier transform of $u(\mathbf{x}, t)$ is defined as

$$\tilde{u}(k_x, z, \omega) = \int_{-\infty}^{\infty} \int_{-\infty}^{\infty} u(\mathbf{x}, t) \exp(-j(\omega t - k_x x)) dt dx, \quad (2-3)$$

where k_x is the horizontal wavenumber. The inverse of $\tilde{u}(k_x, z, \omega)$ is defined as

$$u(\mathbf{x}, t) = \frac{1}{4\pi^2} \int_{-\infty}^{\infty} \int_{-\infty}^{\infty} \tilde{u}(k_x, z, \omega) \exp(j(\omega t - k_x x)) d\omega dk_x. \quad (2-4)$$

2-2 Green's function

The Green's function G is defined as the solution of the 2D acoustic wave equation in an inhomogeneous lossless medium, according to (Wapenaar et al., 2014b)

$$\rho(\mathbf{x}) \nabla \cdot \left(\frac{1}{\rho(\mathbf{x})} \nabla G(\mathbf{x}, \mathbf{x}_0'', t) \right) - \frac{1}{c^2(\mathbf{x})} \frac{\partial^2 G(\mathbf{x}, \mathbf{x}_0'', t)}{\partial t^2} = -\rho(\mathbf{x}) \delta(\mathbf{x} - \mathbf{x}_0'') \frac{\partial \delta(t)}{\partial t}, \quad (2-5)$$

where \mathbf{x}_0'' represents the location of a source point, ρ is the mass density (kg/m^3), c is the velocity (m/s), and δ is a Dirac delta function. Equation 2-5 states that the Green's function $G(\mathbf{x}, \mathbf{x}_0'', t)$ is the impulse response at observation points \mathbf{x} as a function of time t , related to a source point located at \mathbf{x}_0'' . This is known as the causal Green's function, which propagates away from the source and is zero for $t < 0$. See Figure 2-1A. By the principle of time-reversal (Wapenaar and Berkhout, 1989; Fink et al., 2000), the time-reversed Green's function is given by $G(\mathbf{x}, \mathbf{x}_0'', -t)$. This is known as the anti-causal Green's function, which propagates towards the source and is zero for $t > 0$. See Figure 2-1B. If the Green's function is known, the acoustic wavefield can be calculated anywhere in the interior, according to (Wapenaar and Berkhout, 1989)

$$\hat{P}(\mathbf{x}_0'', \omega) = \oint_S \frac{1}{\rho(\mathbf{x})} [\hat{G}(\mathbf{x}, \mathbf{x}_0'', \omega) \nabla \hat{P}(\mathbf{x}, \omega) - \hat{P}(\mathbf{x}, \omega) \nabla \hat{G}(\mathbf{x}, \mathbf{x}_0'', \omega)] \cdot \mathbf{n} dS, \quad (2-6a)$$

$$\hat{P}(\mathbf{x}_0'', \omega) = \oint_S \frac{1}{\rho(\mathbf{x})} [\hat{G}^*(\mathbf{x}, \mathbf{x}_0'', \omega) \nabla \hat{P}(\mathbf{x}, \omega) - \hat{P}(\mathbf{x}, \omega) \nabla \hat{G}^*(\mathbf{x}, \mathbf{x}_0'', \omega)] \cdot \mathbf{n} dS, \quad (2-6b)$$

where $\hat{P}(\mathbf{x}_0'', \omega)$ represents the total acoustic wavefield (i.e. the Green's function convolved with a source wavelet) at point \mathbf{x}_0'' inside boundary S with \mathbf{n} as the normal to the boundary, and $\hat{P}(\mathbf{x}, \omega)$ represents the wavefield observed at the boundary. The asterisk superscript indicates complex conjugate which replaces the time-reversal in the frequency domain. Hence, the products in Equation 2-6b correspond to cross-correlations in the time domain, while the products in Equation 2-6a correspond to convolution in the time domain. These two expressions are known as the Kirchhoff–Helmholtz integral, based on the Green's theorem (Morse and Feshbach, 1953; Berkhout and Wapenaar, 1989). They state that if the wavefield and its normal derivative are known at the boundary, the total acoustic wavefield can be reconstructed anywhere inside the boundary using the Green's function. Consequently, if the Green's function to the reconstruction points is known, there is no need to know a model between the acquisition surface (i.e. boundary S) and reconstruction points in the interior. In reality, however, the wavefield cannot be perfectly reconstructed as this requires having receivers enclosing the medium of interest. For the correlation-type representation (Equation 2-6b), the closed boundary can be replaced by an open boundary, but this depends on a number of assumptions that are not always fulfilled in practice, for example one-sided illumination (Wapenaar et al., 2010). For the convolution-type representation, the closed boundary can be easily replaced by an open boundary (Wapenaar et al., 2010).

With reference to Figure 2-2, a single-sided acquisition surface is considered (Wapenaar et al., 2014b), where the source and receivers are located at one side of the medium, usually the surface of the Earth. In this configuration, the surface boundary is denoted by $\partial\mathbb{D}_0$, below which an inhomogeneous lossless half-space. The half-space above the surface boundary is assumed to be homogeneous. The boundary $\partial\mathbb{D}_0$ is assumed to be a transparent surface which means there will be no free-surface related multiples. The coordinates along $\partial\mathbb{D}_0$ are defined as $\mathbf{x}_0 = (x, z_0)$, with $z_0 = 0$. The source point is located just above the surface at $\mathbf{x}_0'' = (x'', z \rightarrow 0)$. In addition, an arbitrary depth level $\partial\mathbb{D}_i$ is defined. The coordinates along $\partial\mathbb{D}_i$ are denoted by $\mathbf{x}_i = (x, z_i)$, with z_i as the depth of $\partial\mathbb{D}_i$.

With reference to Figure 2-3, the field generated from the point source propagates upward to the homogeneous half-space and downward into the inhomogeneous medium. Because the medium above $\partial\mathbb{D}_0$ is homogeneous, there will be no contribution from it. Assuming the one-way Green's functions are pressured normalized, the Green's function associated with the downgoing part of the radiating source is given by (Wapenaar et al., 2014b)

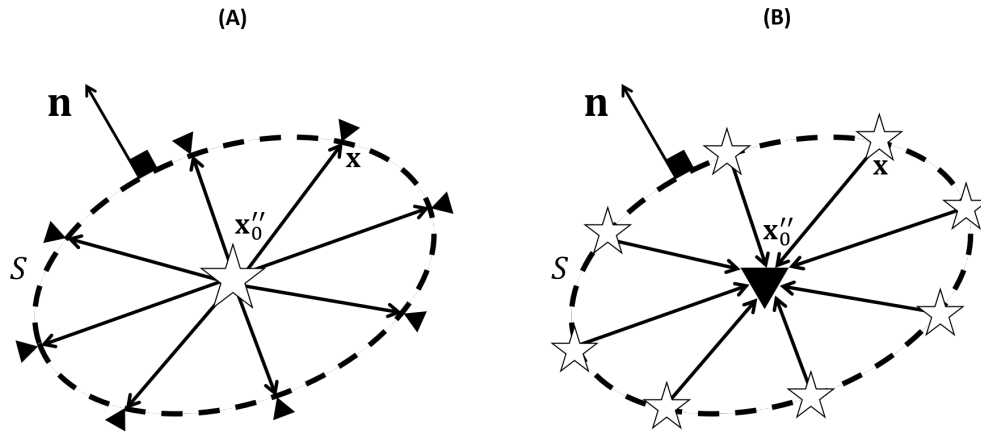


Figure 2-1: Classic Green's function. (A) The causal Green's function. The star represents a source point located at \mathbf{x}''_0 whereas the triangle represents an observation point (receiver) located at \mathbf{x} . The medium is enclosed by boundary S . The arrows represent the direction of the wavefields. (B) The anti-causal Green's function obtained by the principle of time reversal. Here, location \mathbf{x} is interpreted as a source point while location \mathbf{x}''_0 is interpreted as an observation point.

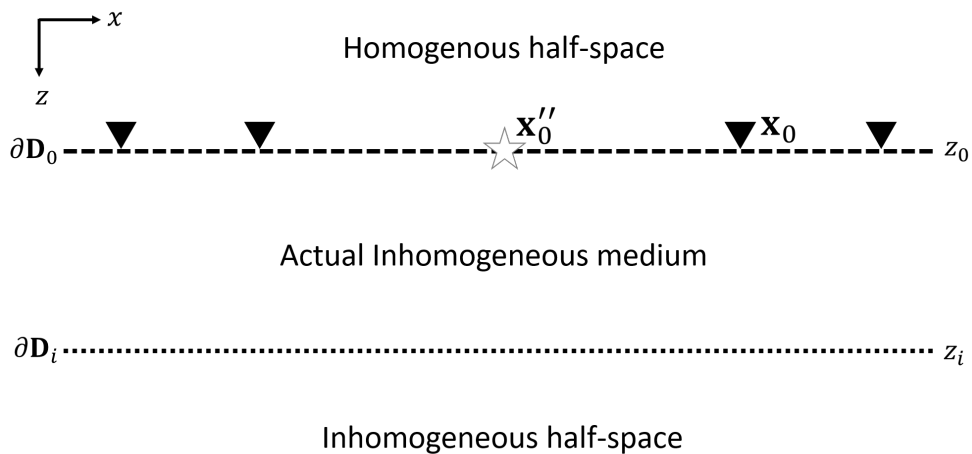


Figure 2-2: Single-sided acquisition surface, with a source point (white star) located at \mathbf{x}''_0 and receivers (black triangles) at \mathbf{x}_0 . The black dashed line on the top represents the transparent surface whereas the dotted line represents the arbitrary depth level.

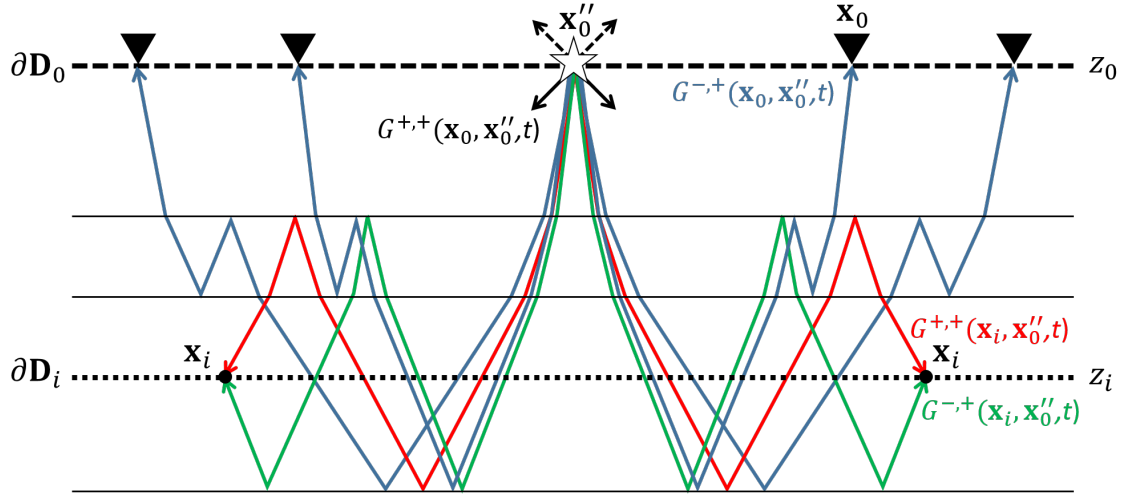


Figure 2-3: Single-sided Green's function in an inhomogeneous medium due to a source point (star) located at \mathbf{x}_0'' . The Green's function is described by four components as shown here. The solid black lines represent interfaces. Note that the dashed arrows above the source represent the field propagating to the homogeneous half-space.

$$\partial_z G^{+,+}(\mathbf{x}, \mathbf{x}_0'', t)|_{z=z_0} = -\frac{1}{2}\rho(\mathbf{x}_0'')\delta(x-x'')\frac{\partial\delta(t)}{\partial t}, \quad (2-7)$$

with the Dirac delta function located at z_0 . The first superscript (+) refers to the downgoing field observed at \mathbf{x} , whereas the second superscript (+) refers to the downgoing field of the source at \mathbf{x}_0'' . The Green's function associated with the upgoing field at $\partial\mathbb{D}_0$ is defined as (Wapenaar et al., 2014b)

$$\partial_z G^{-,+}(\mathbf{x}, \mathbf{x}_0'', t)|_{z=z_0} = \frac{1}{2}\rho(\mathbf{x}_0)\frac{\partial R(\mathbf{x}_0'', \mathbf{x}_0, t)}{\partial t}, \quad (2-8)$$

where $R(\mathbf{x}_0'', \mathbf{x}_0, t)$ is the reflection response of the inhomogeneous medium with a dipole source at \mathbf{x}_0 and observed by a monopole receiver at \mathbf{x}_0'' . Here the first superscript (-) refers the upgoing field observed at \mathbf{x}_0 whereas the second superscript (+) refers to the downgoing field of the source at \mathbf{x}_0'' . The total Green's function $G(\mathbf{x}, \mathbf{x}_0'', t)$ can be expressed as the superposition of the pressure-normalized downgoing and upgoing components (Wapenaar et al., 2014b)

$$G(\mathbf{x}, \mathbf{x}_0'', t) = G^{+,+}(\mathbf{x}, \mathbf{x}_0'', t) + G^{-,+}(\mathbf{x}, \mathbf{x}_0'', t). \quad (2-9)$$

The fields $G^{+,+}(\mathbf{x}_i, \mathbf{x}_0'', t)$ and $G^{-,+}(\mathbf{x}_i, \mathbf{x}_0'', t)$ represent the downgoing and upgoing components of the Green's function, respectively, observed at $\partial\mathbb{D}_i$ with a source located at \mathbf{x}_0'' . These two fields are the desired Green's functions in the Marchenko method. They act as redatuming operators for the surface reflection response $R(\mathbf{x}_0'', \mathbf{x}_0, t)$. In the next section, it will be explained how the focusing functions work and how these focusing functions served as redatuming operators for the desired Green's functions.

2-3 Focusing function

The focusing functions f serve as the essential redatuming operators in the Marchenko method. They were introduced based on the reciprocity theorem for one-way wavefields (Wapenaar et al., 2014a; Slob et al., 2014). The focusing functions are designed to focus the wavefields at a certain point in the subsurface and to subsequently be used to retrieve the desired Green's functions. The point at which the wavefields are focused is called the focal point. The depth level at which the focal point is located is called the focal level. Analogous to equation Equation 2-9, the focusing function f_1 can be expressed as the superposition of the pressure-normalized downgoing and upgoing parts (Wapenaar et al., 2014b)

$$f_1(\mathbf{x}, \mathbf{x}'_i, t) = f_1^+(\mathbf{x}, \mathbf{x}'_i, t) + f_1^-(\mathbf{x}, \mathbf{x}'_i, t), \quad (2-10)$$

where $\mathbf{x}'_i = (x', z_i)$ represent the location of the focal point at $\partial\mathbb{D}_i$. In contrast, the focusing function $f_2(\mathbf{x}, \mathbf{x}''_0, t)$ that focuses the wavefields at a focal point located at $\partial\mathbb{D}_0$ can be expressed by its upgoing and downgoing components as follows (Wapenaar et al., 2014b)

$$f_2(\mathbf{x}, \mathbf{x}''_0, t) = f_2^+(\mathbf{x}, \mathbf{x}''_0, t) + f_2^-(\mathbf{x}, \mathbf{x}''_0, t). \quad (2-11)$$

The subscripts 1 and 2 are used to distinguish between the two types of focusing functions. Wapenaar et al. (2014b) showed that f_1 and f_2 are related, according to

$$f_1^+(\mathbf{x}''_0, \mathbf{x}'_i, t) = f_2^-(\mathbf{x}'_i, \mathbf{x}''_0, t), \quad (2-12)$$

$$-f_1^-(\mathbf{x}''_0, \mathbf{x}'_i, -t) = f_2^+(\mathbf{x}'_i, \mathbf{x}''_0, t). \quad (2-13)$$

Using Equation 2-12 and Equation 2-13, Equation 2-11 can alternatively be expressed as follows

$$f_2(\mathbf{x}'_i, \mathbf{x}''_0, t) = f_1^+(\mathbf{x}''_0, \mathbf{x}'_i, t) - f_1^-(\mathbf{x}''_0, \mathbf{x}'_i, -t). \quad (2-14)$$

To understand the principle of the focusing functions, two states are introduced based on the reciprocity theorem for one-way wavefields (Slob et al., 2014; Wapenaar et al., 2014b; van der Neut et al., 2015). The first state is denoted by A and refers to a truncated version of the actual medium, see Figure 2-4A. Here, the medium is bounded between $\partial\mathbb{D}_0$ and $\partial\mathbb{D}_i$, with $R_A(\mathbf{x}''_0, \mathbf{x}_0, t')$ as reflection response at the surface in the truncated medium, and $T(\mathbf{x}_i, \mathbf{x}''_0, t)$ as the transmission response of the truncated medium. The medium below $\partial\mathbb{D}_i$ is assumed to be reflection free (i.e. no contribution from below the focal level). The second state is denoted by B and refers to the actual medium, see Figure 2-4B. Here, the medium covers everything below $\partial\mathbb{D}_0$, with $R(\mathbf{x}''_0, \mathbf{x}_0, t')$ as the reflection response of the actual medium at the surface. At the focal level, the wavefields are described by the Green's functions $G^{+,+}(\mathbf{x}_i, \mathbf{x}''_0, t)$ and $G^{-,+}(\mathbf{x}_i, \mathbf{x}''_0, t)$. Note that the reflection and transmission responses include all primary reflections and possible internal multiples in both states. The downgoing focusing function f_1^+ is defined as the inverse of the transmission response T , satisfying (van der Neut et al., 2015)

$$\delta(x - x') \delta(t) = \int_{\partial\mathbb{D}_0} \int_{-\infty}^t f_1^+(\mathbf{x}''_0, \mathbf{x}'_i, t - t') T(\mathbf{x}_i, \mathbf{x}''_0, t') dt' d\mathbf{x}''_0, \quad (2-15)$$

whereas the upgoing part f_1^- is defined as the response of the truncated medium to f_1^+ , satisfying (van der Neut et al., 2015)

$$f_1^-(\mathbf{x}_0, \mathbf{x}'_i, t) = \int_{\partial\mathbb{D}_0} \int_{-\infty}^{\infty} f_1^+(\mathbf{x}''_0, \mathbf{x}'_i, t - t') R_A(\mathbf{x}_0, \mathbf{x}''_0, t') dt' d\mathbf{x}''_0. \quad (2-16)$$

Note that the delta function in Equation 2-15 is located at z_i and should be considered as a spatially band-limited delta function, where the evanescent field has been ignored (Wapenaar et al., 2014b). From Equation 2-15 and Equation 2-16, it can be seen that obtaining of f_1^- requires the computation of f_1^+ first. In practice, the function f_1^+ is unknown. However, it can be approximated by employing an initial estimation of the function. The initial estimation of the downgoing focusing function f_{1d}^+ represents the direct arrival of the inverse of the transmission response in the truncated medium, according to (Wapenaar et al., 2014b)

$$f_{1d}^+(\mathbf{x}''_0, \mathbf{x}'_i, t) = T_d^{inv}(\mathbf{x}'_i, \mathbf{x}''_0, t), \quad (2-17)$$

where T_d^{inv} is the direct arrival of the inverse of the transmission response with travel time $t_d = t_d(\mathbf{x}'_i, \mathbf{x}''_0)$. The abbreviation *inv* stands for the inverse of T_d . With reference to Figure 2-5A, the initial focusing function f_{1d}^+ is sent from $\partial\mathbb{D}_0$ at time $t = -t_d$ and arrives at the focal point at $t = 0$. As the field f_{1d}^+ propagates, the upgoing focusing function f_1^- is generated and arrives at $\partial\mathbb{D}_0$, see Figure 2-5B. However, as f_1^- propagates, it generates spurious events that are not desirable, see Figure 2-5C. These events can be eliminated by sending downgoing cancelling operators known as the scattering coda M^+ , which has specific travel times and amplitudes to prevent the generation of the spurious events, see Figure 2-5D. In general, the function f_1^+ can be expressed as follows

$$f_1^+(\mathbf{x}''_0, \mathbf{x}'_i, t) = T_d^{inv}(\mathbf{x}'_i, \mathbf{x}''_0, t) + M^+(\mathbf{x}''_0, \mathbf{x}'_i, t). \quad (2-18)$$

Wapenaar et al. (2014b) showed that the transmission response T_d^{inv} is related in a specific way to the Green's function between $\partial\mathbb{D}_0$ and $\partial\mathbb{D}_i$ and can be sufficiently approximated as

$$T_d^{inv}(\mathbf{x}'_i, \mathbf{x}''_0, t) \approx G_d(\mathbf{x}''_0, \mathbf{x}'_i, -t), \quad (2-19)$$

where $G_d(\mathbf{x}''_0, \mathbf{x}'_i, -t)$ is the time reversal of the direct arrival of Green's function. Hence, expression Equation 2-18 can be simply expressed as follows

$$f_1^+(\mathbf{x}, \mathbf{x}'_i, t) \approx G_d(\mathbf{x}, \mathbf{x}'_i, -t) + M^+(\mathbf{x}, \mathbf{x}'_i, t). \quad (2-20)$$

Equation 2-20 states that the downgoing focusing function is approximated by the time reversal of the direct arrival of Green's function and scattering coda. This will introduce errors in the result that are proportional to the transmission losses at the interfaces (Wapenaar and Berkhout, 1989). When estimating the redatumed reflection response, these errors can be avoided as will be explained in section 2-5. At the focal point \mathbf{x}'_i , the field $f_1^+(\mathbf{x}''_0, \mathbf{x}'_i, t)$ acts as a virtual source of an impulse response operating at $t = 0$. Beyond the focal point \mathbf{x}'_i , the field diverges and after reflection it arrives at the surface, as shown in Figure 2-6. This is the first response of the focusing function which is the Green's function $G^{-,+}(\mathbf{x}''_0, \mathbf{x}'_i, t)$. In contrast, the time-reversed upgoing focusing function $f_1^-(\mathbf{x}''_0, \mathbf{x}'_i, -t)$ acts as a virtual source generating the Green's function $G^{-,-}(\mathbf{x}''_0, \mathbf{x}'_i, t)$ along with the time-reversed

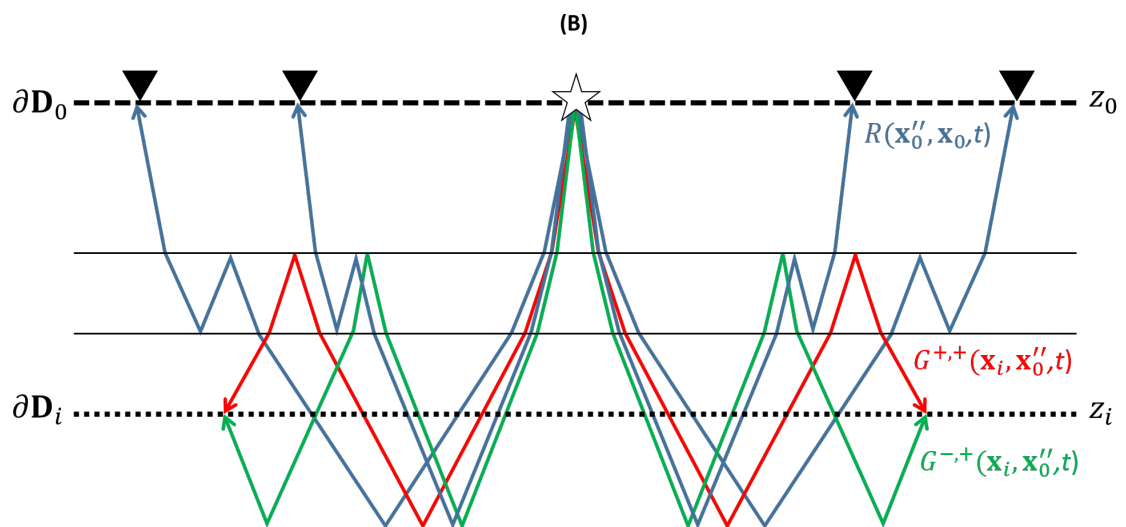
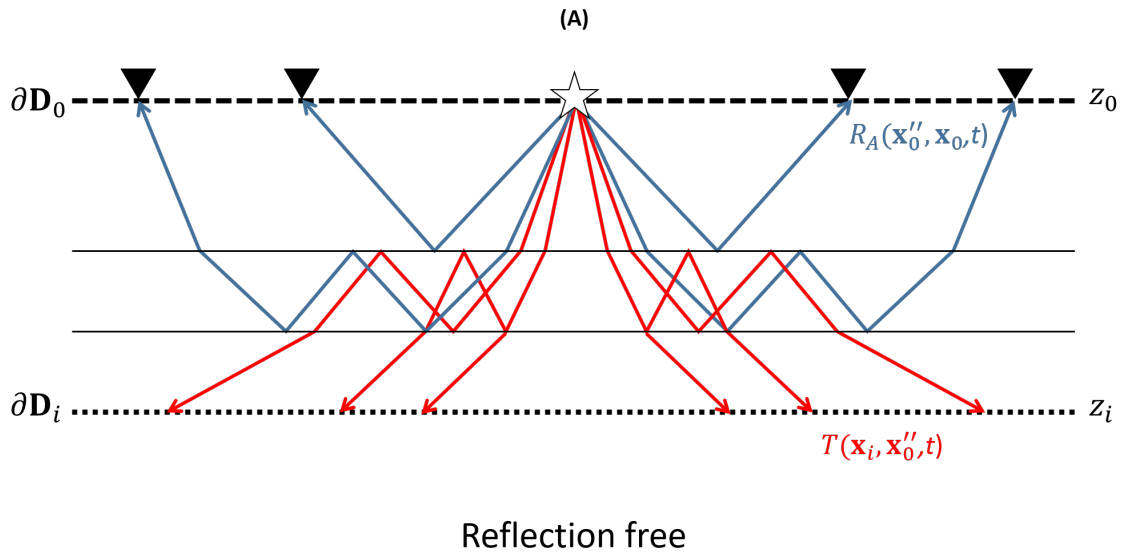


Figure 2-4: Illustration of the two states that are explained in the main text. (A) State A. (B) state B.

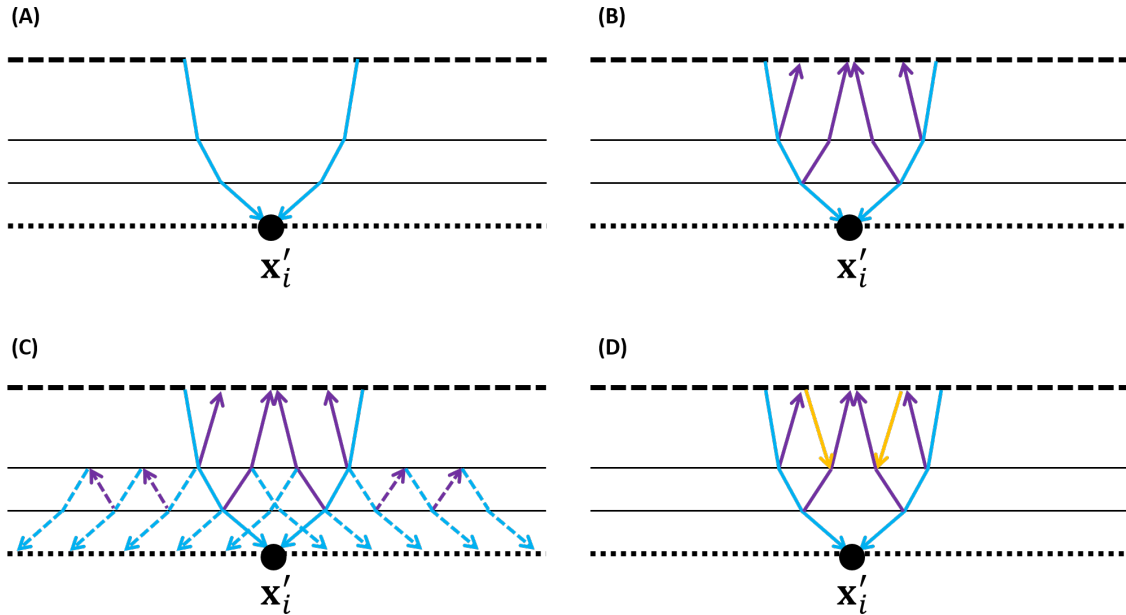


Figure 2-5: Illustration of the focusing function in the truncated medium. The black dashed and dotted lines represent $\partial\mathbb{D}_0$ and $\partial\mathbb{D}_i$, respectively. The black solid lines represent interfaces. (A) Initiating f_1^+ by sending f_{1d}^+ (cyan) from the surface to the focal point (solid circle) at \mathbf{x}'_i . (B) Generation of f_1^- (purple) as the response of the truncated medium to f_{1d}^+ . (C) Generation of spurious events (dashed purple and cyan) due to the propagation of f_1^- . (D) Scattering coda M^+ (yellow) is sent to cancel these spurious events. The focusing function f_1^+ is composed of the cyan and yellow events.

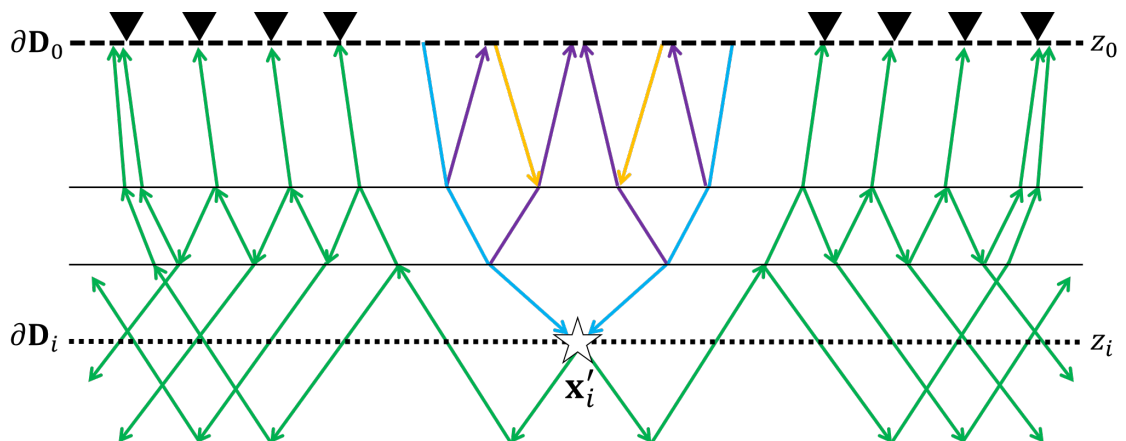


Figure 2-6: The Green's function $G^{-,+}$ (green) as the response of f_1^+ (cyan+yellow). The purple arrows represent f_1^- .

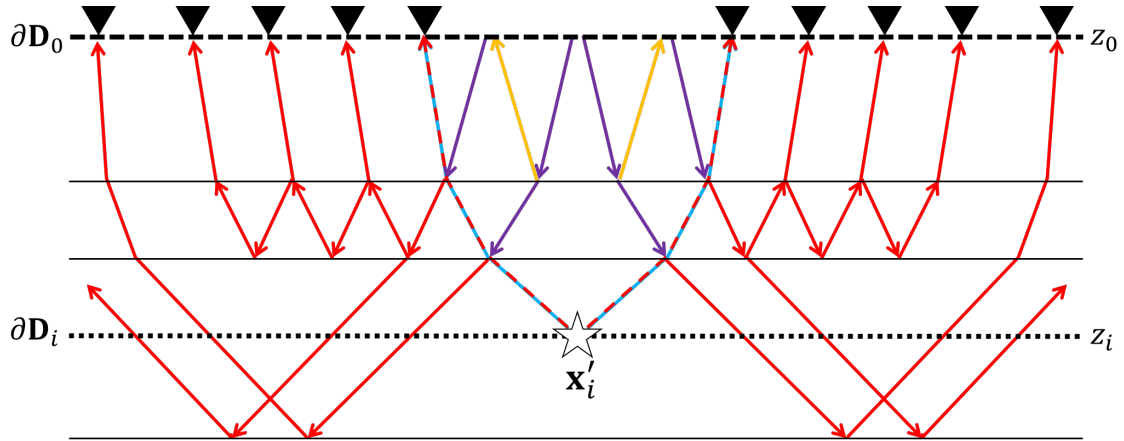


Figure 2-7: The Green's function $G^{-,+}$ (red) and the time-reversed f_1^+ (cyan+yellow) as the response of the time-reversed f_1^- (purple). Note that the dashed (cyan+red) arrows represent the overlap between $G^{-,+}$ and the time-reversed f_1^+ .

downgoing focusing function $f_1^+(\mathbf{x}_0'', \mathbf{x}'_i, -t)$, see Figure 2-7. This is the second response of the focusing function. In the next section, the estimation of the Green's and focusing functions using the coupled Marchenko equations will be explained.

2-4 The coupled Marchenko equations

The coupled Marchenko equations form the basis for obtaining the focusing functions and Green's functions. The equations relate three functions to each other: the Green's function in the actual medium, the reflection response in the actual medium, and the focusing function in the truncated medium. Mathematically, the equations can be expressed as (Wapenaar et al., 2014b)

$$G^{-,+}(\mathbf{x}_0'', \mathbf{x}'_i, t) + f_1^-(\mathbf{x}_0'', \mathbf{x}'_i, t) = \int_{\partial\mathbb{D}_0} \int_{-\infty}^t R(\mathbf{x}_0'', \mathbf{x}_0, t-t') f_1^+(\mathbf{x}_0, \mathbf{x}'_i, t') dt' d\mathbf{x}_0, \quad (2-21)$$

$$G^{-,-}(\mathbf{x}_0'', \mathbf{x}'_i, t) + f_1^+(\mathbf{x}_0'', \mathbf{x}'_i, -t) = \int_{\partial\mathbb{D}_0} \int_{-\infty}^t R(\mathbf{x}_0'', \mathbf{x}_0, t-t') f_1^-(\mathbf{x}_0, \mathbf{x}'_i, -t') dt' d\mathbf{x}_0. \quad (2-22)$$

The ultimate goal of the equations is to retrieve $G^{-,+}$ and $G^{-,-}$. Since the focusing functions are initially unknown, the system is an under-determined problem. However, the system can be solved using an iterative scheme of the coupled Marchenko equations (Wapenaar et al., 2014b; van der Neut et al., 2015). The scheme is based on the causality relations between the Green's functions and focusing functions. The focusing wavefield arrives before the Green's wavefield; therefore, they can be separated in time from each other by applying a mute window $\Theta = \Theta(\mathbf{x}'_i, \mathbf{x}_0'')$. This window is designed to remove all causal events that arrive at and after t_d . In addition, the window removes all anti-causal events that arrive at and before $-t_d$. However, because in practice seismic data are band-limited, a small positive constant ϵ has to be applied to the window to account for the width of the wavelet. Assuming that the wavelet is zero-phase, the value of ϵ has to be half the wavelet duration to avoid removing part of the events. For causal events, the window should remove all events that

arrive at and after $t_d - \epsilon$. For anti-causal events, the window should remove all events that arrive at and before $-t_d + \epsilon$, see [Figure 2-8](#). By applying Θ on the Green's functions and focusing functions, causality dictates

$$\Theta \{G^{-,+}(\mathbf{x}_0'', \mathbf{x}'_i, t)\} = 0, \quad (2-23)$$

$$\Theta \{G^{-,-}(\mathbf{x}_0'', \mathbf{x}'_i, t)\} = 0, \quad (2-24)$$

$$\Theta \{f_1^+(\mathbf{x}_0'', \mathbf{x}'_i, t)\} = \Theta \{G_d(\mathbf{x}_0'', \mathbf{x}'_i, -t) + M^+(\mathbf{x}_0'', \mathbf{x}'_i, t)\} = M^+(\mathbf{x}_0'', \mathbf{x}'_i, t), \quad (2-25)$$

$$\Theta \{f_1^-(\mathbf{x}_0'', \mathbf{x}'_i, t)\} = f_1^-(\mathbf{x}_0'', \mathbf{x}'_i, t). \quad (2-26)$$

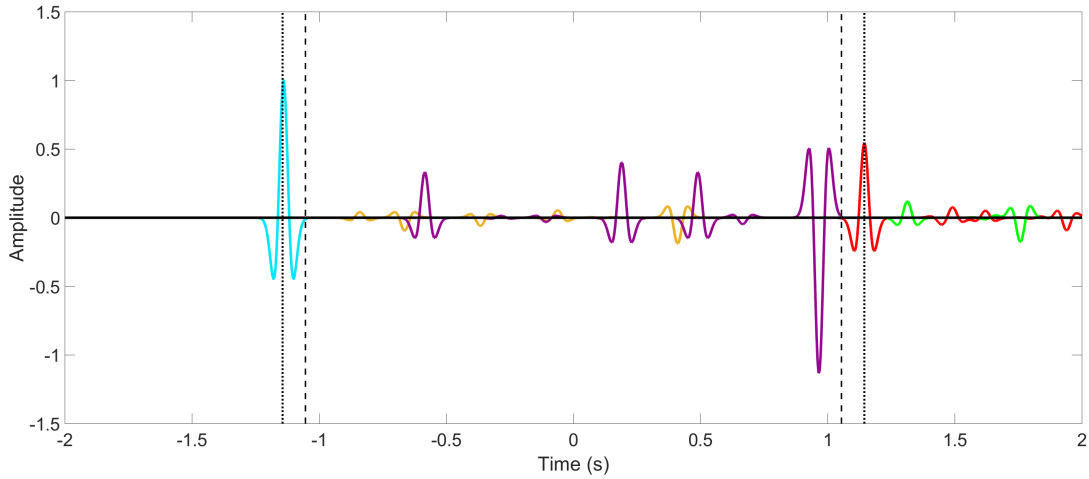


Figure 2-8: The definition of the mute window Θ . The vertical dotted lines represent the arrival time t_d while the vertical dashed lines represent the limits of the mute window Θ after applying the positive constant ϵ . Note that the difference between the dashed and dotted lines is half the duration of the wavelet. The wavelet used here is a Ricker wavelet with a peak frequency of 10 Hz. In this case, the operator Θ will mute f_{1d}^+ (cyan), $G^{-,-}$ (red), $G^{-,+}$ (green) and pass f_1^- (purple) and M^+ (yellow).

The coupled Marchenko equations ([Equation 2-21](#) and [Equation 2-22](#)) after applying Θ becomes

$$f_1^-(\mathbf{x}_0'', \mathbf{x}'_i, t) = \Theta \left\{ \int_{\partial\mathbb{D}_0} \int_{-\infty}^t R(\mathbf{x}_0'', \mathbf{x}_0, t-t') f_1^+(\mathbf{x}_0, \mathbf{x}'_i, t') dt' d\mathbf{x}_0 \right\}, \quad (2-27)$$

$$M^+(\mathbf{x}_0'', \mathbf{x}'_i, -t) = \Theta \left\{ \int_{\partial\mathbb{D}_0} \int_{-\infty}^t R(\mathbf{x}_0'', \mathbf{x}_0, t-t') f_1^-(\mathbf{x}_0, \mathbf{x}'_i, -t') dt' d\mathbf{x}_0 \right\}. \quad (2-28)$$

The latter two expressions can be posed as an iterative substitution to estimate the focusing functions as follows

$$f_{1,k}^-(\mathbf{x}_0'', \mathbf{x}'_i, t) = \Theta \left\{ \int_{\partial\mathbb{D}_0} \int_{-\infty}^t R(\mathbf{x}_0'', \mathbf{x}_0, t-t') f_{1,k}^+(\mathbf{x}_0, \mathbf{x}'_i, t') dt' d\mathbf{x}_0 \right\}, \quad (2-29)$$

$$M_k^+(\mathbf{x}_0'', \mathbf{x}'_i, -t) = \Theta \left\{ \int_{\partial\mathbb{D}_0} \int_{-\infty}^t R(\mathbf{x}_0'', \mathbf{x}_0, t-t') f_{1,k-1}^-(\mathbf{x}_0, \mathbf{x}'_i, -t') dt' d\mathbf{x}_0 \right\}, \quad (2-30)$$

with k as the iteration number, and

$$f_{1,k}^+(\mathbf{x}, \mathbf{x}'_i, t) = G_d(\mathbf{x}, \mathbf{x}'_i, -t) + M_k^+(\mathbf{x}, \mathbf{x}'_i, t). \quad (2-31)$$

The scheme is initiated with the assumption that the value of $M_0^+ = 0$ and $f_{1,0}^+ = G_d$. The estimate of $f_{1,0}^-$ can be obtained by Equation 2-29. This estimate is then substituted into Equation 2-30 to obtain the value of M_1^+ . In the second iteration, the value of M_1^+ is added to G_d to estimate $f_{1,1}^+$. This estimate is then substituted into Equation 2-29 to obtain $f_{1,1}^-$. This process is repeated until the scheme converges. Once the focusing functions are estimated, the Green's functions $G^{-,+}$ and $G^{-,-}$ can be calculated using Equation 2-21 and Equation 2-22. In the integral of the coupled Marchenko equations, there are stationary points at the depth of interest that should be sampled in the acquisition survey at the surface in order to retrieve particular events of the Green's functions. However, reflection data, in practice, are recorded with a finite aperture. This may introduce some practical issues when using the Marchenko method as particular events of the Green's functions would require a certain range of aperture, as illustrated in Figure 2-9.

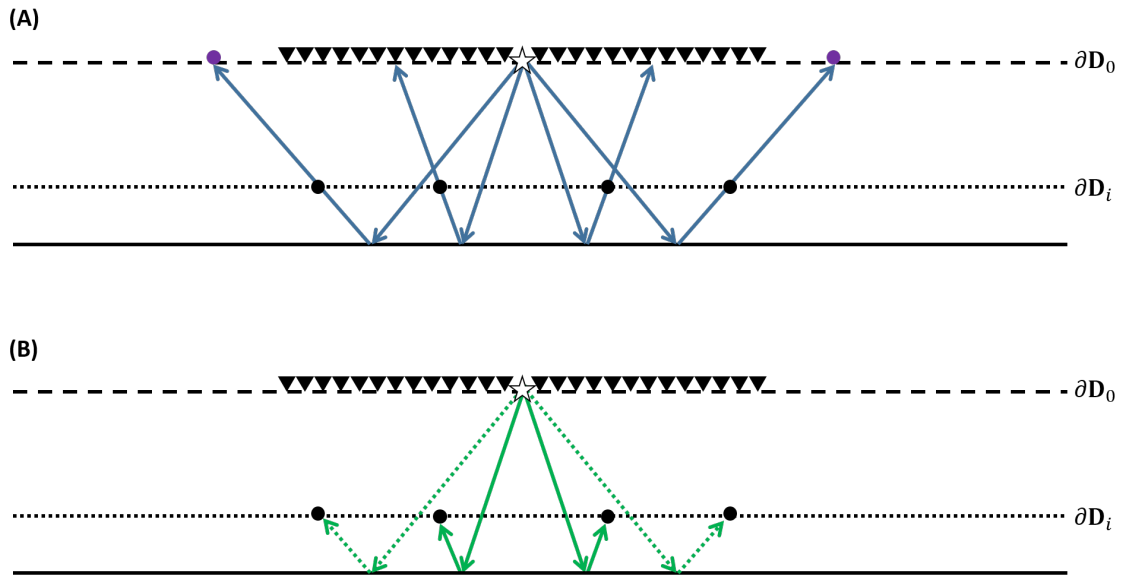


Figure 2-9: Illustration of the stationary points. (A) Reflection response (blue) due to a source (white star) located at $\partial\mathbb{D}_0$. The triangles represent the acquisition surface at $\partial\mathbb{D}_0$. The black solid circles represent focal points at $\partial\mathbb{D}_i$, while the purple ones represent stationary points at $\partial\mathbb{D}_0$ that are outside the acquisition surface. (B) The retrieved parts (solid green) and lost parts (dotted green) of function $G^{-,+}$.

2-5 Marchenko redatuming

As explained in the previous section, the Green's functions $G^{-,+}(\mathbf{x}_0'', \mathbf{x}'_i, t)$ and $G^{-,-}(\mathbf{x}_0'', \mathbf{x}'_i, t)$ are interpreted as the responses of a source point located at \mathbf{x}'_i and observed at \mathbf{x}_0'' , see [Figure 2-10A](#). According to the source-receiver reciprocity theorem ([Wapenaar and Berkhout, 1989](#)), the functions can alternatively be expressed as

$$G^{-,+}(\mathbf{x}_0'', \mathbf{x}'_i, t) = G^{-,+}(\mathbf{x}'_i, \mathbf{x}_0'', t), \quad (2-32)$$

$$G^{-,-}(\mathbf{x}_0'', \mathbf{x}'_i, t) = -G^{+,+}(\mathbf{x}'_i, \mathbf{x}_0'', t). \quad (2-33)$$

The Green's functions $G^{-,+}(\mathbf{x}'_i, \mathbf{x}_0'', t)$ and $G^{+,+}(\mathbf{x}'_i, \mathbf{x}_0'', t)$ are interpreted as the responses of source points at \mathbf{x}_0'' and a receiver at \mathbf{x}'_i , see [Figure 2-10B](#). These two Green's functions are related to a reflection response that is located at the focal level according to ([Wapenaar et al., 2014b](#))

$$G^{-,+}(\mathbf{x}_i, \mathbf{x}_0'', t) = \int_{\partial\mathbb{D}_i} \int_{-\infty}^{\infty} R(\mathbf{x}_i, \mathbf{x}'_i, t-t') G^{+,+}(\mathbf{x}'_i, \mathbf{x}_0'', t') dt' d\mathbf{x}'_i, \quad (2-34)$$

where $R(\mathbf{x}_i, \mathbf{x}'_i, t)$ is the reflection response due to the virtual source at \mathbf{x}'_i and measured at \mathbf{x}_i . The response $R(\mathbf{x}_i, \mathbf{x}'_i, t)$ is estimated by the multidimensional deconvolution (MDD) which involves inverting [Equation 2-34](#) as follows

$$R(\mathbf{x}_i, \mathbf{x}'_i, t) = \int_{\partial\mathbb{D}_0} G^{-,+}(\mathbf{x}_i, \mathbf{x}_0'', t) * [G^{+,+}(\mathbf{x}'_i, \mathbf{x}_0'', t)]^{inv} d\mathbf{x}_0'', \quad (2-35)$$

where the abbreviation *inv* stands for the inverse of $G^{+,+}$, and the asterisk denotes temporal convolution. [Equation 2-35](#) does not only produce the redatumed response at $\partial\mathbb{D}_i$ but also removes the overburden effects between $\partial\mathbb{D}_0$ and $\partial\mathbb{D}_i$, see [Figure 2-11B](#). Additionally, the deconvolution process compensates significantly for the amplitude errors in the Green's functions, related to approximating the direct arrival of the inverse transmission response by the time-reversal of the direct arrival of the Green's function ([Wapenaar et al., 2014b](#)). Consequently, the redatumed reflection response $R(\mathbf{x}_i, \mathbf{x}'_i, t)$ can be used to extract the correct angle-dependent reflectivity. This information can then be used as input for AVO inversion to determine the detailed medium parameters in the zone of interest. The MDD process is typically carried out in the space-frequency domain ($x-\omega$) as a least-squares matrix inversion. This process can sometimes be unstable and requires stabilization ([Minato et al., 2013](#)). The inverse problem can be expressed as follows

$$\hat{\mathbf{R}} = \frac{\hat{\mathbf{G}}^{-,+} [\hat{\mathbf{G}}^{+,+}]^H}{\hat{\mathbf{G}}^{+,+} [\hat{\mathbf{G}}^{+,+}]^H + \mathbf{e}}, \quad (2-36)$$

where $\hat{\mathbf{R}}$, represents the matrix containing $\hat{R}(\mathbf{x}_i, \mathbf{x}'_i, \omega)$, $\hat{\mathbf{G}}^{+,+}$, represents the matrix containing $\hat{G}^{+,+}(\mathbf{x}'_i, \mathbf{x}_0'', \omega)$, $\hat{\mathbf{G}}^{-,+}$ represents the matrix containing $\hat{G}^{-,+}(\mathbf{x}_i, \mathbf{x}_0'', \omega)$, \mathbf{e} is a small positive real constant known as the stabilization parameter, and the capital H superscript indicates the Hermitian transpose (conjugate transpose). Alternatively, for a laterally invariant medium, the deconvolution process can be carried out in the wavenumber-frequency ($k_x-\omega$) as a spectral division as follows

$$\tilde{R}(k_x, z_i, \omega) = \frac{\tilde{G}^{-,+}(k_x, z_i, \omega)}{\tilde{G}^{+,+}(k_x, z_i, \omega)}, \quad (2-37)$$

where $\tilde{R}(k_x, z_i, \omega)$ is the re-datuned reflection response in the wavenumber-frequency domain. Similar to Equation 2-36, the errors related to the transmission losses will be cancelled in this process. The spectral division can also be unstable when $\tilde{G}^{+,+}(k_x, z_i, \omega)$ is very small. The solution can be regularized as follows

$$\tilde{R}(k_x, z_i, \omega) = \frac{\tilde{G}^{-,+}(k_x, z_i, \omega) [\tilde{G}^{+,+}(k_x, z_i, \omega)]^*}{|\tilde{G}^{+,+}(k_x, z_i, \omega)|^2 + e}, \quad (2-38)$$

where the bar on each side of $\tilde{G}^{+,+}$ indicates the modulus of $\tilde{G}^{+,+}$, and asterisk superscript indicates complex conjugate. In the next chapter, the estimation of the angle-dependent reflectivity from the results obtained by Equation 2-36 and Equation 2-37 will be explained.

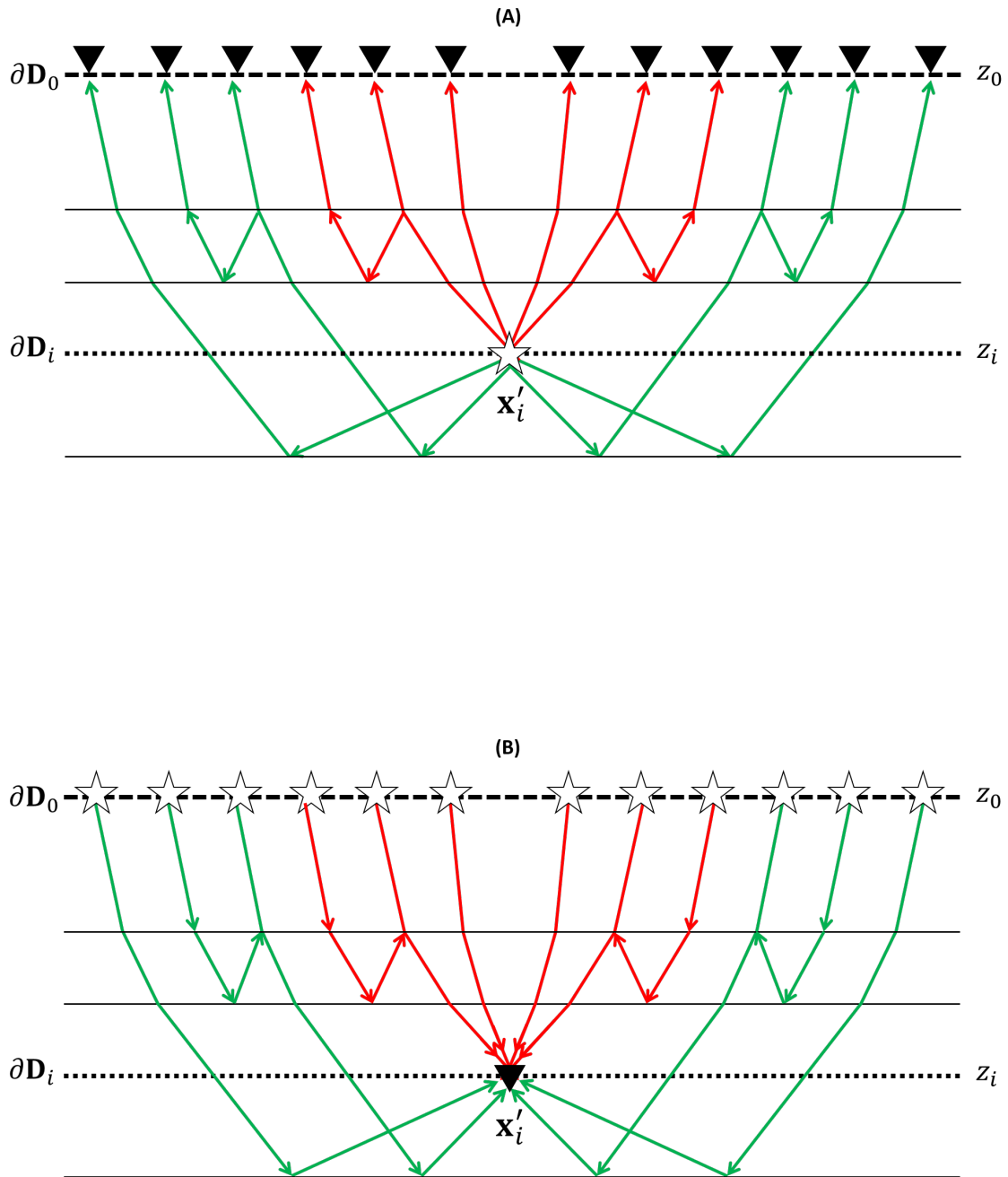


Figure 2-10: Source-receiver reciprocity theorem. (A) $G^{-,+}$ (green) and $G^{-,-}$ (red) are the responses of a source point located at \mathbf{x}'_i and observed at \mathbf{x}'_0 . (B) $G^{-,+}$ (green) and $G^{+,+}$ (red) are the responses of source points located at \mathbf{x}'_0 and observed at \mathbf{x}'_i

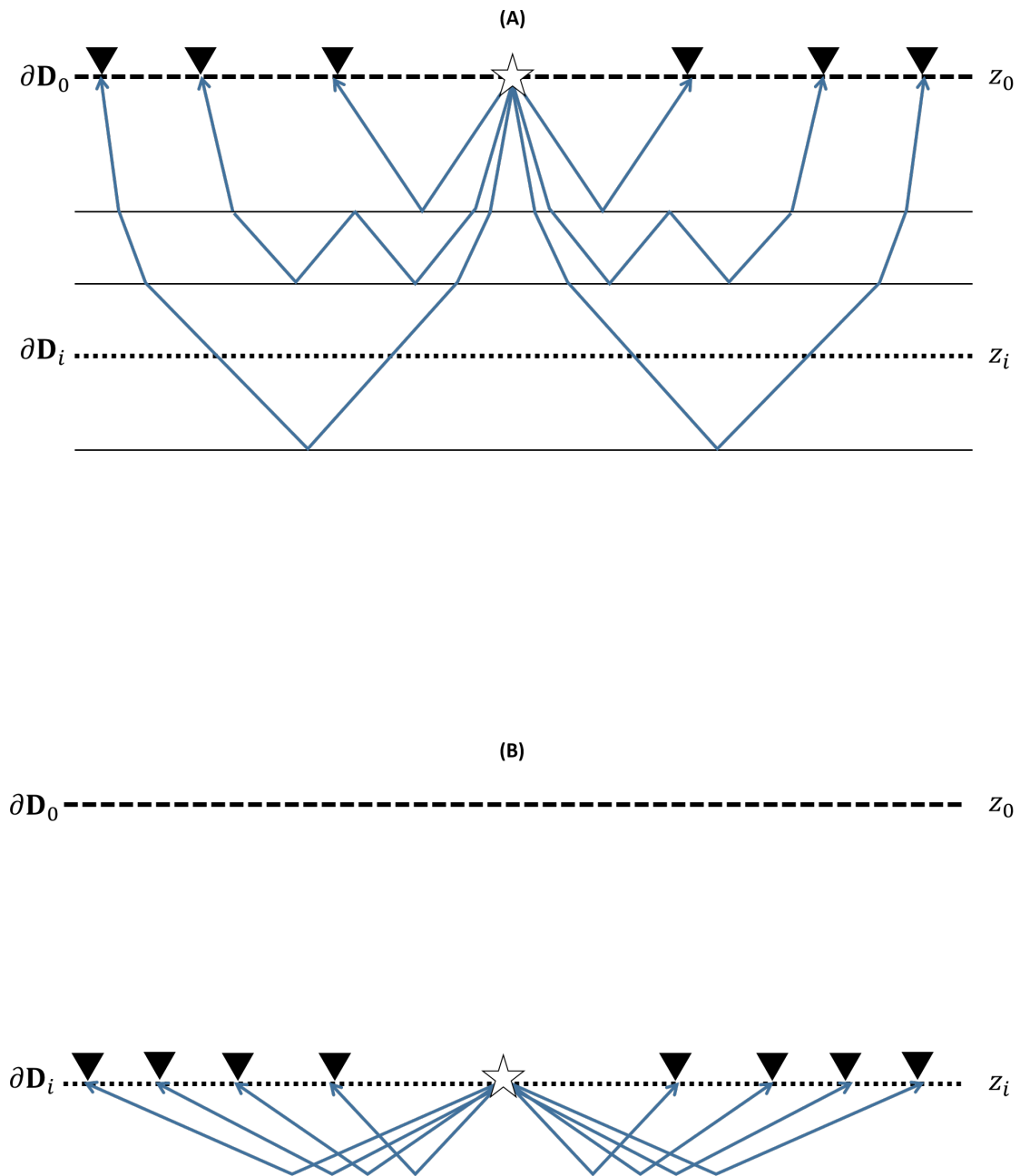


Figure 2-11: Illustration of the source-receiver redatuming using MDD. (A) Surface reflection response. (B) Redatumed reflection response. Note that the overburden has been completely removed.

Chapter 3

Imaging angle-dependent reflectivity

3-1 Properties of the angle-dependent reflectivity

The angle-dependent reflectivity for two homogeneous acoustic half-spaces separated by an interface located at z_i is given by (De Bruin et al., 1990)

$$r(z_i, \theta) = \frac{\rho_2 c_2 \cos \theta - \rho_1 \sqrt{c_1^2 - c_2^2 \sin^2 \theta}}{\rho_2 c_2 \cos \theta + \rho_1 \sqrt{c_1^2 - c_2^2 \sin^2 \theta}}, \quad (3-1)$$

where θ is the angle of incidence. The subscript 1 refers to the upper half-space, and 2 refers to the lower half-space, see [Figure 3-1](#). The value of r ranges from -1 to 1 , where a negative r means the upper half-space has higher acoustic impedance than the lower half-space and a positive r means the lower half-space has higher acoustic impedance than the upper half-space. A total reflection occurs when $r = 1$ or $r = -1$, whereas a total transmission occurs when $r = 0$. If $c_1 < c_2$, the reflectivity becomes a complex value (i.e. consisting of real and imaginary parts) for

$$\sin |\theta| > c_1/c_2. \quad (3-2)$$

A total internal reflection with a magnitude of 1 occurs after the critical angle, see [Figure 3-2](#). The critical angle is defined as

$$\theta_c = \sin^{-1}(c_1/c_2). \quad (3-3)$$

For $|\theta| > \theta_c$, the lower half-space can support an evanescent wavefield only, that is, one whose amplitude decays as z increases ([Wapenaar and Berkhout, 1989](#)). For an interface between two acoustic homogeneous half-spaces with $c_1 = 1500$ m/s, $c_2 = 2000$ m/s, $\rho_1 = 1000$ kg/m³, and $\rho_2 = 1500$ kg/m³, the modulus of $r(\theta, z_i)$ is shown in [Figure 3-3A](#). If $c_1 > c_2$, the critical angle does not exist. In this case, the reflectivity is always real for $|\theta| \leq 90^\circ$. For an interface between two acoustic homogeneous half-spaces with $c_1 = 2000$ m/s, $c_2 = 1500$ m/s, $\rho_1 = 1000$ kg/m³, and $\rho_2 = 1500$

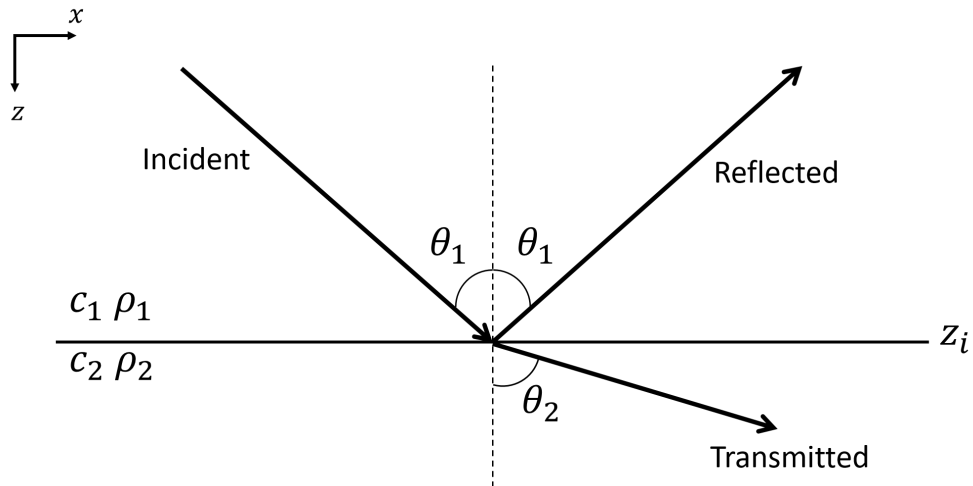


Figure 3-1: Reflection of an incident downgoing plane wave at an interface (horizontal line) between two acoustic homogeneous half-spaces. The arrow represents the path of the wave. The vertical dashed line represents the normal. Snell's law describes the relationship between the angles of incidence θ_1 and transmission θ_2 .

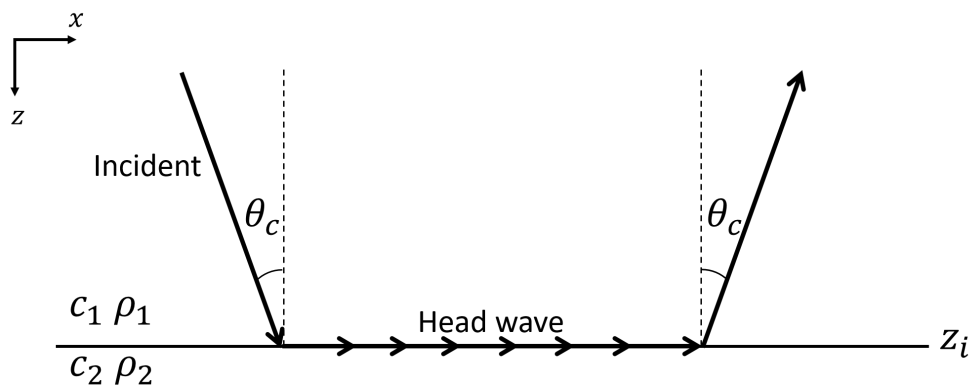


Figure 3-2: A refracted wave that enters and leaves a high-velocity medium at the critical angle is known as a head wave. Here, the angle of refraction approaches 90° , at which the refracted ray becomes parallel to the interface. Beyond the critical angle, the lower half-space supports an evanescent wave only.

kg/m³, the modulus of $r(\theta, z_i)$ is shown in Figure 3-3B. When there is a density contrast only (i.e. $\rho_1 \neq \rho_2$ and $c_1 = c_2$), the reflection function becomes angle independent, according to De Bruin et al. (1990)

$$r(z_i) = \frac{\rho_2 - \rho_1}{\rho_2 + \rho_1}. \quad (3-4)$$

In this expression, the reflectivity is equivalent to the normal-incidence reflectivity. For an interface between two acoustic homogeneous half-spaces with $c_1 = c_2 = 2000$ m/s, $\rho_1 = 1000$ kg/m³, and $\rho_2 = 1500$ kg/m³, the modulus of $r(\theta, z_i)$ equals 0.2 for all angles.

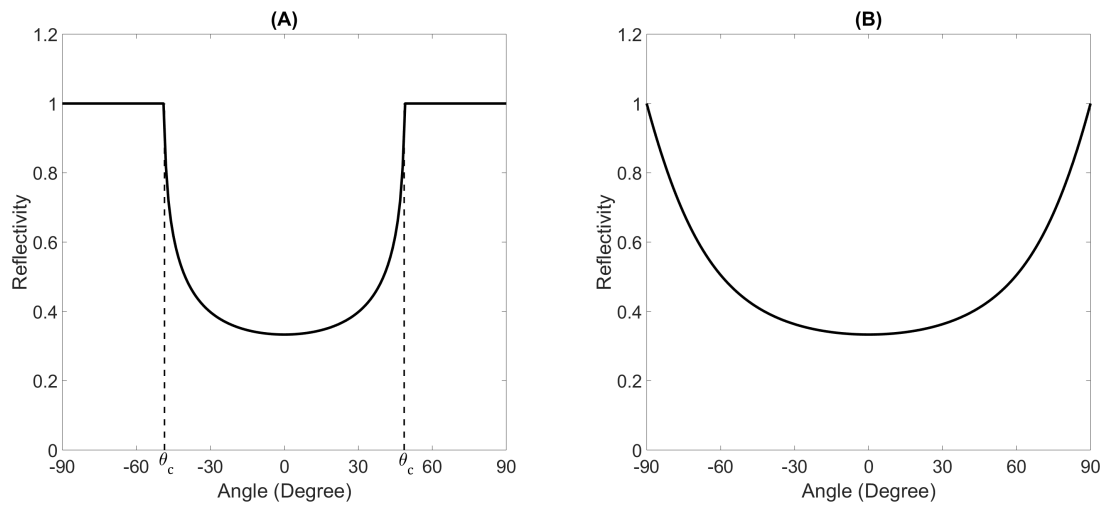


Figure 3-3: Reflection coefficient in angle domain. (A) Angle-dependent reflectivity with $c_1 < c_2$. Note that the evanescent wave occurs after θ_c with amplitude of 1. (B) Angle-dependent reflectivity with $c_1 > c_2$. Only the moduli have been plotted.

In the wavenumber-frequency domain, the reflection operator can be expressed as follows (De Bruin et al., 1990)

$$\tilde{r}(k_x, z_i, \omega) = \frac{\rho_2 \sqrt{k_1^2 - k_x^2} - \rho_1 \sqrt{k_2^2 - k_x^2}}{\rho_2 \sqrt{k_1^2 - k_x^2} + \rho_1 \sqrt{k_2^2 - k_x^2}}, \quad (3-5)$$

where

$$k_x = k_1 \sin \theta, \quad (3-6a)$$

with

$$k_1 = \omega/c_1, \quad (3-6b)$$

$$k_2 = \omega/c_2. \quad (3-6c)$$

Note that $\tilde{r}(k_x, z_i, \omega)$ is frequency-dependent in contrast with $r(z_i, \theta)$. If $c_1 < c_2$, the wavenumber-domain reflection operator becomes complex for $k_2 < |k_x| < k_1$, as shown in Figure 3-4. On the other

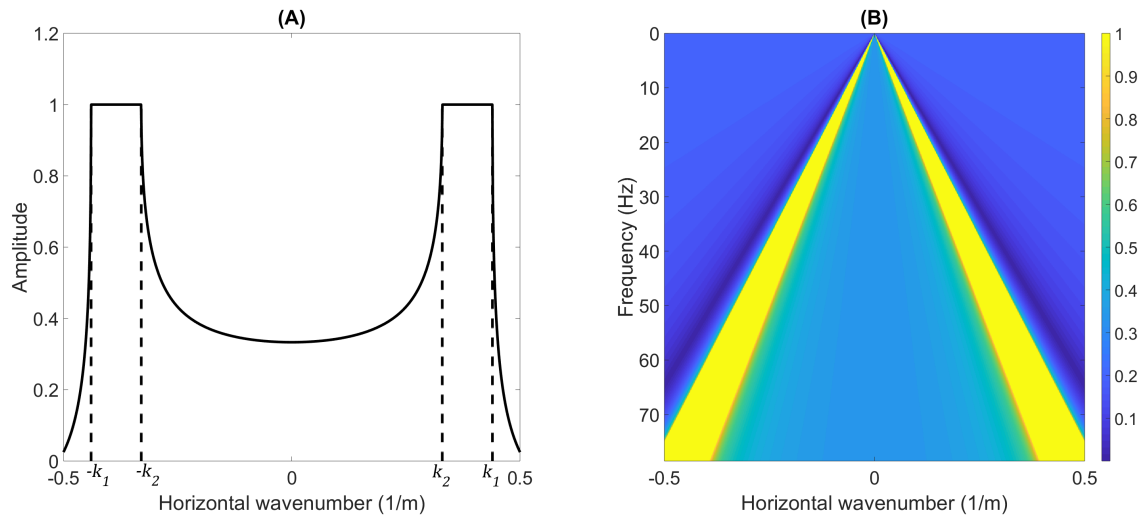


Figure 3-4: Reflection operator in the wavenumber-frequency domain with $c_1 < c_2$. (A) The modulus of \hat{r} for a single-frequency of $f = 70$ Hz. The total reflection occurs for $k_2 < |k_x| < k_1$ with amplitude of 1. The evanescent wavefield occurs for all $|k_x| > k_1$. (B) Wavenumber-frequency spectrum of the reflection operator. Note that the total reflection occurs within the yellow area with amplitude of 1. Only the moduli have been plotted.

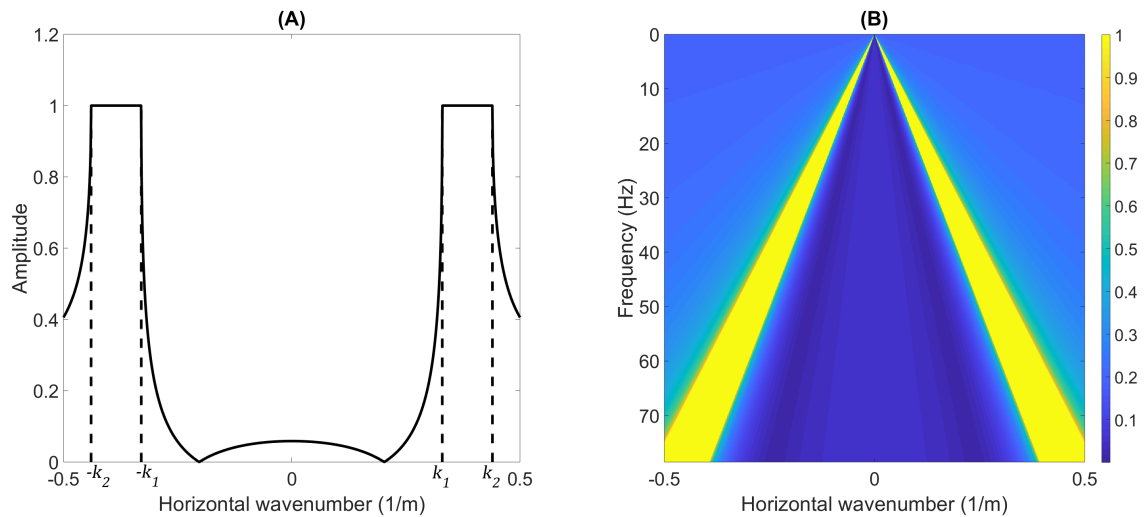


Figure 3-5: Reflection operator in the wavenumber-frequency domain with $c_1 > c_2$. (A) The modulus of \hat{r} for a single-frequency of $f = 70$ Hz. The total reflection occurs for $k_1 < |k_x| < k_2$ with amplitude of 1. The evanescent wavefield occurs for all $|k_x| > k_2$. (B) Wavenumber-frequency spectrum of the reflection operator. Note that the total reflection occurs within the yellow area with amplitude of 1. Only the moduli have been plotted.

hand, if $c_1 > c_2$, the wavenumber-domain reflection operator becomes complex for $k_1 < |k_x| < k_2$, as shown in Figure 3-5. Beyond the maximum bounds in both situations the wavenumber-domain reflection operator is real and acts on the evanescent waves only (Wapenaar and Berkhout, 1989).

In the ray-parameter domain, the reflection operator can be expressed as follows (De Bruin, 1992)

$$\check{r}(p, z_m) = \frac{\rho_2 \sqrt{1/c_1^2 - p^2} - \rho_1 \sqrt{1/c_2^2 - p^2}}{\rho_2 \sqrt{1/c_1^2 - p^2} + \rho_1 \sqrt{1/c_2^2 - p^2}} \quad (3-7)$$

where p is the ray parameter (slowness) given by

$$p = \frac{k_x}{\omega} = \frac{\sin \theta}{c_1} = \frac{1}{c_x}. \quad (3-8)$$

The breve denotes the ray-parameter domain. For the situation that $c_1 < c_2$, the value of $\check{r}(p, z_i)$ becomes complex for $1/c_2 < |p| < 1/c_1$, as shown in Figure 3-6A. For the situation that $c_1 > c_2$, the value of $\check{r}(p, z_i)$ becomes complex for $1/c_1 < |p| < 1/c_2$, as shown in Figure 3-6B. Note that $r(\theta, z_i)$ and $\check{r}(p, z_i)$ are frequency independent whereas $\tilde{r}(k_x, z_i, \omega)$ is frequency dependent. The three reflection functions will be used in chapter 4 for the verification of the imaged angle dependent reflection properties.

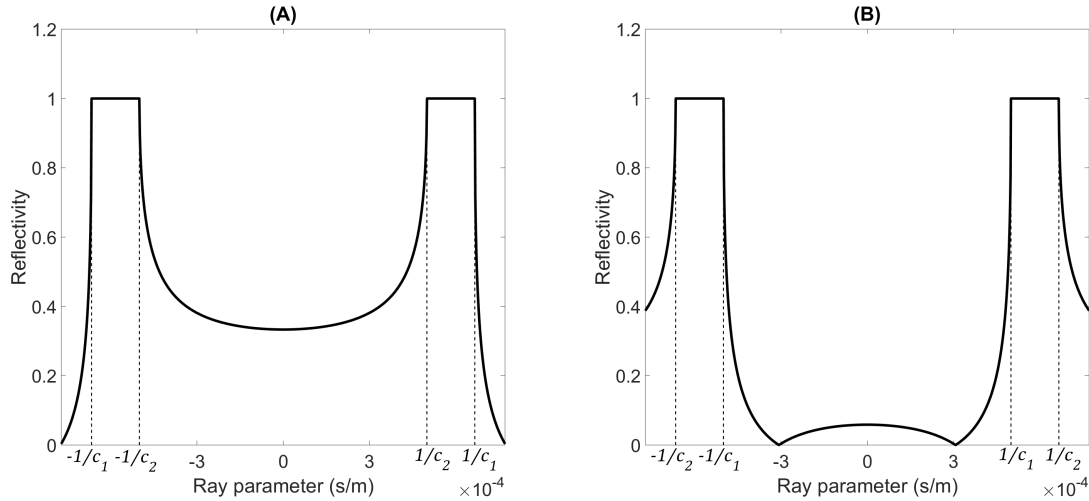


Figure 3-6: Reflection operator in the ray-parameter domain. (A) The modulus of \check{r} with $c_1 < c_2$. The total reflection occurs for $1/c_2 < |p| < 1/c_1$ with amplitude of 1. The evanescent wavefield occurs for all $|p| > 1/c_1$. (B) The modulus of \check{r} with $c_1 > c_2$. The total reflection occurs for $1/c_1 < |p| < 1/c_2$ with amplitude of 1. The evanescent wavefield occurs for all $|p| > 1/c_2$

3-2 Imaging principle

According to Wapenaar and Berkhout (1989), the measured wavefield at a certain depth level in the subsurface can be decomposed into upgoing and downgoing wavefields. When the first arrival of the upgoing and downgoing wavefields coincide in time and space, a reflector exists (Claerbout, 1971).

In other words, when the redatuming level intersects the reflector, the imaging condition will return a non-zero amplitude. This holds for impulse responses but for band-limited data there will be some overlap due to wavelet thickness. Typically, the imaging process is carried out recursively through the subsurface with small depth steps. For each lateral position, the upgoing wavefield is deconvolved with the downgoing wavefield in the space-frequency domain or in the wavenumber-frequency domain (Berkhout, 1985). In order to extract the angle-dependent reflectivity, the imaging principle has to be extended by adding all frequency components along lines of constant ray parameter or angle (De Bruin et al., 1990). By using the Marchenko method, the procedure is implemented as follows:

1. *Estimating the downgoing and upgoing wavefields.* At every depth level z_i , the upgoing wavefield $G^{-,+}(\mathbf{x}'_i, \mathbf{x}''_0, t)$ and downgoing wavefield $G^{+,+}(\mathbf{x}'_i, \mathbf{x}''_0, t)$ are estimated for every lateral position by employing to the coupled Marchenko equations (Equation 2-21 and Equation 2-22).
2. *Deconvolving the upgoing wavefield with the downgoing wavefield.* The first arrivals of $G^{-,+}(\mathbf{x}'_i, \mathbf{x}''_0, t)$ and $G^{+,+}(\mathbf{x}'_i, \mathbf{x}''_0, t)$ are isolated and transformed into the space-frequency domain $(x-\omega)$ using to Equation 2-1. After that, the deconvolution process is carried out using Equation 2-36 to obtain the reflectivity in the space-frequency domain. In practice, the frequency ω is bounded according to $-\omega_N < \omega < +\omega_N$, where ω_N is the Nyquist frequency. The frequency sampling $\Delta\omega$ is given by

$$\Delta\omega = \frac{2\pi}{\Delta t N_t}, \quad (3-9)$$

where Δt is the temporal sampling, and N_t is the number of samples in the time domain.

3. *Transforming into the wavenumber-frequency domain.* The result obtained from the previous step is transformed into the wavenumber-frequency domain $(k_x-\omega)$, using to Equation 2-3. In practice, the wavenumber k_x is bounded according to $-k_N < k_x < +k_N$, where k_N is the spatial Nyquist frequency. The wavenumber sampling Δk_x is given by

$$\Delta k_x = \frac{2\pi}{\Delta x N_x}, \quad (3-10)$$

where Δx is the spatial sampling, and N_x is the number of samples in the space domain.

4. *Mapping the horizontal wavenumber k_x into ray parameter p or angle θ .* In order to preserve the angle dependent reflection information in the imaging step all frequency contributions, which are represented as complex values, must be summed along lines of constant ray parameter. If the variable k_x is replaced by p according to,

$$\tilde{R}(k_x, z_i, \omega) \rightarrow \check{R}(p, z_i, \omega), \quad (3-11)$$

then imaging can be carried out in the ray parameter-frequency domain along lines of constant p . Here, $\check{R}(p, z_i, \omega)$ is the frequency contributions mapped into the ray parameter domain (i.e. $p - \omega$ spectrum). Instead of carrying out the process in the ray parameter domain, the process can also be carried out in the angle domain by replacing the variable k_x by θ according to

$$\tilde{R}(k_x, z_i, \omega) \rightarrow R(\theta, z_i, \omega). \quad (3-12)$$

where $R(\theta, z_i, \omega)$ is the frequency contributions mapped into the angle domain (i.e. $\theta - \omega$ spectrum). The mapping process is performed by a simple interpolation process (De Bruin, 1992). In the ray-parameter domain, the interpolation process consists of the following steps:

- The variable k_x is replaced by p for every single frequency using Equation 3-8.
- The range of p is defined as $(-p_{max}, p_{max})$, where p_{max} is the maximum slowness. The range should only span the dip components of interest in the data. As a rule of thumb, $p_{max} = 1/\min(c)$ (Yilmaz, 2001).
- The number of samples in the ray parameter domain N_p equals N_x .
- The increment in the ray parameter domain Δp is calculated as follows

$$\Delta p = \frac{2p_{max}}{N_p}. \quad (3-13)$$

- The frequency contributions $\tilde{R}(k_x, z_i, \omega)$ and p are used as input in a linear interpolation process to obtain the $p - \omega$ spectrum, as shown in Figure 3-7

Similarly, the process in the angle domain consists of the following steps:

- The variable k_x is replaced by θ for every single frequency using Equation 3-8. Because some of the angles will be complex values, the real part will be considered only: $\text{Re}\{\theta\}$.
- The range of θ is defined as $(-90^0, 90^0)$.
- The number of samples in angle domain N_θ equals N_x .
- The increment in the angle domain $\Delta\theta$ is calculated as follows

$$\Delta\theta = \frac{180^0}{N_x}. \quad (3-14)$$

- The frequency contributions $\tilde{R}(k_x, z_i, \omega)$ and $\text{Re}\{\theta\}$ are used as input in a linear interpolation process to obtain the $\theta - \omega$ spectrum, as shown in Figure 3-8

5. *Summing all frequency contributions (positive frequencies only).* For every value of p or θ , a complex averaging of all positive frequency contributions is applied according to (De Bruin, 1992)

$$\langle \check{r}(p, z_i) \rangle = \frac{1}{N_\omega} \sum_{n=1}^{N_\omega} \check{R}(p, z_i, \omega_n), \quad (3-15)$$

$$\langle r(\theta, z_i) \rangle = \frac{1}{N_\omega} \sum_{n=1}^{N_\omega} R(\theta, z_i, \omega_n), \quad (3-16)$$

where N_ω represents the number of positive frequency components, n is the index of summation, and the angle bracket indicates approximation. The result is a true amplitude estimate of the angle-dependent reflectivity, as shown in Figure 3-9B and Figure 3-10B. Bear in mind that the angle-dependent reflectivity information is contained in the complex value (i.e. the real and imaginary parts). The amplitude of the reflectivity can be obtained by estimating the modulus, and its polarity is derived from the real part. When the summation is carried out in the wavenumber-frequency domain, the reflectivity information is distorted, as shown in Figure 3-9A and Figure 3-10A.

6. Repeat the same process for each depth level of interest. By repeating this procedure for each depth level of interest, $z - p$ panel or $z - \theta$ panel is obtained, as shown in Figure 3-11. The panel represents an image of the angle-dependent reflectivity as a function of depth. By picking procedure, the angle-dependent reflectivity can be obtained, as shown in Figure 3-12.

As explained in section 2-5, the deconvolution process can be also carried out in the wavenumber-frequency domain. The procedure can be explained explicitly as follows:

1. Estimating the downgoing and upgoing wavefields. At every depth level, the upgoing wavefield $G^{-,+}(\mathbf{x}'_i, \mathbf{x}''_0, t)$ and downgoing wavefield $G^{+,+}(\mathbf{x}'_i, \mathbf{x}''_0, t)$ using the coupled Marchenko equations (Equation 2-21 and Equation 2-22).
2. Transforming into the wavenumber-frequency domain. The first arrivals of $G^{-,+}(\mathbf{x}'_i, \mathbf{x}''_0, t)$ and downgoing wavefield $G^{+,+}(\mathbf{x}'_i, \mathbf{x}''_0, t)$ are isolated and transformed into the wavenumber-frequency domain ($k_x - \omega$) using Equation 2-3.
3. Deconvolving the upgoing wavefield with the downgoing wavefield. The upgoing wavefield is deconvolved with the downgoing wavefield using Equation 2-37.
4. Mapping the horizontal wavenumber k_x into ray parameter p or angle θ . The mapping process is applied to $\tilde{R}(k_x, z_i, \omega)$ as described by Equation 3-11 and Equation 3-12.
5. Summing all frequency contributions (positive frequencies only). The true reflectivity is obtained using Equation 3-15 and Equation 3-16.
6. Repeat the same process for each depth level of interest.

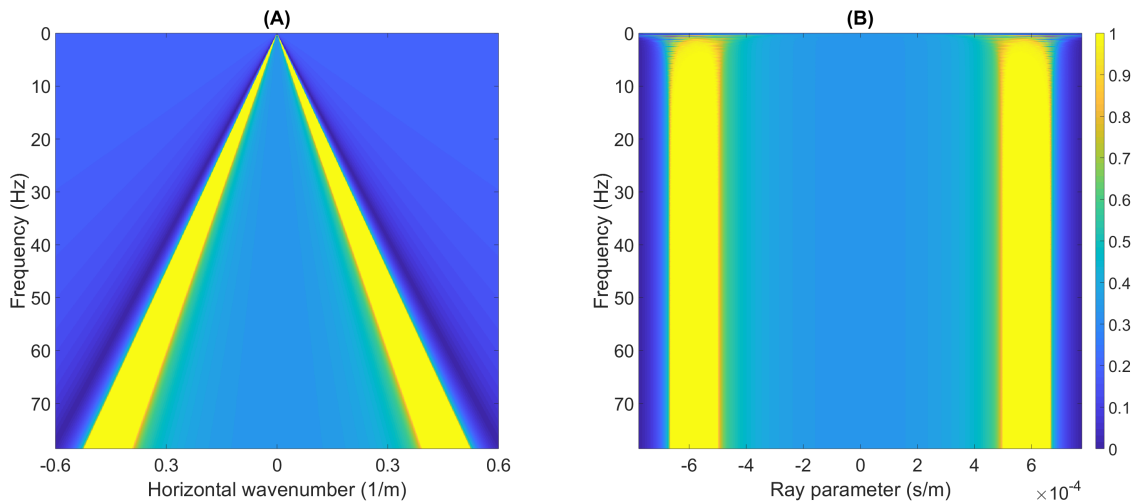


Figure 3-7: Mapping the variable k_x into ray parameter p using a linear interpolation process. (A) Wavenumber-frequency domain with $c_1 = 1500$ m/s, $c_2 = 2000$ m/s, $\rho_1 = 1000$ kg/m³, and $\rho_2 = 1500$ kg/m³. (B) Ray-parameter-frequency domain obtained by the mapping process explained in the main text. Only the moduli have been plotted.

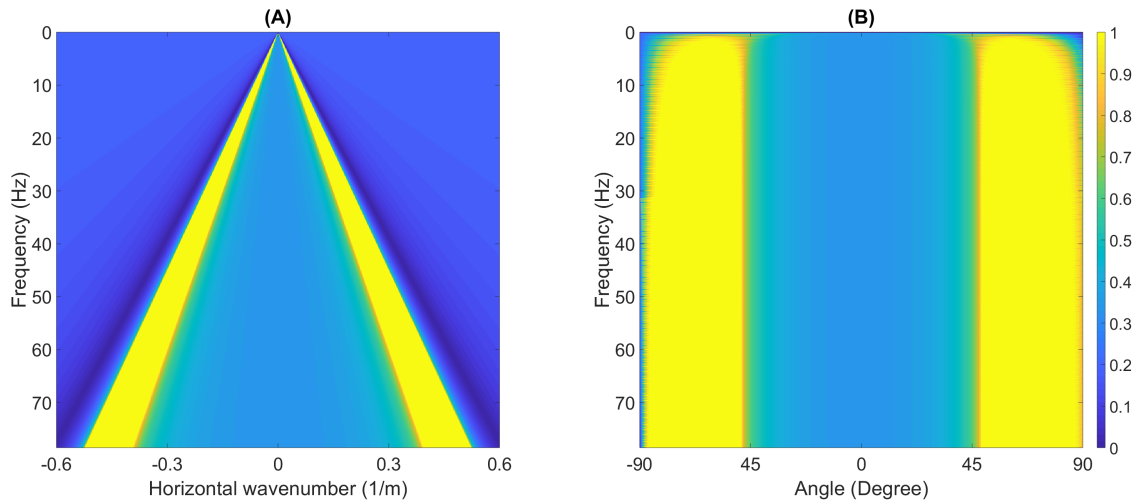


Figure 3-8: Mapping the variable k_x into angle θ using a linear interpolation process. (A) Wavenumber-frequency domain with $c_1 = 1500$ m/s, $c_2 = 2000$ m/s, $\rho_1 = 1000$ kg/m³, and $\rho_2 = 1500$ kg/m³. (B) Angle-frequency domain obtained by the mapping process explained in the main text. Only the moduli have been plotted.

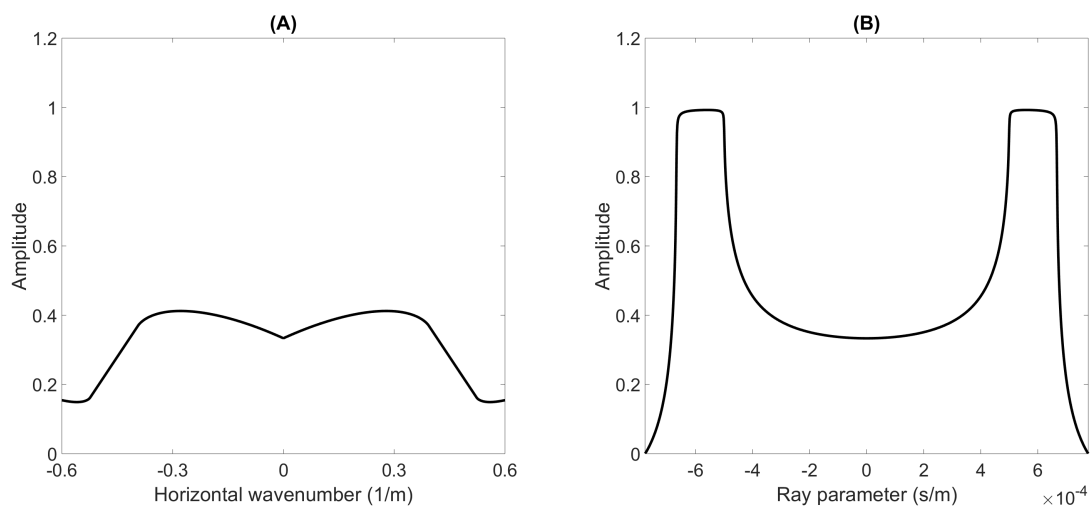


Figure 3-9: Summation of all positive frequency components along lines of constant (A) wavenumber and (B) ray parameter. Note that the reflectivity is preserved in (B) whereas it is distorted in (A). These results are based on Figure 3-7.

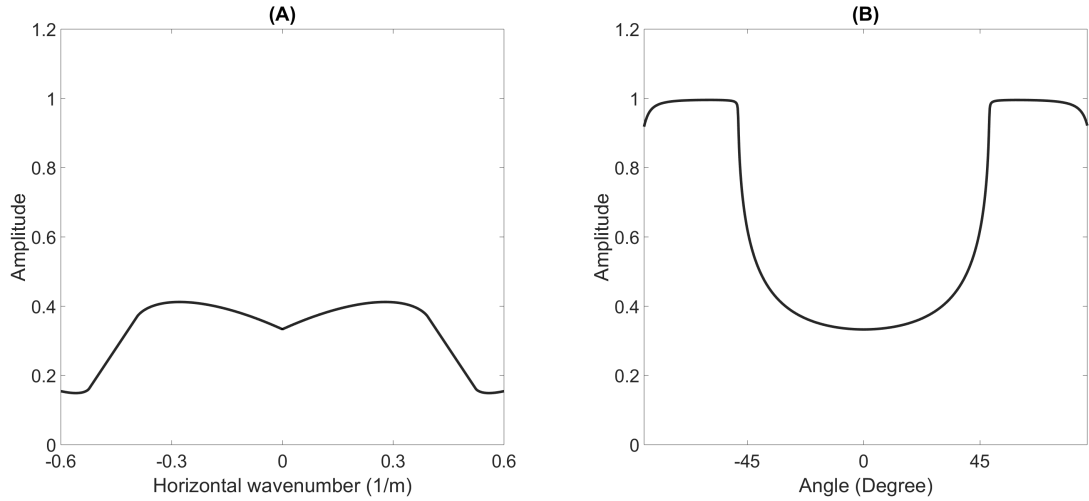


Figure 3-10: Summation of all positive frequency components along lines of constant (A) wavenumber and (B) angle. Note that the reflectivity is preserved in (B) whereas it is distorted in (A). These results are based on Figure 3-8.

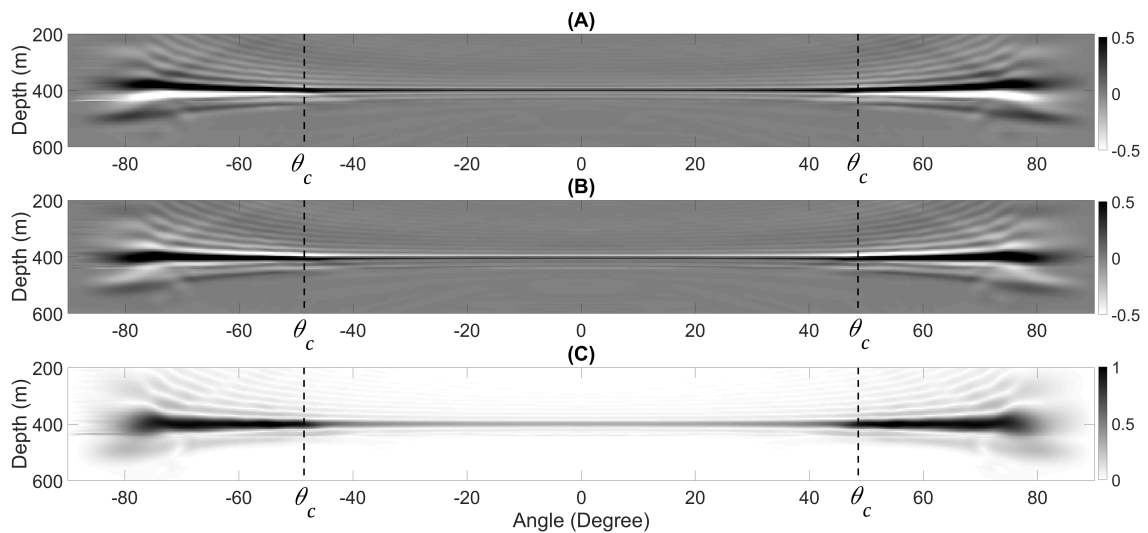


Figure 3-11: Imaged angle-dependent reflectivity for a two-layer acoustic medium with $c_1 = 1500$ m/s, $c_2 = 2000$ m/s, $\rho_1 = 1000$ kg/m³, and $\rho_2 = 1500$ kg/m³. The reflector is located at 400m. The imaging process has been applied with a depth step of 5m. (A) Image of the real part. Note that the polarity is positive. (B) Image of the imaginary part. (C) Image of the moduli.

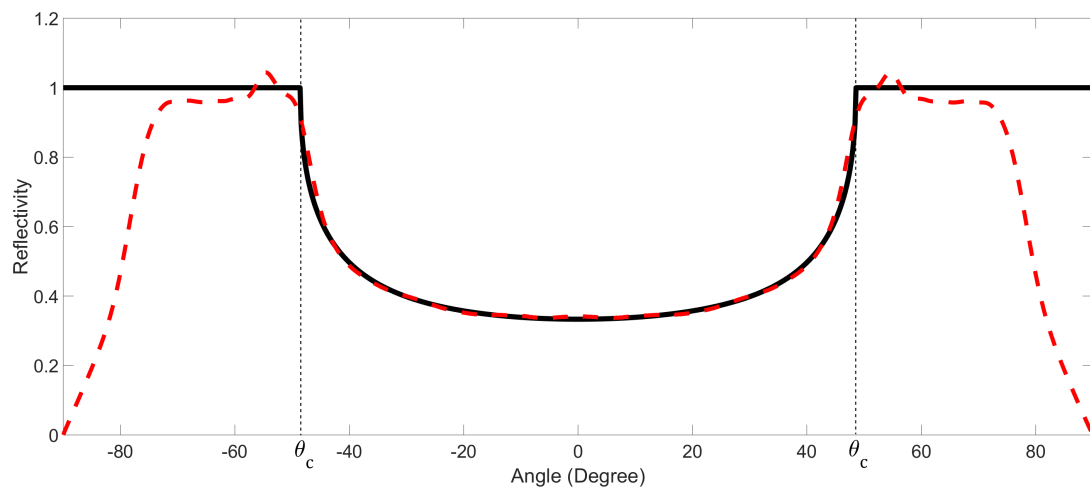


Figure 3-12: Estimated angle-dependent reflectivity obtained by picking procedure along the event in Figure 3-11C. The polarity is derived from Figure 3-11A. Note that the estimated reflectivity (dashed red) matches the exact one (solid black) very well up to the critical angle.

Chapter 4

Numerical examples

In this chapter, the imaging process explained in the previous chapter will be demonstrated with numerical examples based on 1.5 acoustic layered models. Each numerical example introduces a particular aspect for which the approach is tested using the Marchenko and standard imaging. The estimated angle-dependent reflectivity will be compared to the analytic expressions (Equation 3-1 and Equation 3-7) for verification. In the first two numerical examples, the imaging process will be demonstrated explicitly to understand the workflow shown in Figure 4-1. The workflow summarizes the procedures that have been explained in the previous chapter.

The reflection data $R(\mathbf{x}_0'', \mathbf{x}_0, t)$ and direct arrival $G_d(\mathbf{x}_0'', \mathbf{x}'_i, t)$ are obtained through numerical modelling, using a finite-difference program (Thorbecke and Draganov, 2010). The input source signature $S(t)$ used to model $R(\mathbf{x}_0'', \mathbf{x}_0, t)$ and $G_d(\mathbf{x}_0'', \mathbf{x}'_i, t)$ is approximately a sinc function with a flat spectrum of amplitude 1 between 5 Hz and 80 Hz, as shown in Figure 4-2. A shift of 0.3 s is added to the source wavelet to make it casual and suitable for the finite-difference scheme. The reflection data and direct arrival have a temporal sampling of 4 ms, with a maximum recording time of 4 s. The recording of the data is delayed with 0.3 s to place the peak of the wavelet at the correct time. For better visualization, the wavefields shown in the $t - x$ plots are convolved with a Ricker wavelet with a peak frequency of 25 Hz. The reflection data are modeled with 1001 dipole sources located at the surface and recorded by 1001 monopole receivers located at the surface as well. For both sources and receivers, the spatial sampling is 5 m, with offset range from -2500 m to 2500 m in the x direction. The free-surface multiples are not modeled and the direct wave is removed from the modeled reflection data. The direct arrivals are modeled with 1001 monopole sources located in the subsurface at the same depth and recorded by 1001 monopole receivers at the surface. The same spatial sampling and offset range of the reflection data are used.

The Marchenko method is applied using the iterative implementation by Thorbecke et al. (2017). The program requires the reflection data $R(\mathbf{x}_0'', \mathbf{x}_0, t)$ and direct arrival $G_d(\mathbf{x}_0'', \mathbf{x}'_i, t)$ as input to estimate the functions $G^{-,+}(\mathbf{x}_0'', \mathbf{x}'_i, t)$, $G^{-,-}(\mathbf{x}_0'', \mathbf{x}'_i, t)$, $f_1^+(\mathbf{x}_0'', \mathbf{x}'_i, t)$, $f_1^-(\mathbf{x}_0'', \mathbf{x}'_i, t)$, and $f_2(\mathbf{x}'_i, \mathbf{x}_0'', t)$. The number of iterations required for convergence depends on the reflectivity and number of events in the model (Thorbecke et al., 2017). The program also gives the option to apply standard redatuming by setting the number of iterations to zero. In this case, the function $f_1^+(\mathbf{x}_0'', \mathbf{x}'_i, t)$ is entirely equivalent to the time-reversed direct arrival $G_d(\mathbf{x}_0'', \mathbf{x}'_i, -t)$. Because the direct arrivals $G_d(\mathbf{x}_0'', \mathbf{x}'_i, t)$ are estimated

from monopole sources, the estimated Green's functions $G^{-,+}(\mathbf{x}_0'', \mathbf{x}_i', t)$ and $G^{-,-}(\mathbf{x}_0'', \mathbf{x}_i', t)$ contain a monopole signature. In order to have a redatumed reflection response $R(\mathbf{x}_i, \mathbf{x}_i', t)$ as if there is a dipole source at \mathbf{x}_i' , a monopole-to-dipole conversion has to be applied, see [Appendix B](#). The multidimensional deconvolution (MDD) is carried out using the MDD program developed by [Thorbecke \(2017\)](#). The results obtained by deconvolution are stabilized before estimating the angle-dependent reflectivity, see [Appendix C](#). The programs use the data format from Seismic Unix (SU) and some additional operations are performed using this software suite ([Cohen and Stockwell, 2016](#)). The spectral division, mapping process, and imaging condition are implemented using Matlab scripts developed by the author. These scripts can be found in [section E-2](#).

4-1 Imaging reflectivity in the presence of a complex overburden

A horizontally layered model of four layers is considered with a constant velocity of 1500 m/s and varying density, see [Figure 4-3](#). The second layer is characterized by a high-impedance contrast at the top and bottom, which is an approximation of a complex overburden. Out of the total modeled data set, three shot records are plotted in [Figure 4-4](#). Because the velocity is constant, the head wave does not exist. The direct arrivals are estimated from truncated media based on the models in [Figure 4-3](#). This means that the modeled direct arrivals are accurate in terms of arrival times and amplitudes. For the sake of demonstration, the imaging process will be applied to the reflector depth. Out of the total modeled direct arrivals, nine shots are plotted in [Figure 4-5](#) with their corresponding truncated media. Bear in mind that these truncated media are reflection free below the focal level z_i .

The reflection data $R(\mathbf{x}_0'', \mathbf{x}_0, t)$ and time-reversed direct arrival $G_d(\mathbf{x}_0'', \mathbf{x}_i', -t)$ are used as input to initiate the Marchenko iterative scheme, as described by [Equation 2-29](#) and [Equation 2-30](#). For the first reflector, which is located at 400 m, the scheme converges immediately at $k = 0$. This is expected as $f_1^-(\mathbf{x}_0'', \mathbf{x}_i', t)$ does not exist due to the fact that there is no reflector above the focal level. In this case, the total focusing function is only composed of $f_1^+(\mathbf{x}_0'', \mathbf{x}_i', t)$ which is equivalent to $G_d(\mathbf{x}_0'', \mathbf{x}_i', -t)$, as shown in [Figure 4-6-I](#). For the second reflector, which is located at 700 m, the scheme converges at $k = 4$. In this case, $f_1^-(\mathbf{x}_0'', \mathbf{x}_i', t)$ is generated due to the presence of a reflector above the focal level. Because $f_1^-(\mathbf{x}_0'', \mathbf{x}_i', t)$ does not cross any interfaces as it propagates, it will not produce any spurious events. Consequently, the scattering coda M^+ does not exist, and thus $f_1^+(\mathbf{x}_0'', \mathbf{x}_i', t)$ will also be the same as $G_d(\mathbf{x}_0'', \mathbf{x}_i', -t)$. Here, the total focusing function is composed of $f_1^+(\mathbf{x}_0'', \mathbf{x}_i', t)$ and $f_1^-(\mathbf{x}_0'', \mathbf{x}_i', t)$, as shown in [Figure 4-6-II](#). For the third reflector, which is located at 1100 m, the scheme converges at $k = 10$. At this depth level, $f_1^+(\mathbf{x}_0'', \mathbf{x}_i', t)$ is no longer equivalent to $G_d(\mathbf{x}_i', \mathbf{x}_0'', -t)$ due to the generation of internal multiples as $f_1^-(\mathbf{x}_0'', \mathbf{x}_i', t)$ crosses the second reflector. In this case, $f_1^+(\mathbf{x}_0'', \mathbf{x}_i', t) = G_d(\mathbf{x}_0'', \mathbf{x}_i', -t) + M^+(\mathbf{x}_0'', \mathbf{x}_i', t)$, as shown in [Figure 4-6-III](#).

The Green's functions are estimated at the depth of each reflector using [Equation 2-21](#) and [Equation 2-22](#). Since the focusing function at the first reflector consists of $G_d(\mathbf{x}_0'', \mathbf{x}_i', -t)$ only, the Marchenko and standard redatuming will produce the same Green's functions, as shown in [Figure 4-7-I](#). However, for the deeper reflectors, the focusing function includes $f_1^+(\mathbf{x}_0'', \mathbf{x}_i', t)$ and $f_1^-(\mathbf{x}_0'', \mathbf{x}_i', t)$, and thus the Marchenko and standard redatuming will not produce the same Green's functions. At every iteration, the focusing functions are updated in terms of events and amplitudes. As a result, the Green's functions will be updated with the correct events and amplitudes, as shown in [Figure 4-7-II](#) and [Figure 4-7-III](#). Before applying the imaging process, the source signature of the Green's functions is converted into dipole. First, the imaging process is carried out based on the MDD (see [Equation 2-36](#)). Bear in mind that only the first arrivals of $G^{-,+}(\mathbf{x}_0'', \mathbf{x}_i', t)$ and $G^{-,-}(\mathbf{x}_0'', \mathbf{x}_i', t)$ are used in this process.

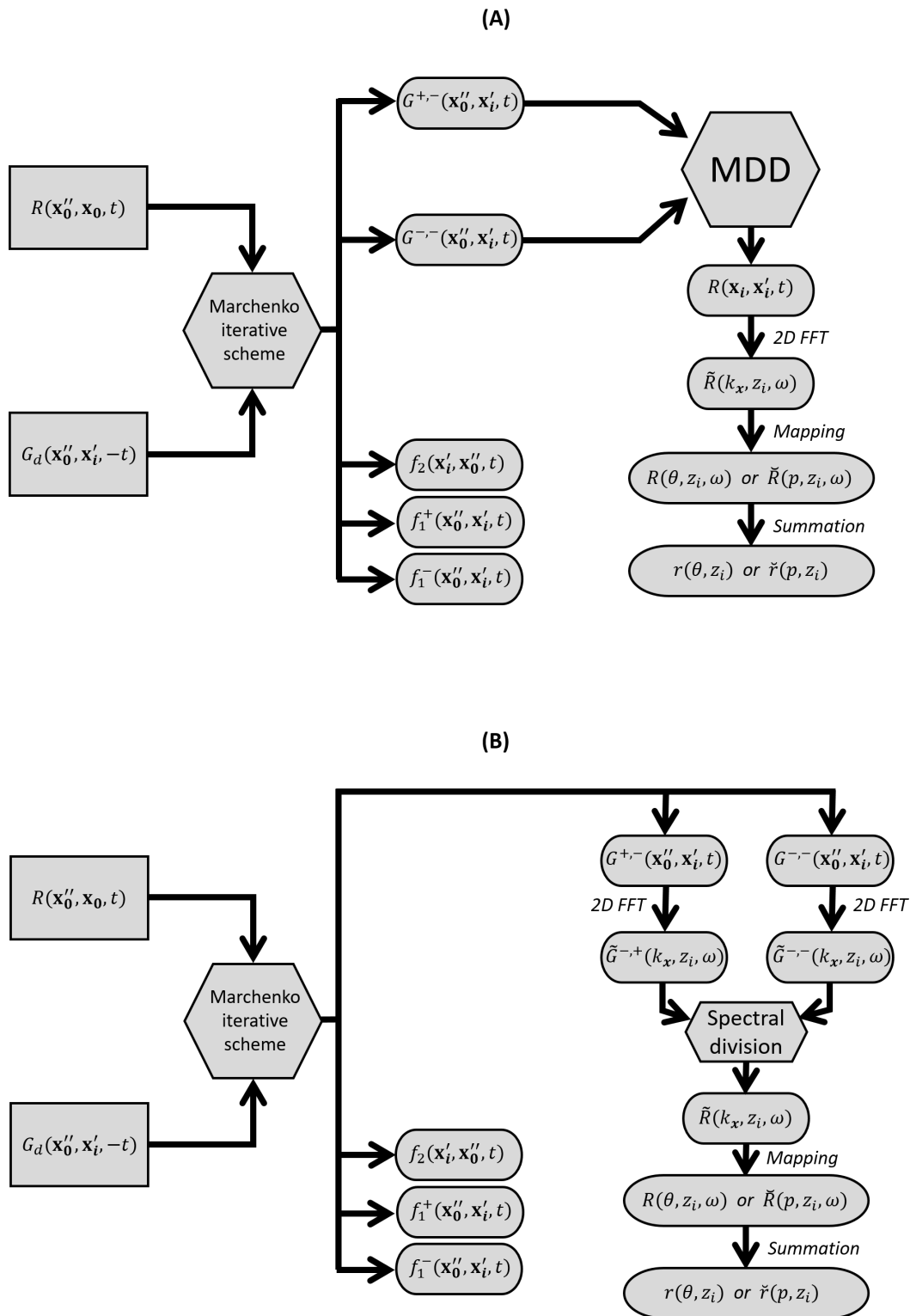


Figure 4-1: The workflow of imaging angle-dependent reflectivity using the Marchenko method. (A) Imaging based on the MDD. (B) Imaging based on the spectral division. Note that FFT stands for fast Fourier transform.

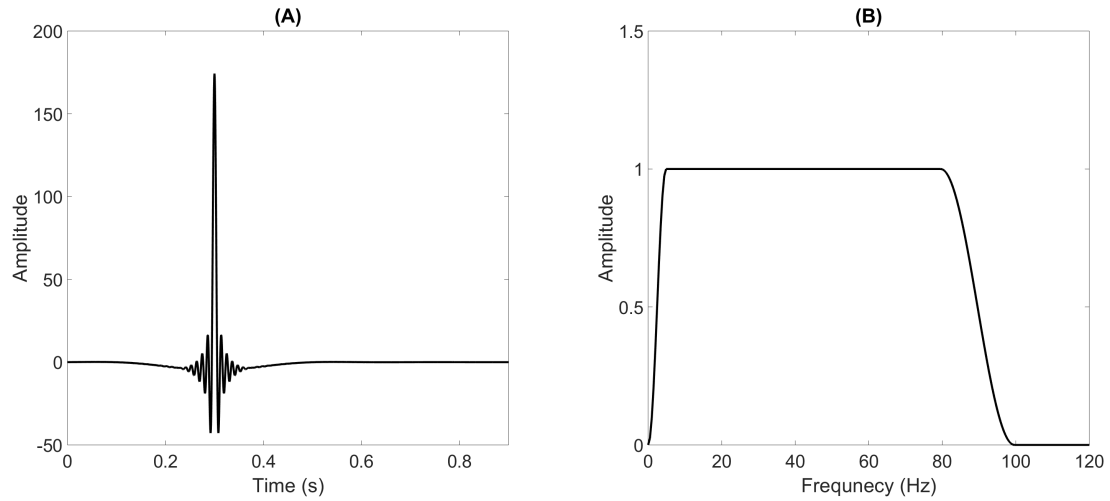


Figure 4-2: Source wavelet with a flat frequency spectrum between $f_{min} = 5$ Hz and $f_{max} = 80$ Hz. (A) Time domain. (B) Frequency domain.

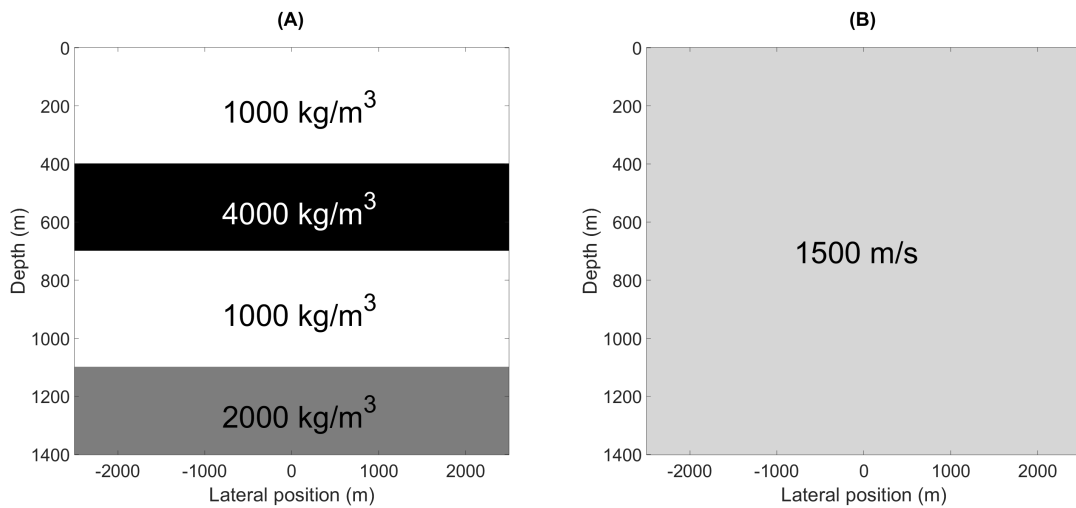


Figure 4-3: A Laterally invariant medium with a complex overburden. (A) Density model. (B) Velocity model. Note that the velocity is constant here.

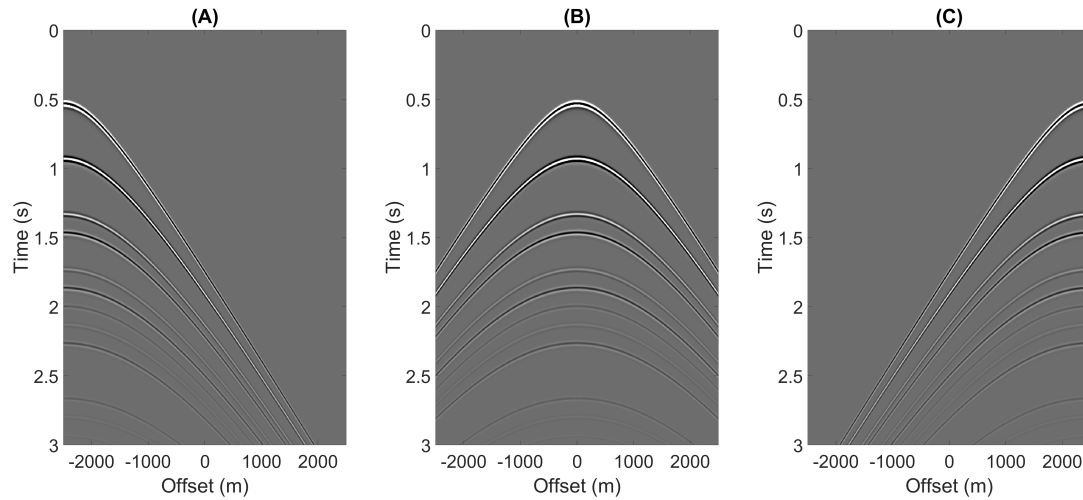


Figure 4-4: Modeled reflection data $R(\mathbf{x}''_0, \mathbf{x}_0, t)$ of the medium in Figure 4-3 with a source located at the surface and (A) $x = -2500$ m, (B) $x = 0$ m, and (C) $x = 2500$ m.

Therefore, the redatumed reflection response $R(\mathbf{x}_i, \mathbf{x}'_i, t)$ will consist of a single reflection event, as shown in Figure 4-8. Compared to standard redatuming, it can be seen that the AVO response, as shown in Figure 4-8C, is preserved by the Marchenko method. In addition, the Marchenko method produces a redatumed reflection response free of artefacts (see Figure 4-8III-A and III-B). Since the medium is laterally invariant, the redatumed reflection response with the virtual source located at $\mathbf{x}'_i = (x = 0, z_i)$ is sufficient for estimating the angle-dependent reflectivity. The mapping process is applied on $R(\mathbf{x}_i, \mathbf{x}'_i, t)$ (see Equation 3-11 and Equation 3-12) to obtain the $p - \omega$ and $\theta - \omega$ spectra, as shown in Figure 4-9. Finally, the angle-dependent reflectivity is estimated in the ray parameter and angle domains using Equation 3-15 and Equation 3-16, as shown in Figure 4-10. Unlike the standard imaging, it can be seen that the Marchenko method successfully recovered the angle-dependent reflectivity. It is important to mention that the reflectivity is only recovered when the scheme has converged, as shown in Figure 4-11. The imaging process can be repeated for every \mathbf{x}'_i . However, the Green's function $G^{-,+}(\mathbf{x}''_0, \mathbf{x}'_i, t)$ with \mathbf{x}'_i located at the far offset is not completely retrieved due to the existence of stationary points, see Figure 4-12. As a result, the redatumed response $R(\mathbf{x}_i, \mathbf{x}'_i, t)$ will not be reconstructed completely.

Next, the imaging process is carried out based on the spectral division (see Equation 2-38) since the medium is laterally invariant. The Green's functions with the virtual source located at $\mathbf{x}'_i = (x = 0, z_i)$ are sufficient for estimating the angle-dependent reflectivity. After applying spectral division, the result is mapped into the ray parameter and angle domains, as shown in Figure 4-13. Finally, the angle-dependent reflectivity is obtained using Equation 3-15 and Equation 3-16, as shown in Figure 4-14. Compared to the MDD, the spectral division covers a wider range of offset. This is because the Green's function $G^{-,-}(\mathbf{x}''_0, \mathbf{x}'_i, t)$ is not retrieved completely at the far offset due to the effect of the mute window Θ . At the far offset, the window starts intersecting $G^{-,-}(\mathbf{x}''_0, \mathbf{x}'_i, t)$, causing partial removal of the function, as shown in Figure 4-15. Because the MDD approach uses all the $G^{-,-}(\mathbf{x}''_0, \mathbf{x}'_i, t)$, instead of only the center one, the lack of the far offset retrieval affects the offset at which the reflectivity can be obtained.

By repeating the imaging process for all depth levels, the image of the angle-dependent reflectivity can be reconstructed. For faster computation, the process is applied based on the spectral division with a

depth step of 5 m. The images of the real and imaginary parts of the reflectivity are shown in [Figure 4-16](#) and [Figure 4-17](#), respectively. Note that the real part indicates the polarity of the reflectivity. By using the real and imaginary parts, the modulus can be estimated, as shown in [Figure 4-18](#). Because the source wavelet has a finite length (see [Figure 4-2](#)), there is energy away from the interface in the image domain, reflecting the band-limitation in this imaging process. Note that at oblique angles in the $z - \theta$ gather, the width of the imaged event increases for increasing θ value. This can be explained by the apparent wavelength along the z -direction $\lambda_z = \lambda / \cos \theta$, with λ as wavelength along the propagation direction. Under oblique angles, the denominator becomes smaller (i.e. $\cos \theta \rightarrow 0$ for $\theta \rightarrow 90^\circ$). Consequently, the apparent length λ_z increases, reflecting the loss of resolution at the far offset. By amplitude picking along the events in [Figure 4-18](#) and taking the polarity from the events in [Figure 4-16](#), the angle-dependent reflection coefficients are obtained ([Figure 4-14A](#)). A similar process can be applied to obtain the image in the ray parameter domain.

4-2 Imaging reflectivity in a medium with varying velocity and density

In the previous example, the reflectivity was constant for all angles because there were only density contrasts in the medium. In reality, however, the velocity of the subsurface is inhomogeneous. When there are velocity contrasts, head waves are generated at the critical angle θ_c (see [Equation 3-3](#)) and evanescent waves are generated at angles larger than θ_c . The Marchenko method cannot deal with these types of waves ([Wapenaar et al., 2014b](#)). In this example, the approach is evaluated for retrieving the reflectivity when both density and velocity vary with depth, as shown in [Figure 4-19](#). Out of the total data set, three shot records are plotted in [Figure 4-20](#). The direct arrivals are estimated from truncated media extracted from the same model in [Figure 4-19](#).

Similar to the previous example, the imaging process is applied at the depth of each reflector. The reflection data and time-reversed direct arrivals are used as input in the Marchenko scheme to obtain the focusing and Green's functions, which are shown in [Figure 4-21](#). First, the redatumed reflection response is estimated using the MDD and then mapped into the angle and ray parameter domains, see [Figure 4-22](#). Note that when the velocity varies across an interface, the spectrum is no longer flat (see [Figure 4-22I](#) and [Figure 4-22III](#)). Only the second reflector ([Figure 4-22II](#)) shows a flat spectrum because the velocity does not change across it. The frequency contributions are summed along lines of constant angle and ray parameter to obtain the angle-dependent reflectivity, as shown in [Figure 4-23](#). For the first reflector, it can be seen that both the Marchenko and standard methods recover the angle-dependent reflectivity up to the critical angle. For the second reflector, where only the density varies, the Marchenko method estimates the reflectivity correctly, unlike the standard method which shows lower amplitude and artefacts. This shows that the Marchenko method is not affected by the velocity contrasts surrounding this reflector. For the third reflector, the reflectivity estimated by the Marchenko method is retrieved correctly below the critical angle. This is due to the effect of the wave propagation through the subsurface, especially in a medium with a varying velocity. As the wave propagates into the subsurface, it refracts according to Snell's law (see [Figure 3-1](#)). As a result, the wave starts bending while propagating and when it reflects from the deep reflector it arrives outside the acquisition surface. In order to obtain such events, a larger aperture is required. This introduces a practical limitation to surface seismic acquisition.

Next, the redatumed reflection response is estimated using the spectral division and mapped into the ray parameter and angle domains, see [Figure 4-24](#). The angle-dependent reflectivity is then estimated, as shown in [Figure 4-25](#). Compared to the MDD, the spectral division covers a wider range of angles.

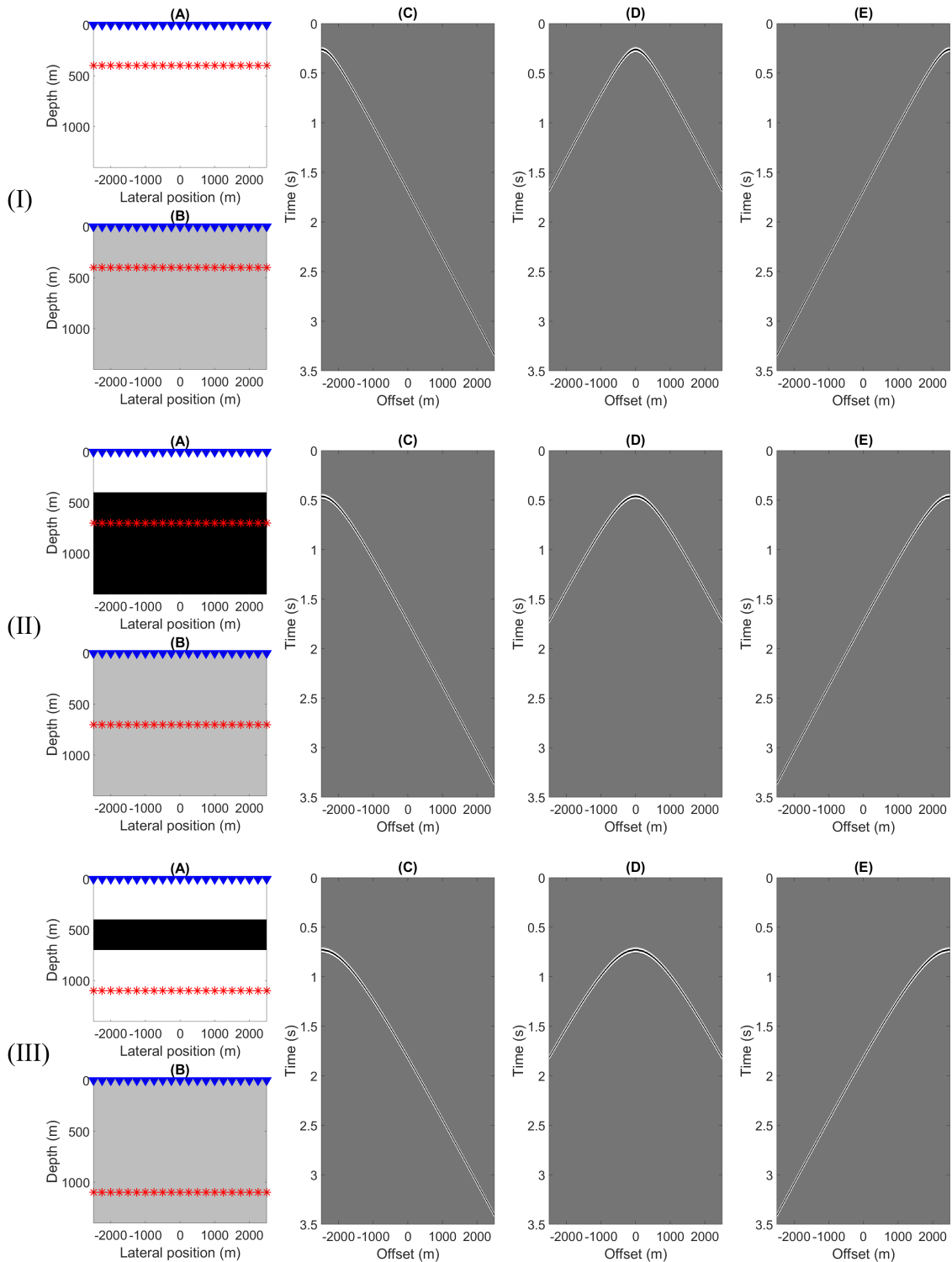


Figure 4-5: Modeled direct arrivals $G_d(\mathbf{x}''_0, \mathbf{x}'_i, t)$ from (I) $z_i = 400$ m, (II) $z_i = 700$ m, and (III) $z_i = 1100$ m. The (A) density model and (B) velocity model are extracted from the models in Figure 4-3. The red asterisks and blue triangles indicate the locations of the sources and receivers, respectively. Note that the truncated velocity media are the same as the actual medium because the velocity is homogeneous in this example. (C) Source located at $x = -2500$ m. (D) Source located at $x = 0$, (E) Source located at $x = 2500$ m.

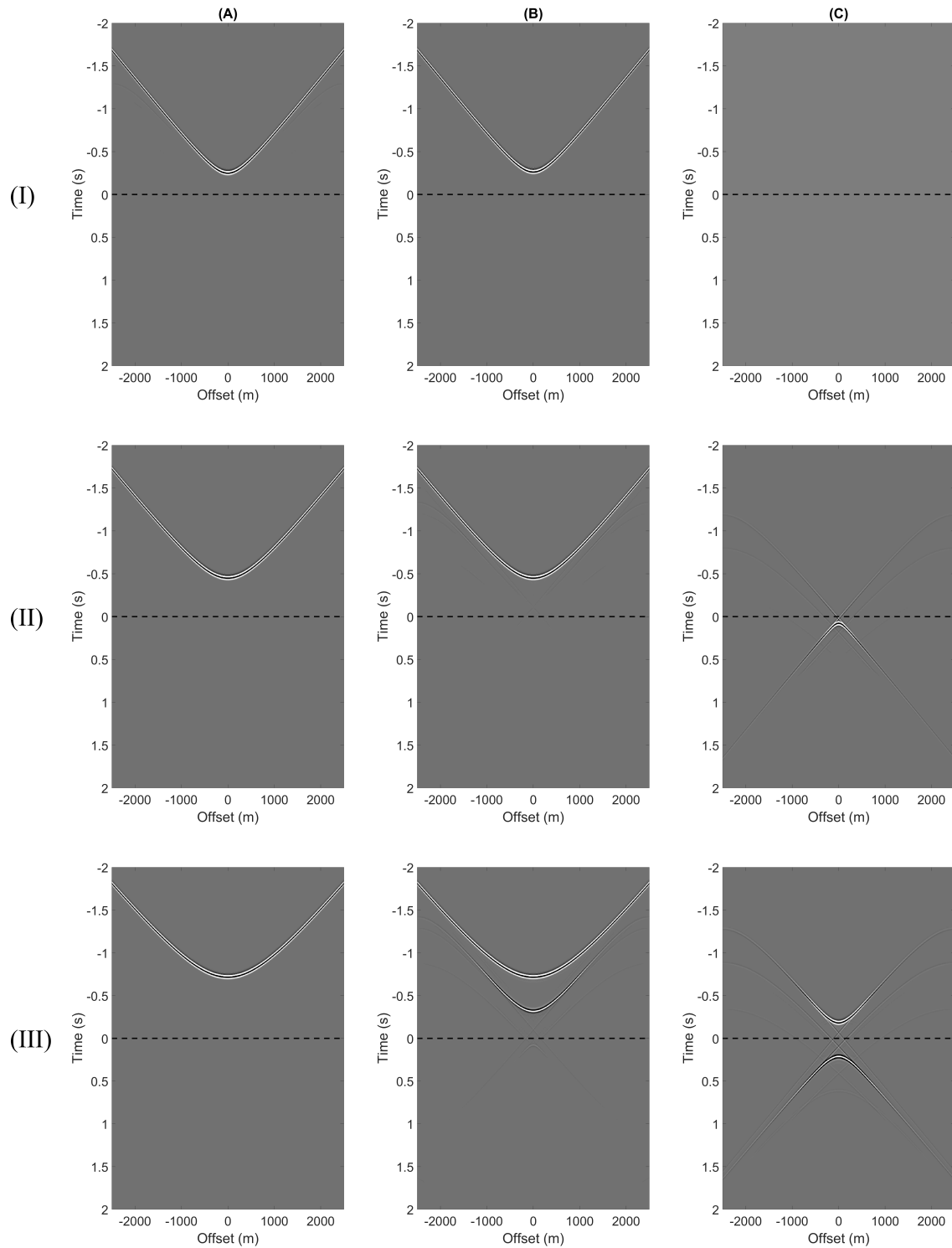


Figure 4-6: Focusing functions estimated in a medium with a complex overburden. The focal point is located at $x = 0$ and (I) $z_i = 400$ m, (II) $z_i = 700$ m, and (III) $z_i = 1100$ m. (A) $G_d(\mathbf{x}_0'', \mathbf{x}_i', -t)$. (B) $f_1^+(\mathbf{x}_0'', \mathbf{x}_i', t)$. (C) $f_1^-(\mathbf{x}_0'', \mathbf{x}_i', t)$. The horizontal dashed line indicates $t = 0$. Note that $f_1^+(\mathbf{x}_0'', \mathbf{x}_i', t)$ in (III-B) consists of two events which correspond to G_d and M^+ .

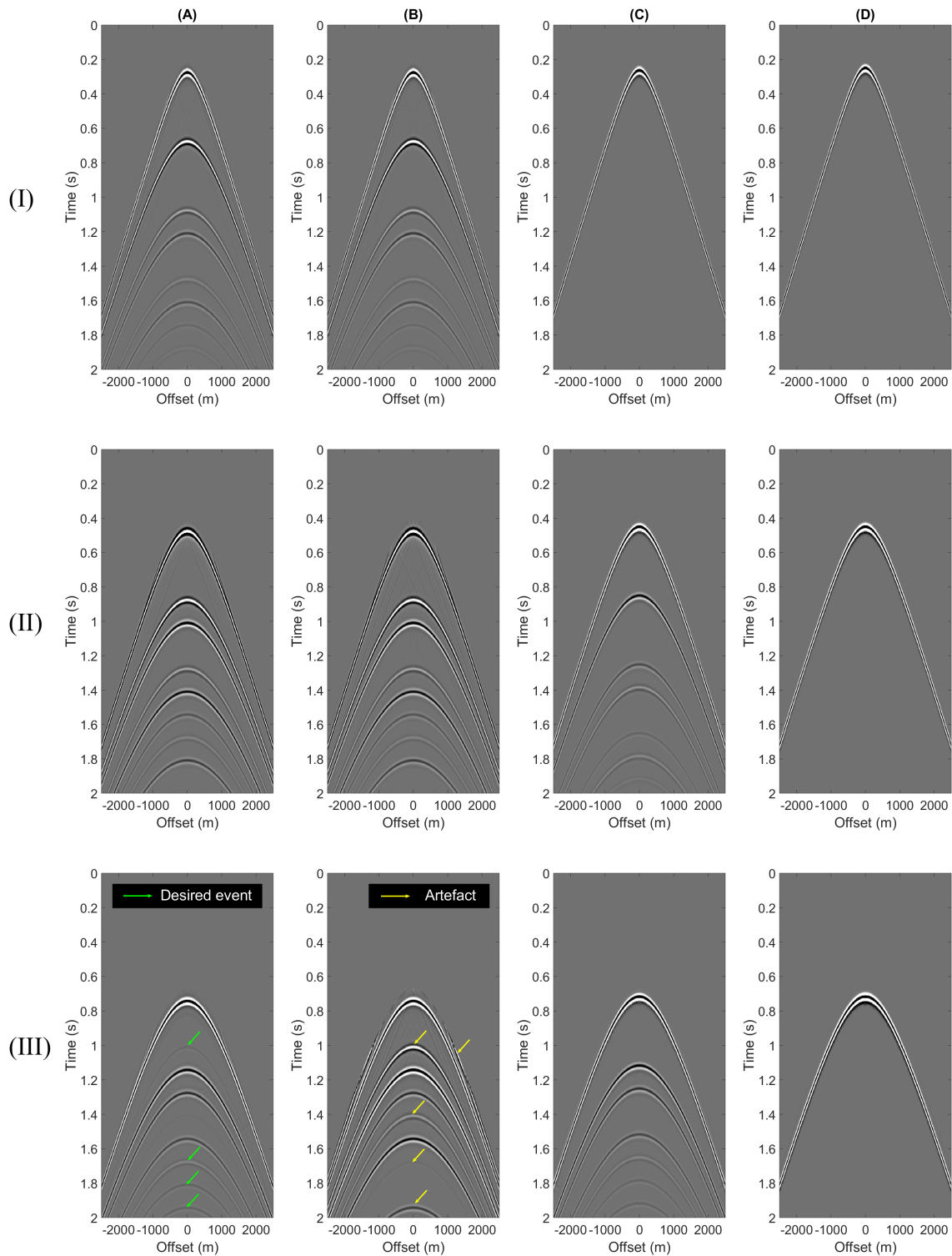


Figure 4-7: Comparison between the Marchenko and standard methods in estimating the Green's functions with a complex overburden. The focal point is located at $x = 0$ and (I) $z_i = 400$ m, (II) $z_i = 700$ m, and (III) $z_i = 1100$ m. (A) Marchenko $G^{-,+}$. (B) Standard $G^{-,+}$. (C) Marchenko $G^{-,-}$. (D) Standard $G^{-,-}$. Note the desired events obtained by the Marchenko method and the artefacts existing in the standard method. For deeper reflectors, the Marchenko method retrieves more than one event in $G^{-,-}$.

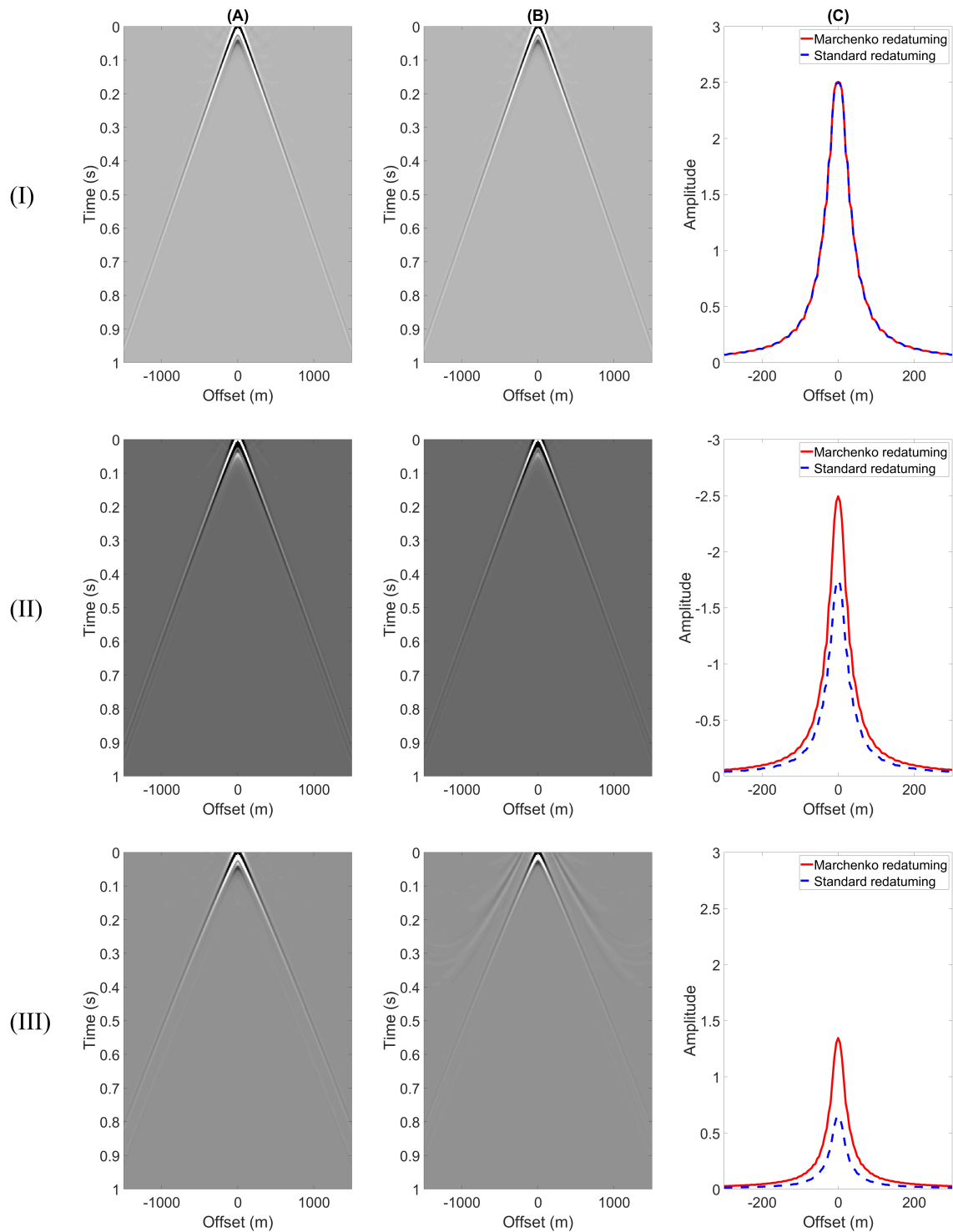


Figure 4-8: The redatumed reflection response $R(\mathbf{x}_i, \mathbf{x}'_i, t)$ in the presence of a complex overburden. The virtual source is located at $x = 0$ and (I) $z_i = 400$ m, (II) $z_i = 700$ m, and (III) $z_i = 1100$ m. (A) Marchenko redatuming. (B) Standard redatuming. (C) AVO response obtained by estimating the envelope from (A) and (B).

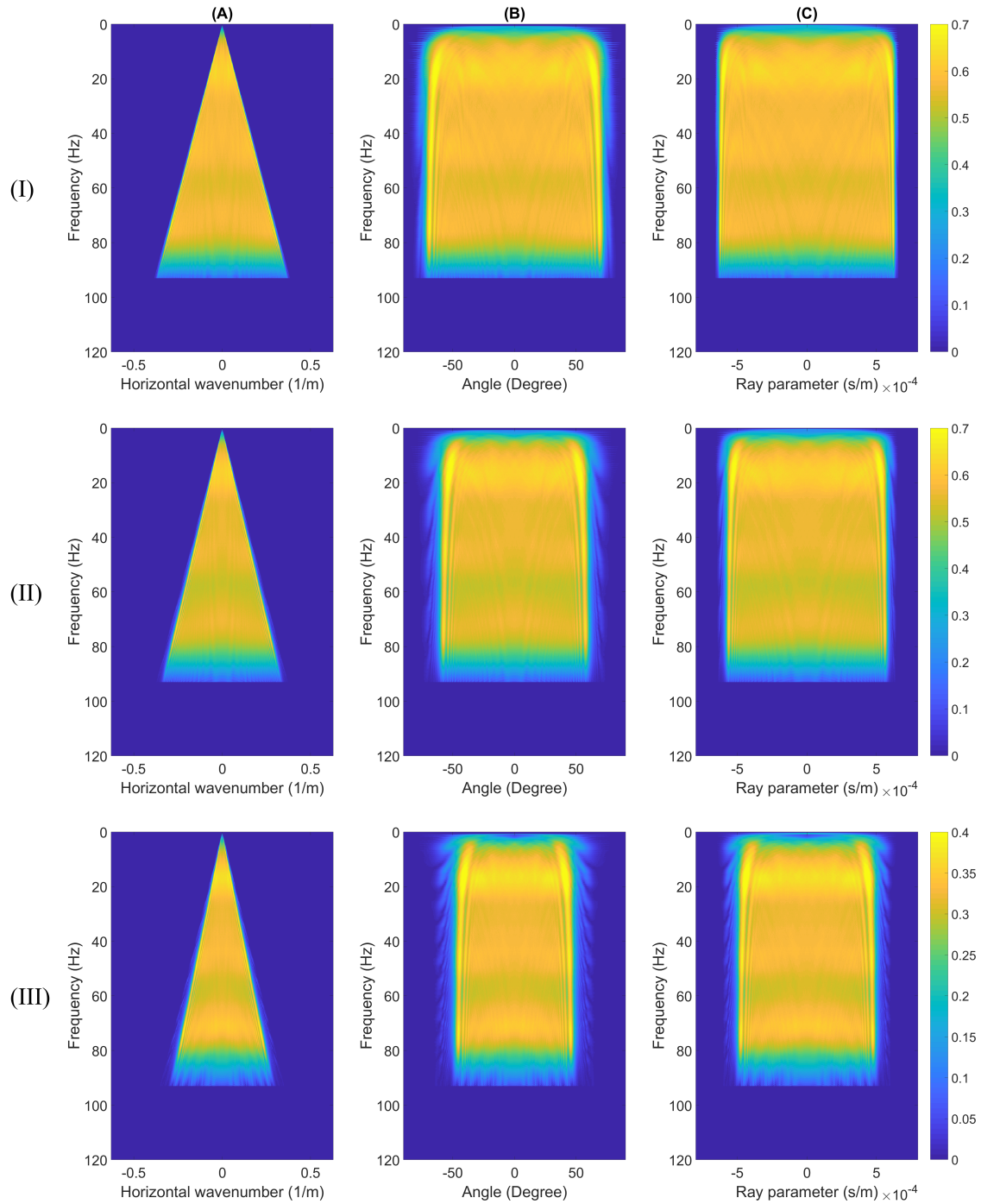


Figure 4-9: Applying the mapping process on $R(\mathbf{x}_i, \mathbf{x}'_i, t)$ which is estimated in a medium with a complex overburden. The focal point is located at $x = 0$ and (I) $z_i = 400$ m, (II) $z_i = 700$ m, and (III) $z_i = 1100$ m. (A) Wavenumber-frequency domain. (B) Angle-frequency domain. (C) Ray parameter-frequency domain. Only the moduli have been plotted.

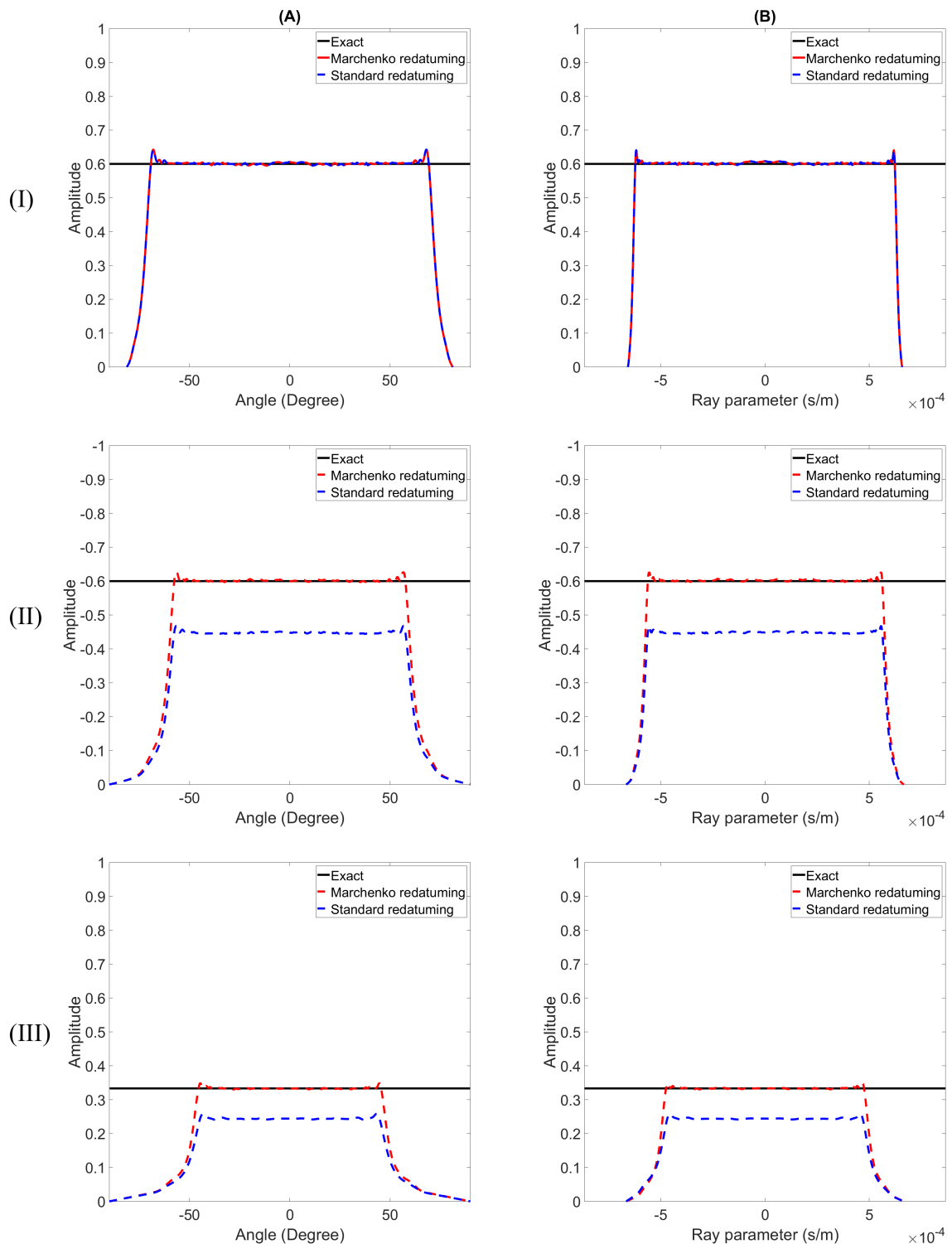


Figure 4-10: The angle-dependent reflectivity obtained by the Marchenko and standard redatuming methods in a medium containing a complex overburden. (I) $z_i = 400$ m. (II) $z_i = 700$ m. (III) $z_i = 1100$ m. (A) Reflectivity as a function of angle. (B) Reflectivity as a function of ray parameter.

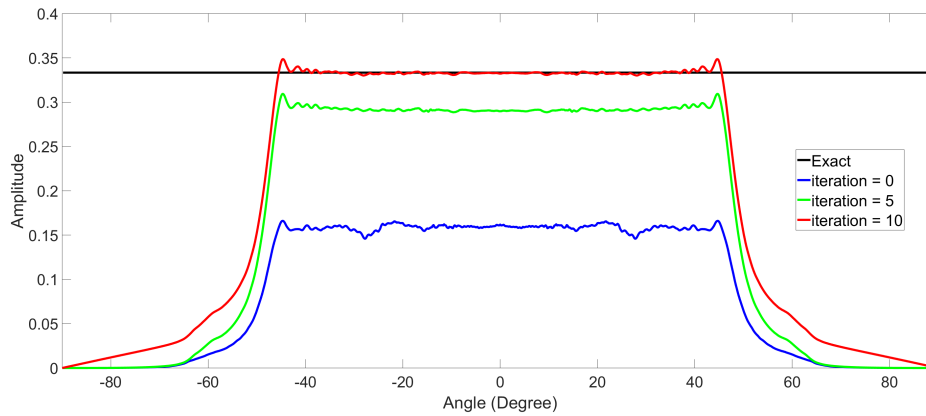


Figure 4-11: The angle-dependent reflectivity at $z_i = 1100$ with different iteration numbers. Note that the reflectivity is correctly retrieved at $k = 10$, which represents the maximum iteration number at this depth level.

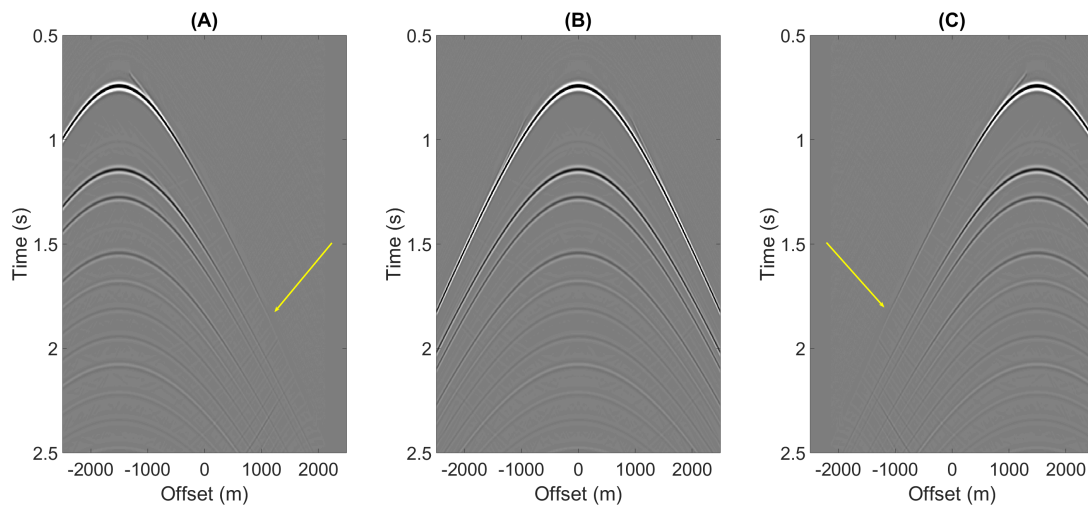


Figure 4-12: Estimated $G^{-,+}$ in a medium with a complex overburden. (A) $\mathbf{x}'_i = (-1500 \text{ m}, 1100 \text{ m})$. (B) $\mathbf{x}'_i = (0, 1100 \text{ m})$. (C) $\mathbf{x}'_i = (1500 \text{ m}, 1100 \text{ m})$. Note that $G^{-,+}$ is completely retrieved in (B), while it is not in (A) and (C) due the stationary points. The yellow arrows indicate the missing parts.

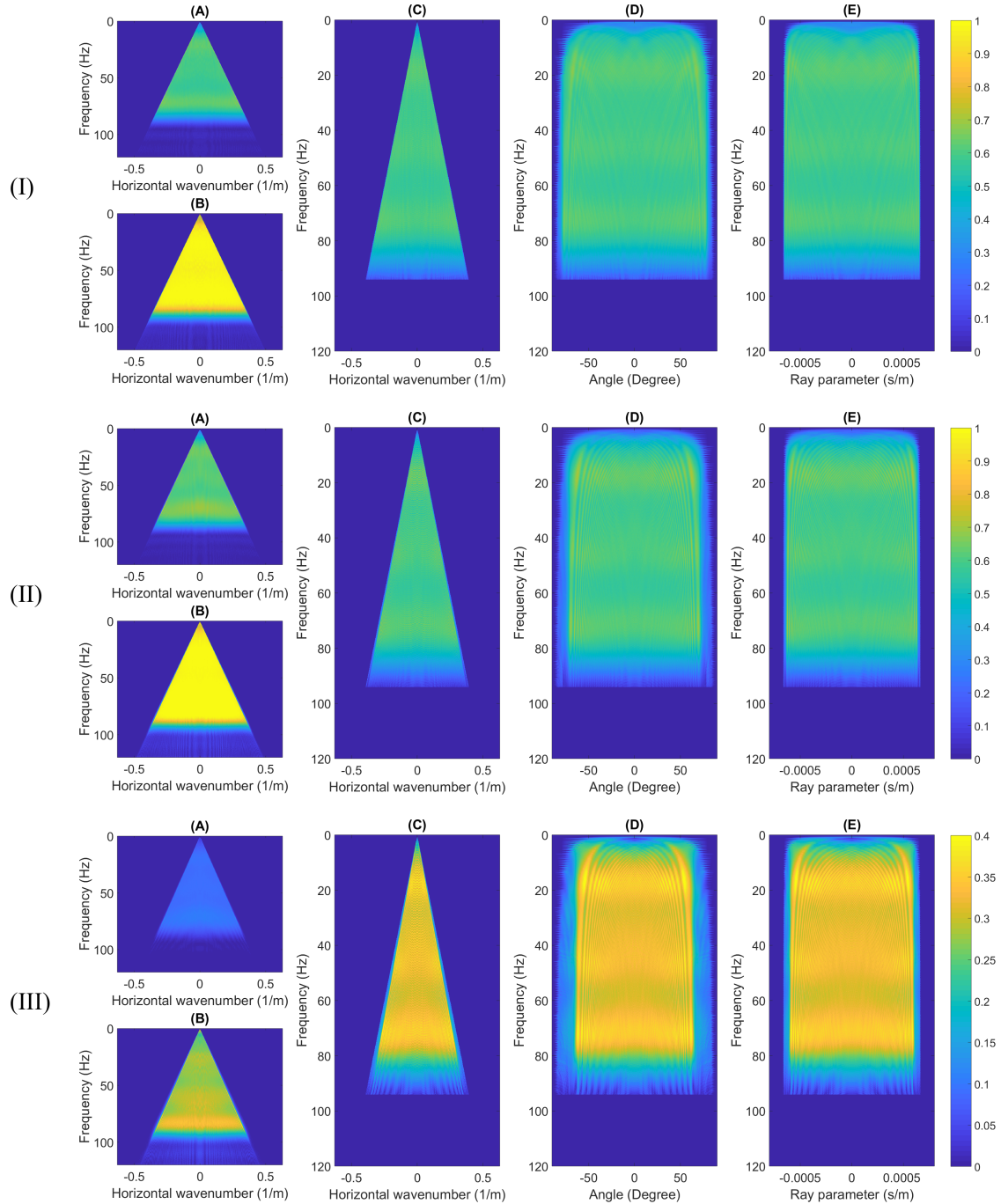


Figure 4-13: Applying the mapping process on $G^{-,+}$ and $G^{-,-}$ which are estimated in a medium with a complex overburden. The focal point is located at $x = 0$ and (I) $z_i = 400$ m, (II) $z_i = 700$ m, and (III) $z_i = 1100$ m. (A) First arrival of $\tilde{G}^{-,+}(k_x, z_i, \omega)$. (B) First arrival of $\tilde{G}^{-,-}(k_x, z_i, \omega)$. (C) Spectral division. (D) Angle-frequency domain. (E) Ray parameter-frequency domain. Only the moduli have been plotted.

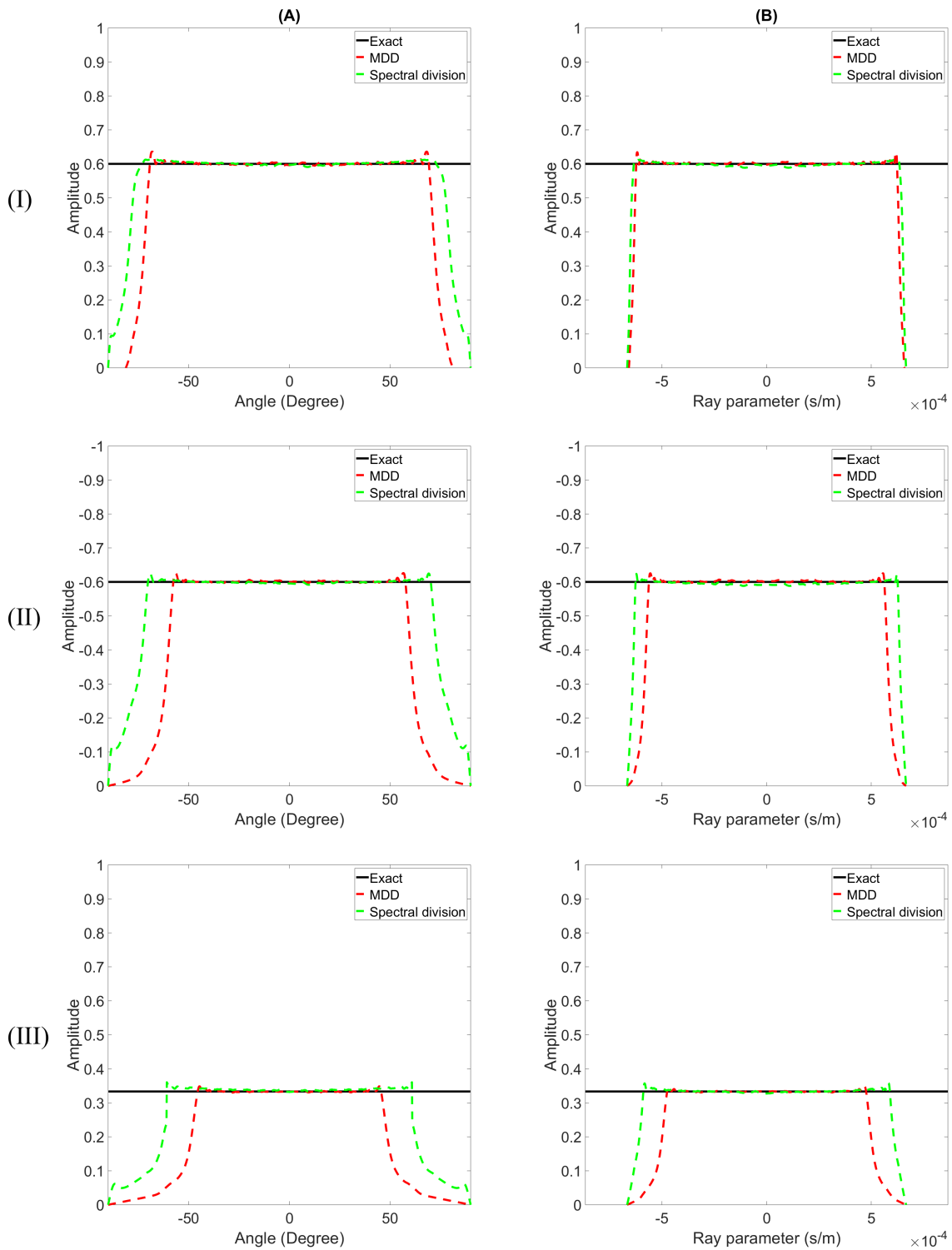


Figure 4-14: The angle-dependent reflectivity obtained by the spectral division and MDD in a medium containing a complex overburden. (I) $z_i = 400$ m. (II) $z_i = 700$ m. (III) $z_i = 1100$ m. (A) Reflectivity as a function of angle. (B) Reflectivity as a function of ray parameter.

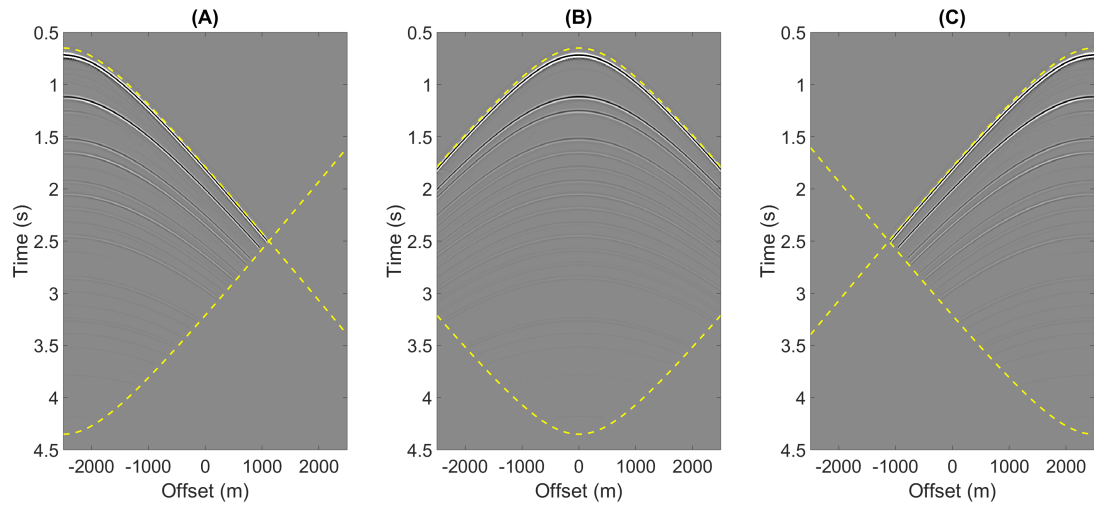


Figure 4-15: The effect of the mute window Θ (yellow dashed hyperbola) on the retrieval of $G^{-,-}(\mathbf{x}_0'', \mathbf{x}_i', t)$. (A) $\mathbf{x}_i' = (-2500 \text{ m}, 1100 \text{ m})$. (B) $\mathbf{x}_i' = (0, 1100 \text{ m})$. (C) $\mathbf{x}_i' = (2500 \text{ m}, 1100 \text{ m})$.

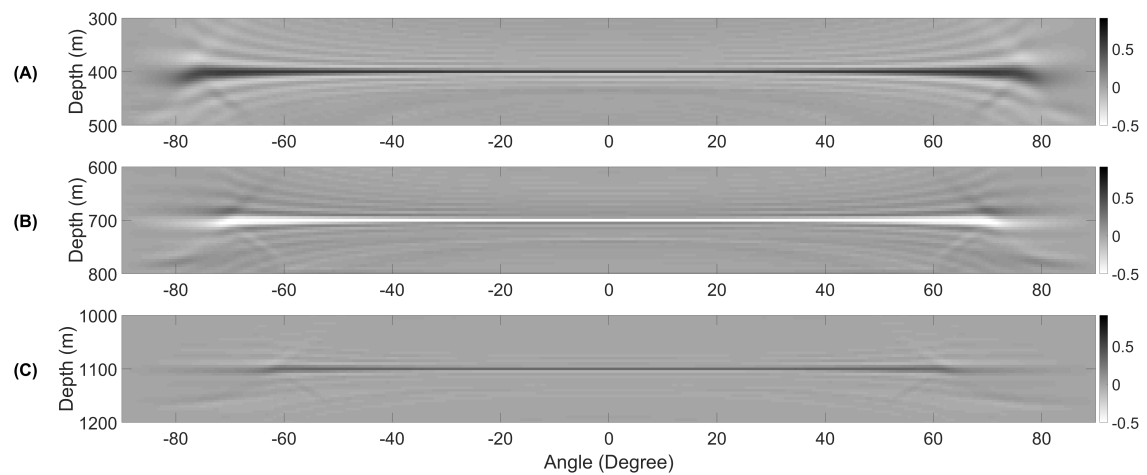


Figure 4-16: Real part of the angle-dependent reflectivity as a function of depth with the presence of a complex overburden. (A) First reflector. (B) Second reflector. (C) Third reflector. Note that the real part shows the polarity of the reflectivity, with white as a negative polarity and black as a positive polarity.

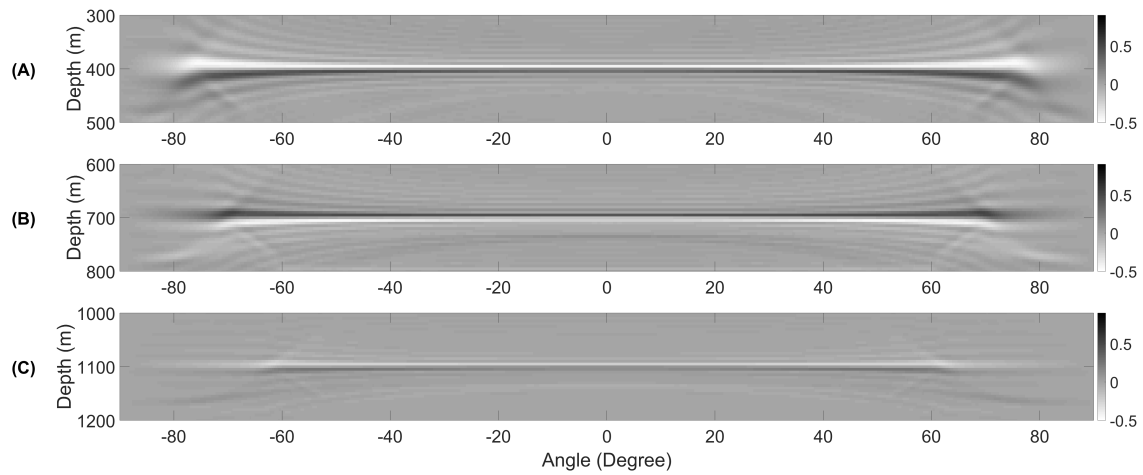


Figure 4-17: Imaginary part of the angle-dependent reflectivity as a function of depth with the presence of a complex overburden. (A) First reflector. (B) Second reflector. (C) Third reflector.

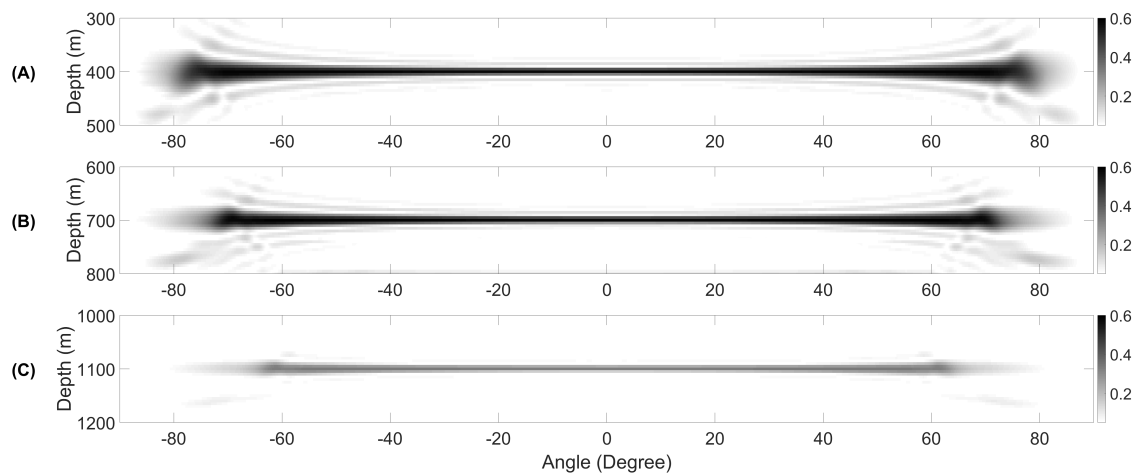


Figure 4-18: Modulus of the angle-dependent reflectivity as a function of depth with the presence of a complex overburden. (A) First reflector. (B) Second reflector. (C) Third reflector. Note that the first and second reflectors show very high contrasts associated with the complex overburden.

This is due to the effect of the mute window Θ on $G^{-, -}$, as explained in the previous example. It is important to mention that because of the varying velocity, the direct arrival G_d bends as it propagates from deeper reflectors. Consequently, the mute window is also affected by the wave propagation.

By repeating the process for all depth levels, the image of the angle-dependent reflectivity can be reconstructed. For faster computation, the process is applied based on the spectral division with a depth step of 5 m. The images of the real and imaginary parts of the reflectivity are shown in Figure 4-26 and Figure 4-27, respectively. By using the real and imaginary parts, the modulus can be estimated as shown in Figure 4-28. By amplitude picking along the events in Figure 4-28 and taking the polarity from the events in Figure 4-26, the angle-dependent reflection coefficient is obtained (Figure 4-14A).

Based on the results of this example and the previous one, it can be concluded that the Marchenko method has the potential to retrieve angle-dependent reflectivity correctly, unlike the standard method. In the next examples, only the approach using the Marchenko method will be considered.

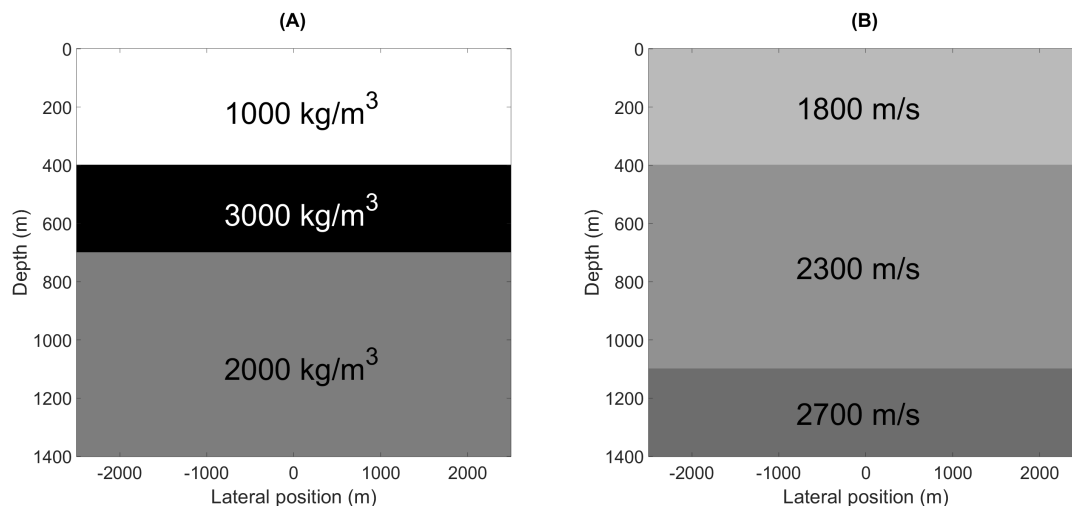


Figure 4-19: A Laterally invariant medium with varying density and velocity. (A) Density model. (B) Velocity model.

4-3 Imaging reflectivity in the presence of a low-velocity layer.

Following a similar example as De Bruin et al. (1990), a horizontally layered model is considered with a low-velocity layer located between 500 m and 1400 m, as shown in Figure 4-29. At this layer, the critical angle does not exist as described by Equation 3-1. For the purpose of this example, the imaging process is only applied on the depth of the low-velocity layer. The angle-dependent reflectivity at this layer is depicted in Figure 4-30. It can be seen that the approach successfully obtained the reflectivity using the Marchenko method. By repeating the imaging process around this layer, the image of the angle-dependent reflectivity can be reconstructed. For faster computation, the process is applied based on the spectral division with a depth step of 5 m, see Figure 4-31

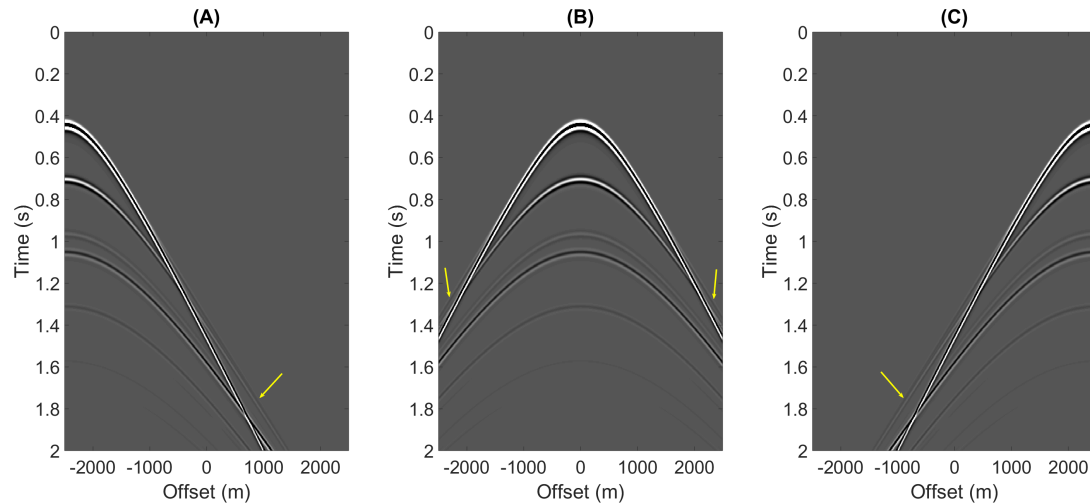


Figure 4-20: Modeled reflection data $R(\mathbf{x}''_0, \mathbf{x}_0, t)$ of the medium in Figure 4-19 with a source located at the surface and (A) $x = -2500$ m, (B) $x = 0$ m, and (C) $x = 2500$ m. The yellow arrows highlight the head waves, observed from around $t = 1$ s and $x = \pm 850$ m.

4-4 Imaging reflectivity using an inaccurate density model

In section 4-1, the density model from which the direct arrivals have been estimated was assumed to be correct. In practice, however, the density model can be inaccurate. In this example, the reflection response is modeled based on the models in Figure 4-32, whereas the direct arrivals are estimated based on the models in Figure 4-33. The density model shows an absolute error of 500 kg/m^3 in each layer. This will introduce an error in the amplitudes of the direct arrivals, as shown in Figure 4-34. Thus, the amplitudes of the focusing and Green's functions will also contain errors. However, by applying the imaging process at the depth of each reflector, the reflectivity is obtained correctly, as shown in Figure 4-35. This is because the deconvolution process compensates for the amplitude errors in $G^{-,+}(\mathbf{x}''_0, \mathbf{x}'_i, t)$ and $G^{-,-}(\mathbf{x}''_0, \mathbf{x}'_i, t)$ as long as they contain the same error.

4-5 Imaging reflectivity using an inaccurate velocity model

In section 4-2, the velocity model from which the direct arrivals have been estimated was assumed to be correct. In practice, however, the velocity model often contains errors. Here, the example in section 4-2 is repeated, but now the direct arrivals are estimated from truncated media based on the models in Figure 4-36. The velocity model shows an error of $+100 \text{ m/s}$ in each layer (about $+5.5$ percent in each layer). This will introduce errors in the amplitudes and travel times of the direct arrivals, which are shown in Figure 4-37. In the previous example, it was established that an error in the amplitude of the direct arrival does not have any consequences on the method because the error is canceled by the deconvolution process. However, the arrival time of the direct arrival has a significant influence in the Marchenko scheme. The window operator, which separates the focusing and Green's functions from each other, is defined by the travel time of the direct arrival. An error in the travel time of the direct arrival will introduce an erroneous time shift and residual moveout in the estimated Green's functions, thus introducing the same impact on the redatumed reflection response.

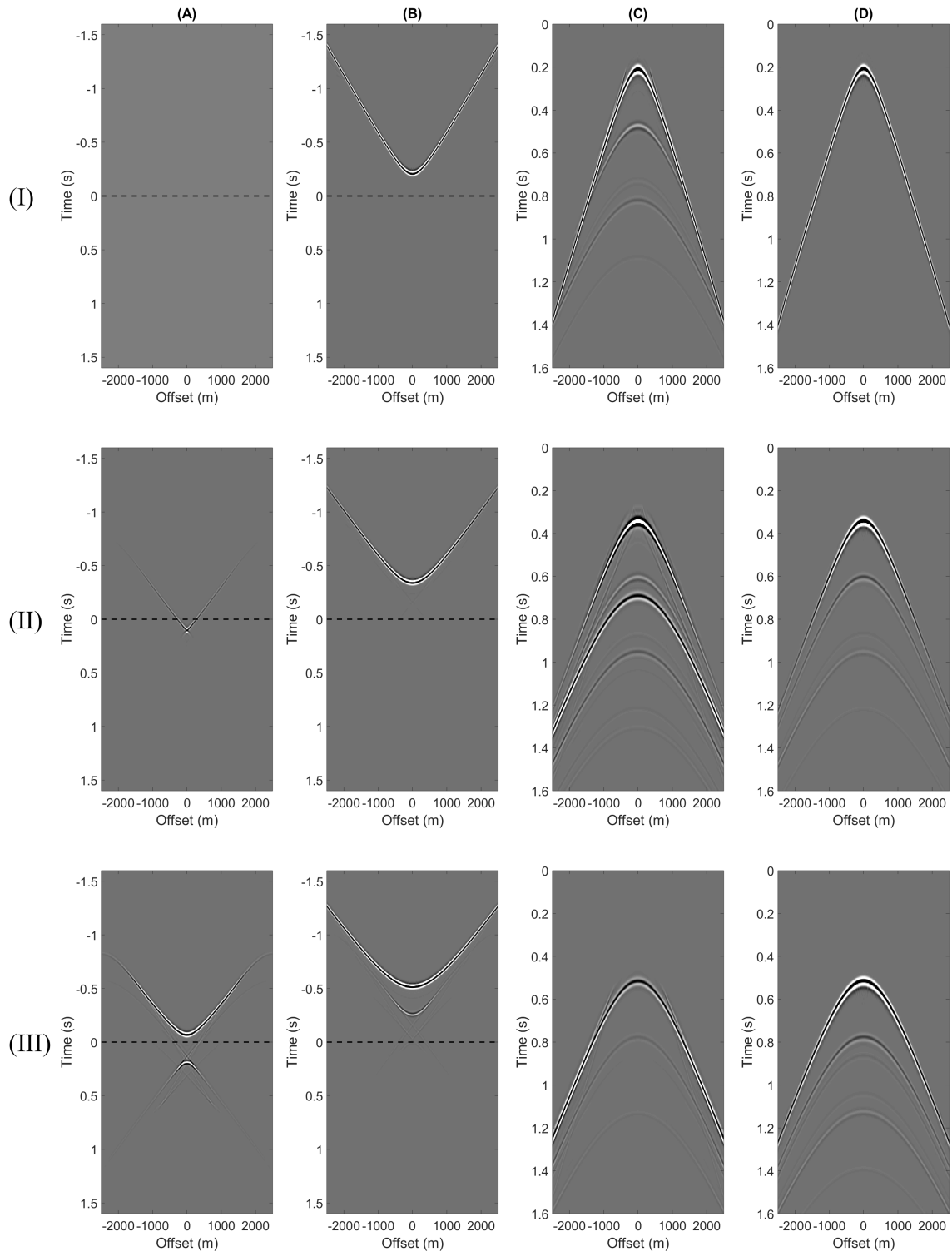


Figure 4-21: Estimated Green's and focusing functions in a medium with varying density and velocity. The focal point is located at $x = 0$ and (I) $z_i = 400$ m, (II) $z_i = 700$ m, and (III) $z_i = 1100$ m. (A) $f_1^-(\mathbf{x}_0'', \mathbf{x}_i', t)$. (B) $f_1^+(\mathbf{x}_0'', \mathbf{x}_i', t)$. (C) $G^{-,+}(\mathbf{x}_0'', \mathbf{x}_i', t)$. (D) $G^{-,-}(\mathbf{x}_0'', \mathbf{x}_i', t)$. The horizontal dashed line indicates $t = 0$.

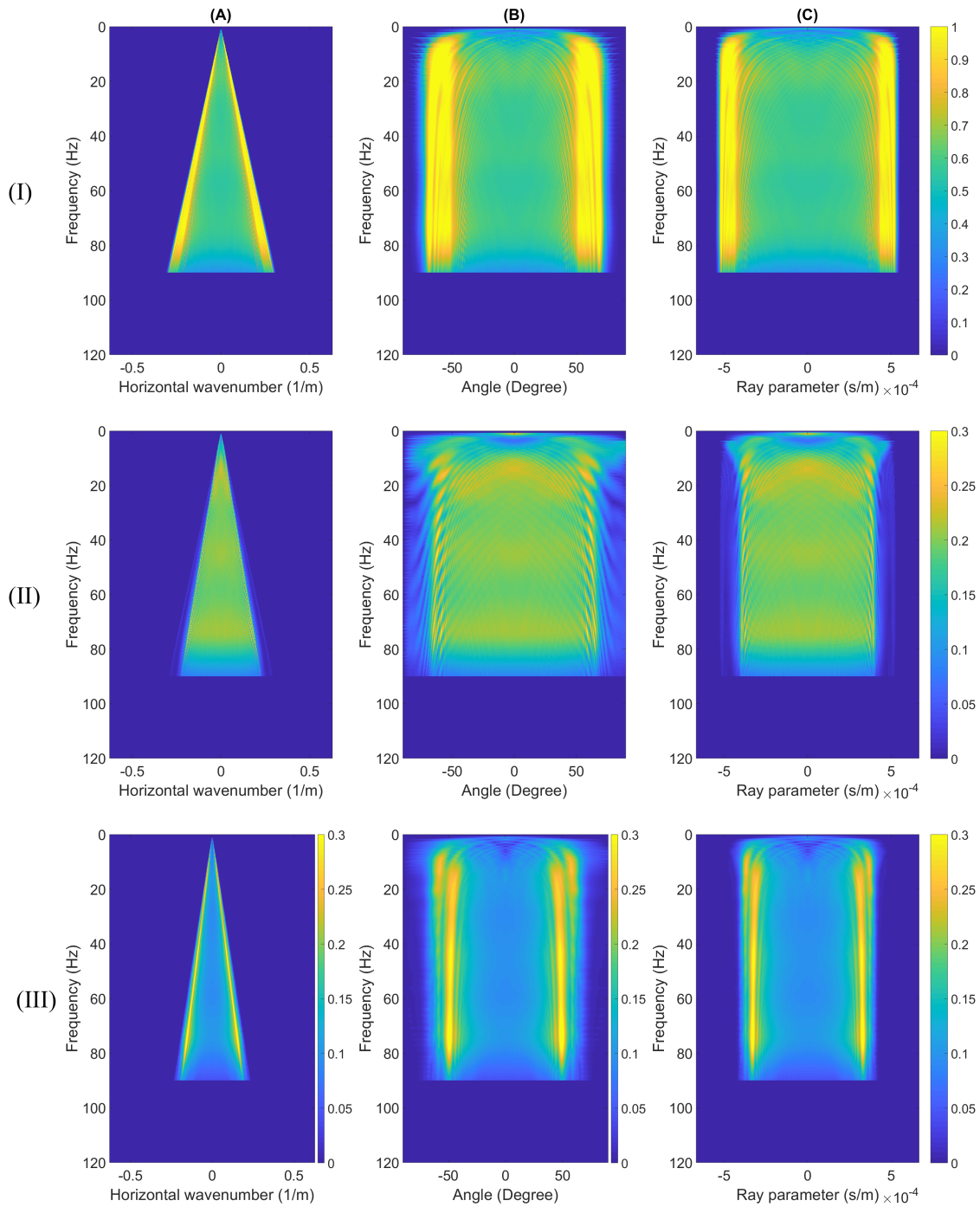


Figure 4-22: Applying the mapping process on $R(\mathbf{x}_i, \mathbf{x}'_i, t)$ which is estimated in a medium with varying density and velocity. The focal point is located at $x = 0$ and (II) $z_i = 700$ m, and (III) $z_i = 1100$ m. (A) Wavenumber-frequency domain. (B) Angle-frequency domain. (C) Ray parameter-frequency domain. Only the moduli have been plotted. Note that in (I) and (III) the spectra are not flat because of the velocity contrasts.

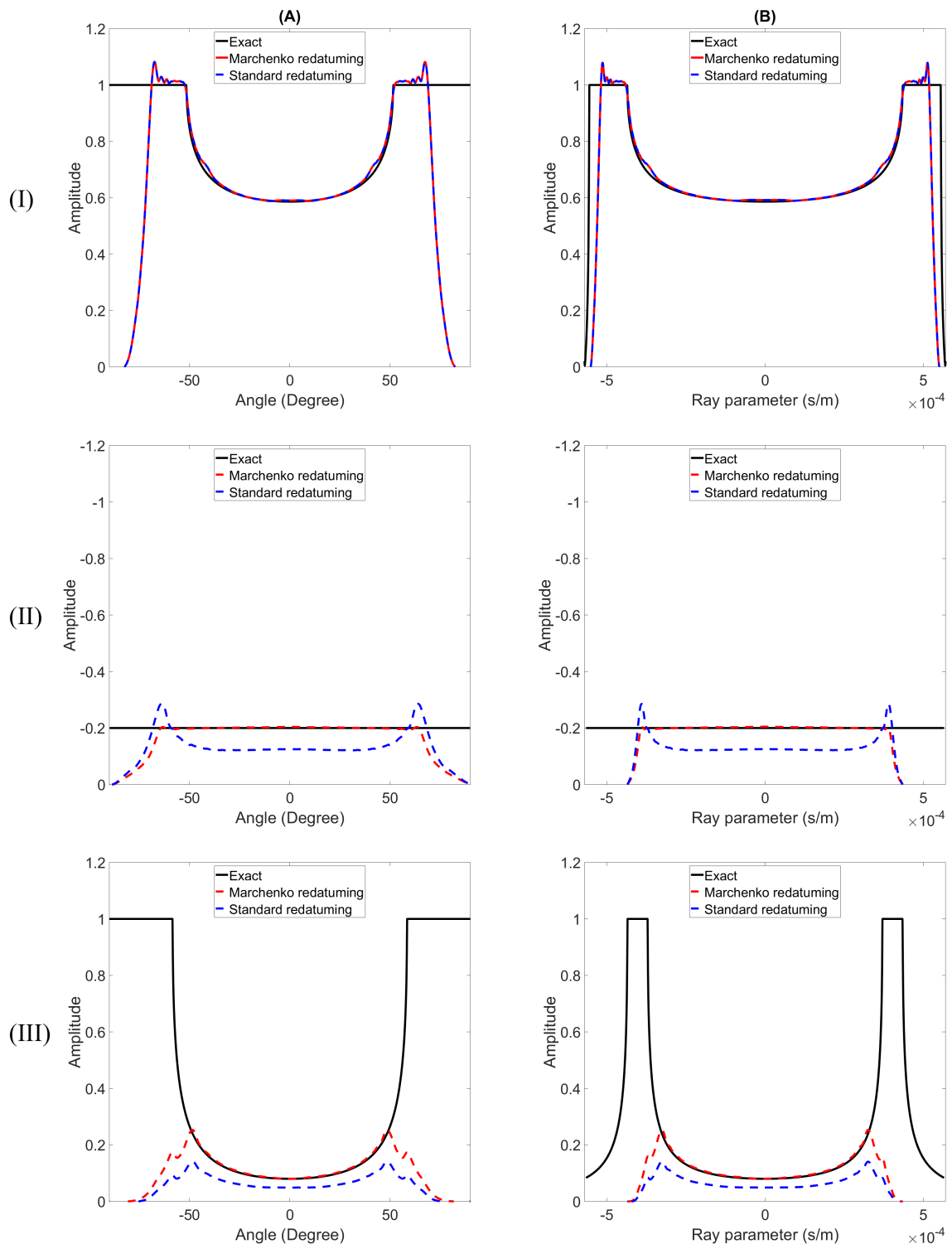


Figure 4-23: The angle-dependent reflectivity obtained by the Marchenko and standard redatuming methods in a medium with varying density and velocity. (I) $z_i = 400$ m. (II) $z_i = 700$ m. (III) $z_i = 1100$ m. (A) Reflectivity as a function of angle. (B) Reflectivity as a function of ray parameter.

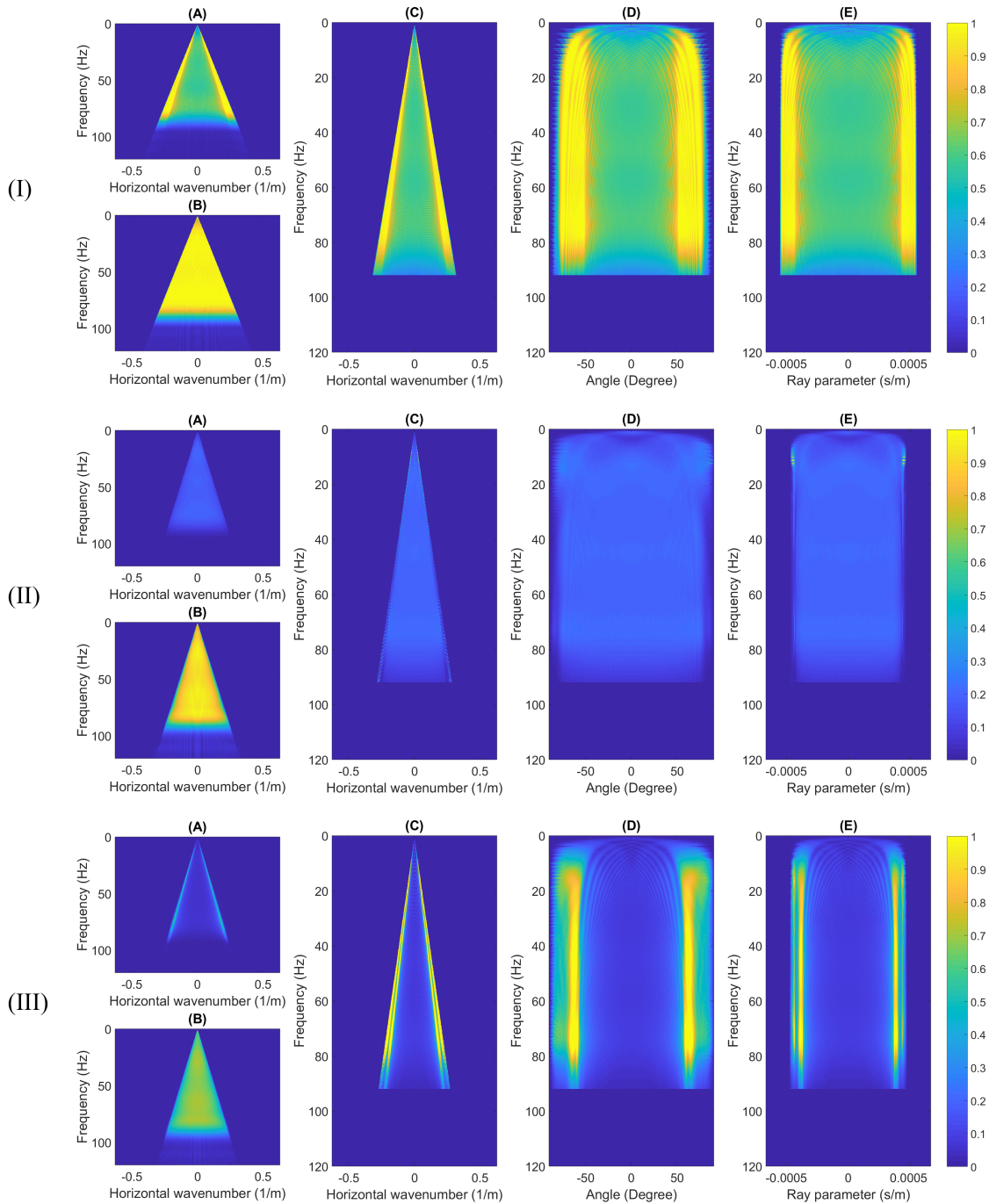


Figure 4-24: Applying the mapping process on $G^{-,+}$ and $G^{-,-}$ which are estimated in a medium with varying density and velocity. The focal point is located at $x = 0$ and (I) $z_i = 400$ m, (II) $z_i = 700$ m, and (III) $z_i = 1100$ m. (A) First arrival of $\tilde{G}^{-,+}(k_x, z_i, \omega)$. (B) First arrival of $\tilde{G}^{-,-}(k_x, z_i, \omega)$. (C) Spectral division. (D) Angle-frequency domain. (E) Ray parameter-frequency domain. Only the moduli have been plotted.

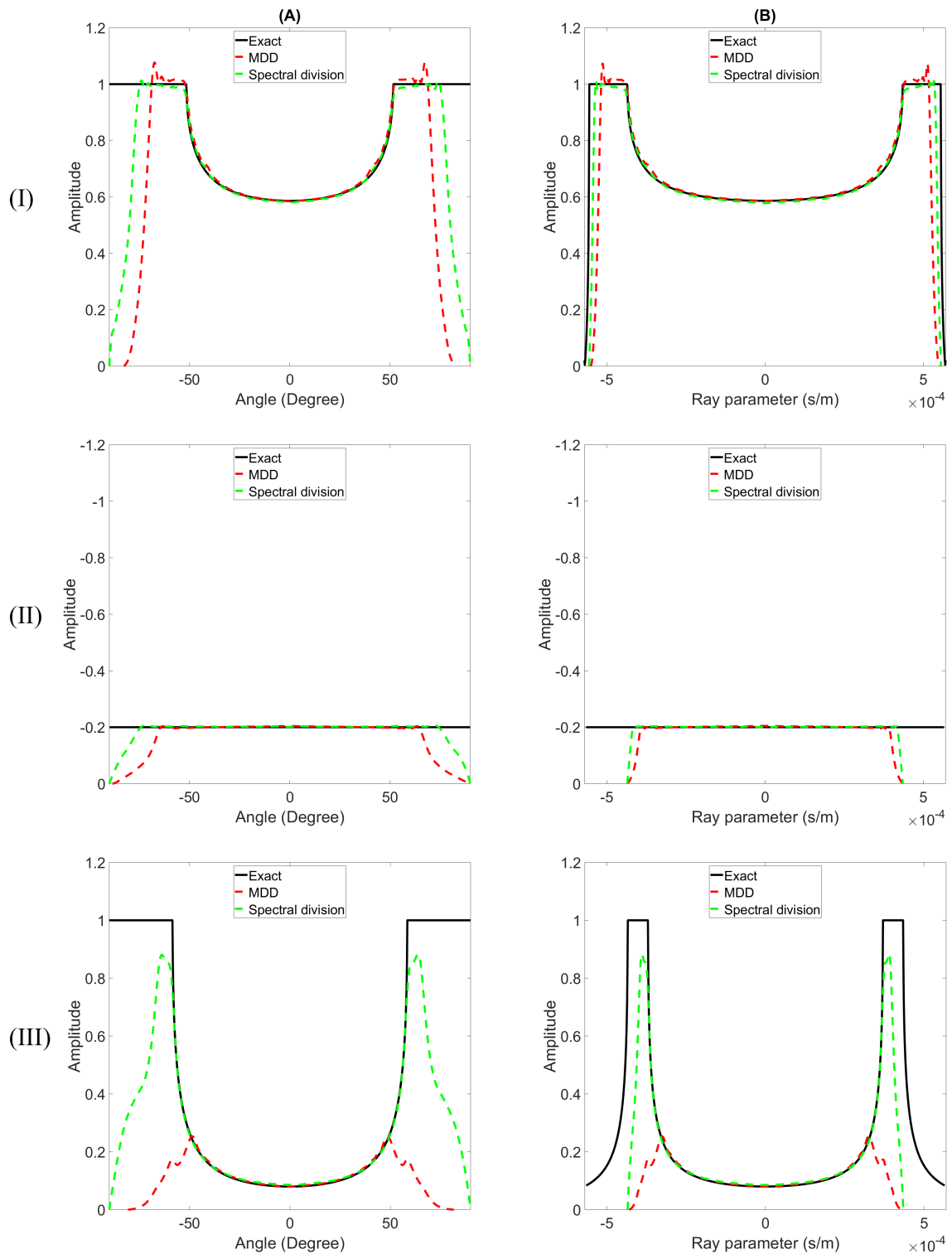


Figure 4-25: The angle-dependent reflectivity obtained by the spectral division and MDD in a medium with varying density and velocity. (I) $z_i = 400$ m. (II) $z_i = 700$ m. (III) $z_i = 1100$ m. (A) Reflectivity as a function of angle. (B) Reflectivity as a function of ray parameter.

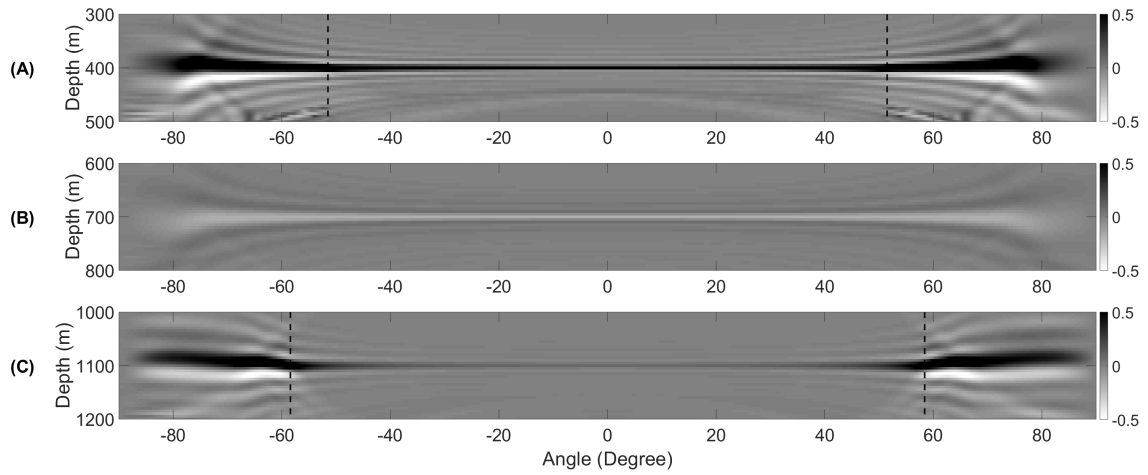


Figure 4-26: Real part of the angle-dependent reflection coefficient as a function of depth in a medium with varying density and velocity. (A) First reflector. (B) Second reflector. (C) Third reflector. The vertical dashed line indicates the critical angle.

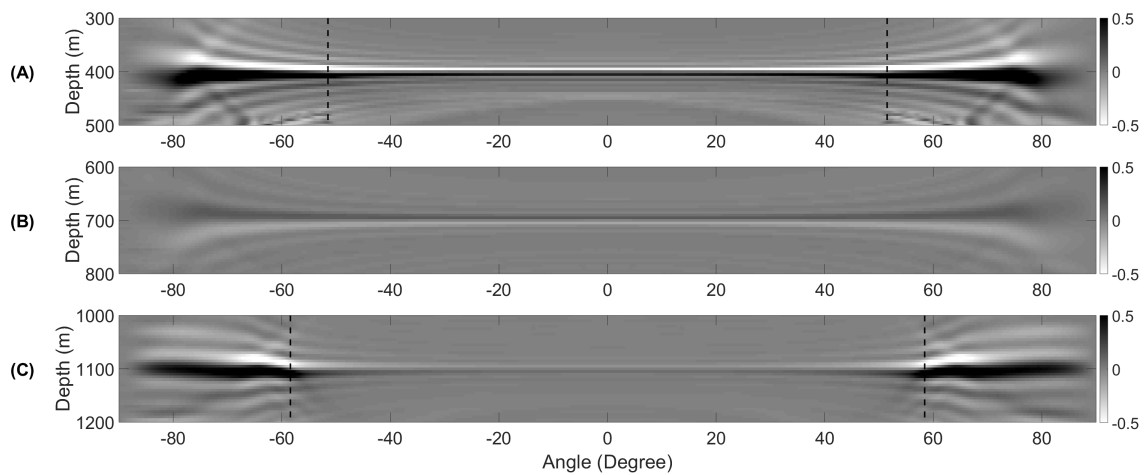


Figure 4-27: Imaginary part of the angle-dependent reflection coefficient as a function of depth in a medium with varying density and velocity. (A) First reflector. (B) Second reflector. (C) Third reflector. The vertical dashed line indicates the critical angle.

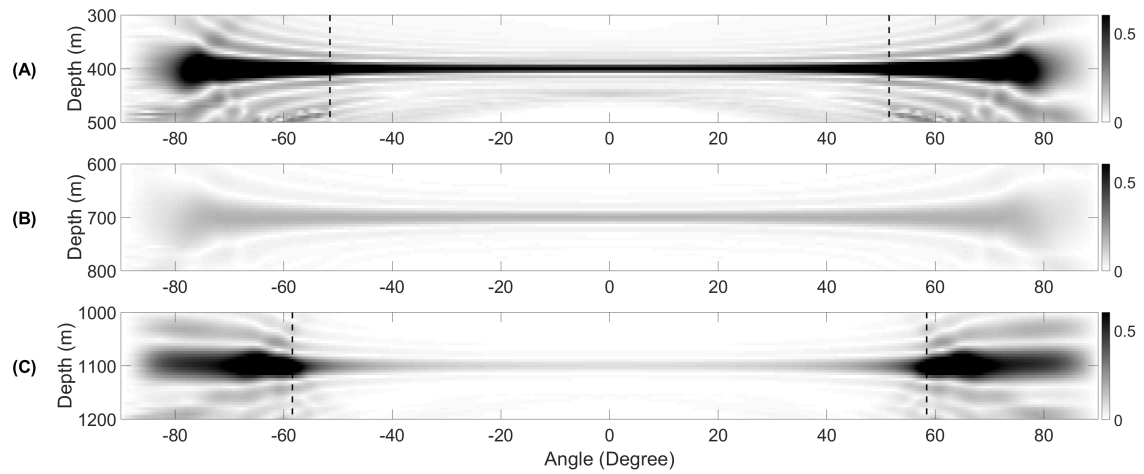


Figure 4-28: Modulus of the angle-dependent reflection coefficient as a function of depth in a medium with varying density and velocity. (A) First reflector. (B) Second reflector. (C) Third reflector. The vertical dashed line indicates the critical angle.

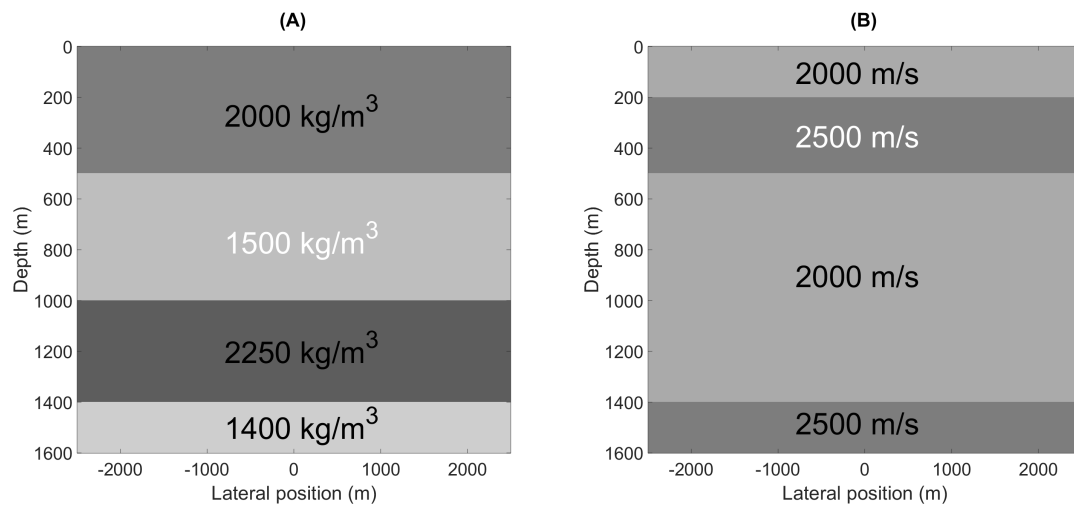


Figure 4-29: A Laterally invariant medium with a low-velocity layer. (A) Density model. (B) Velocity model.

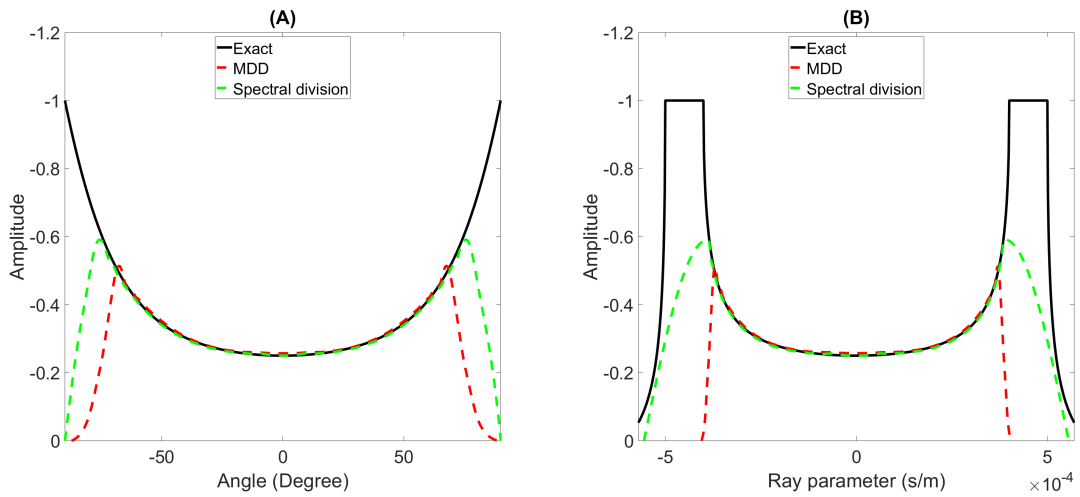


Figure 4-30: The angle-dependent reflectivity obtained by the spectral division and MDD at the low-velocity layer. (A) Reflectivity as a function of angle. (B) Reflectivity as a function of ray parameter.

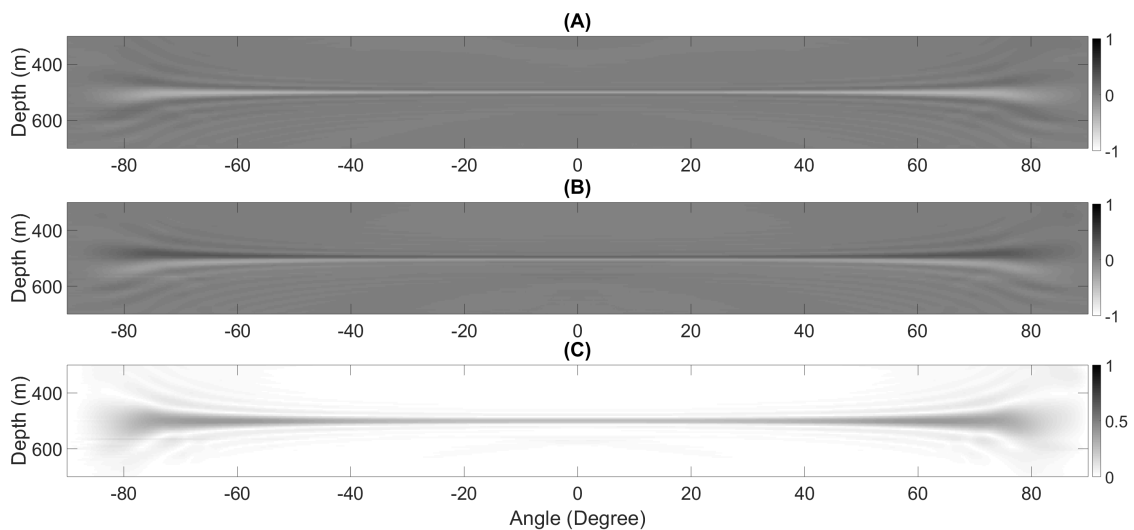


Figure 4-31: Image of the angle-dependent reflectivity for a reflector located above a low-velocity layer. (A) Real part. (B) Imaginary part. (C) Modulus.

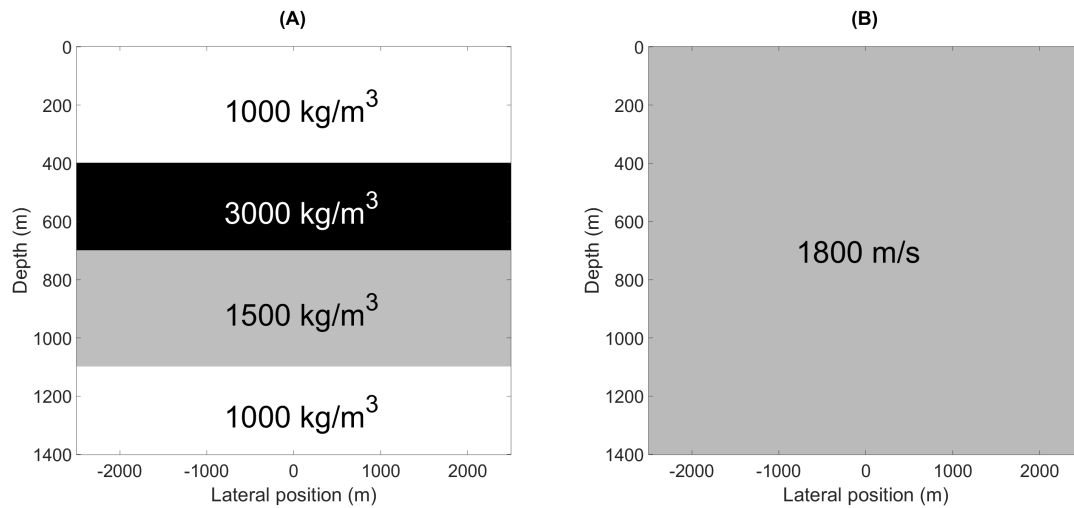


Figure 4-32: The models from which the reflection data are modeled in [section 4-4](#). (A) Correct density model. (B) Correct velocity model.

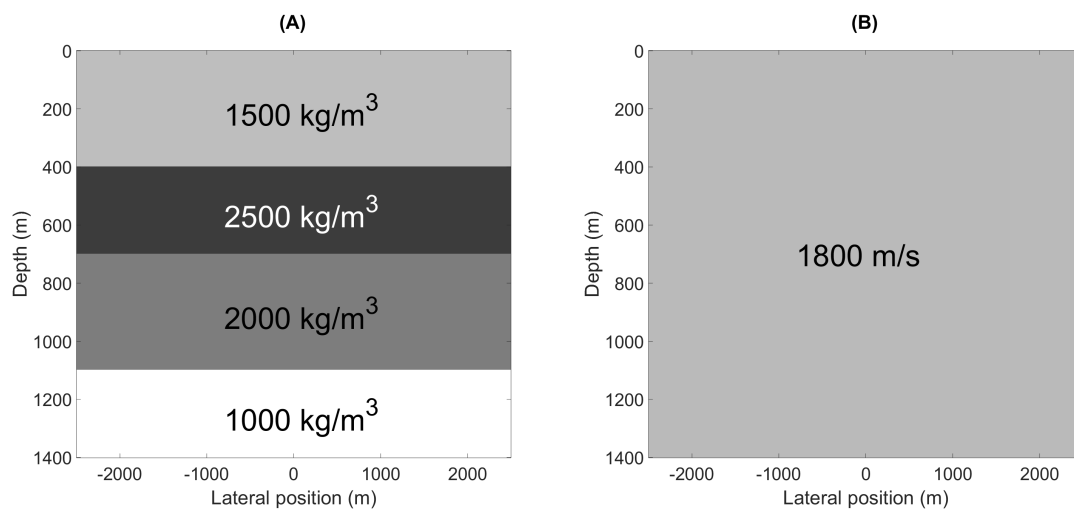


Figure 4-33: The models from which the truncated media are extracted in [section 4-4](#). (A) Wrong density model. (B) Correct velocity model.

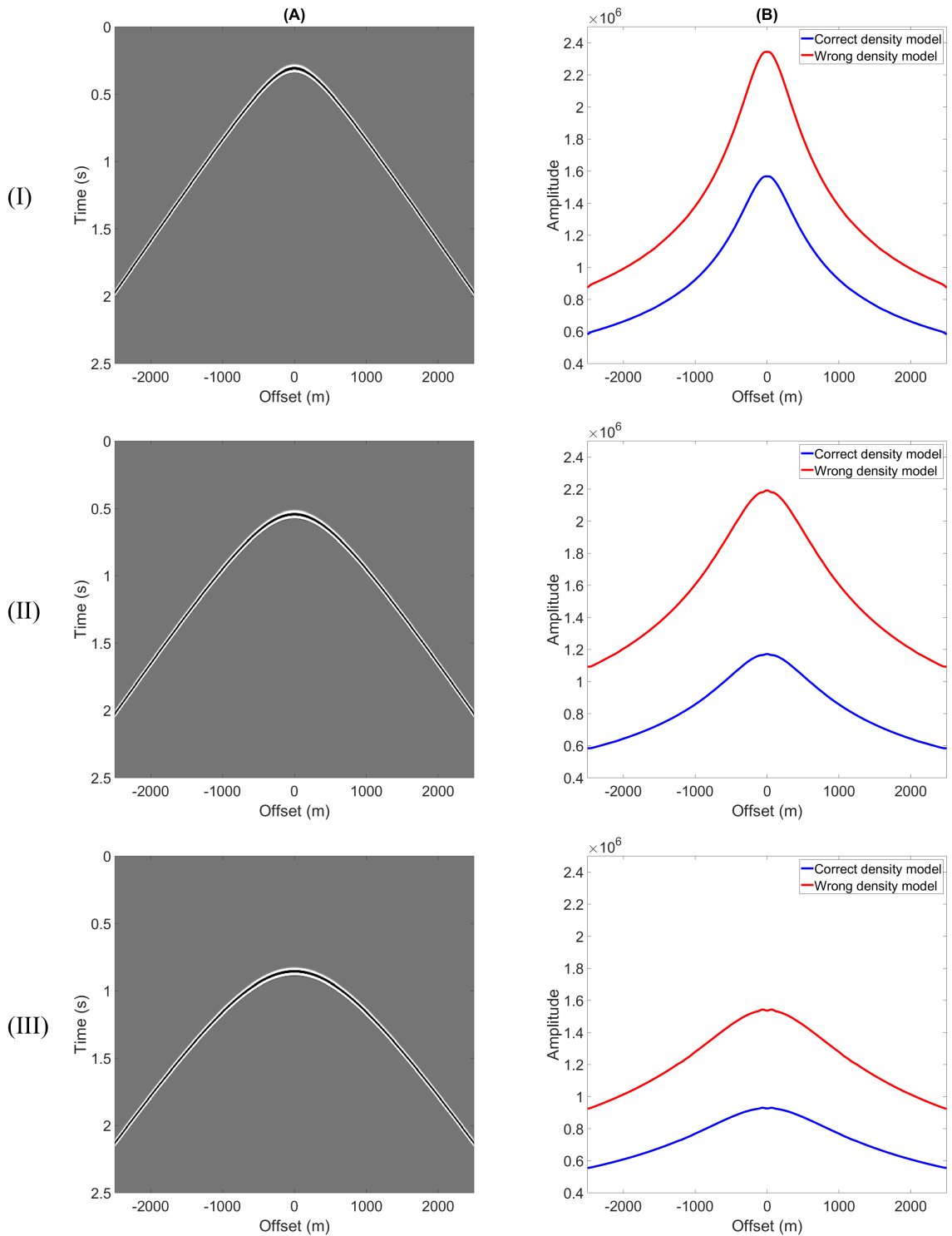


Figure 4-34: Comparison between the direct arrivals estimated from the wrong density model and correct density model. (A) The response of the direct arrival. (B) The AVO response of the direct arrival. The focal point is located at $x = 0$ and (I) $z_i = 400$ m, (II) $z_i = 700$ m, (III) $z_i = 1100$ m. Note that there is a significant difference in amplitude between the correct and wrong direct arrivals.

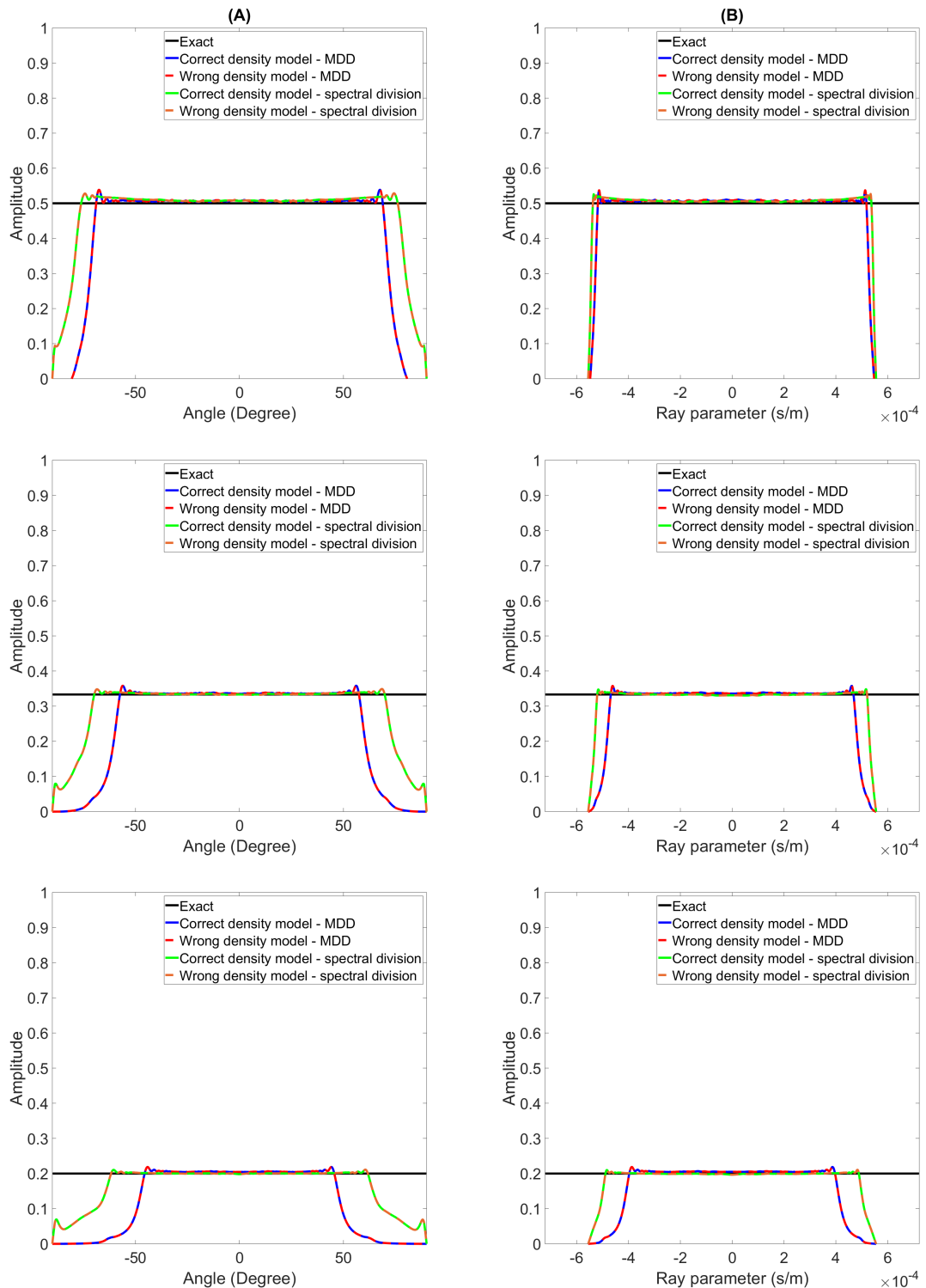


Figure 4-35: The angle-dependent reflectivity obtained using the direct arrivals modeled in the wrong density model and correct density model. The virtual source is located at (I) $z_i = 400$ m, (II) $z_i = 700$ m, and (III) $z_i = 1100$ m. (A) Reflectivity as a function of angle. (B) Reflectivity as a function of ray parameter.

Consequently, the image of the angle-dependent reflectivity of each reflector will be placed in the wrong depth with residual downward curvature (frown) at the far angles. In this case, the imaging process cannot be applied immediately to the depth of each reflector. In fact, the process should be done recursively through the subsurface. For faster computation, the process is applied based on the spectral division with a depth step of 5 m. The real and imaginary parts of the reflectivity are shown in Figure 4-38 and Figure 4-39, respectively. Compared to the results obtained by the correct velocity (see Figure 4-26 and Figure 4-27), it can be seen that the reflectors are placed in the wrong depth levels and have downward curvatures at the far angles. Also, the maximum angle that is retrieved is around 60 degrees, while it reaches 80 degrees when the direct arrival is estimated from the correct velocity model. By using the real and imaginary parts, the modulus can be obtained, as shown in Figure 4-40. By amplitude picking procedure, see Appendix D, the angle-dependent reflectivity can be obtained, as shown in Figure 4-41. It can be seen that the amplitude of the reflectivity can still be recovered correctly up to 60 degrees.

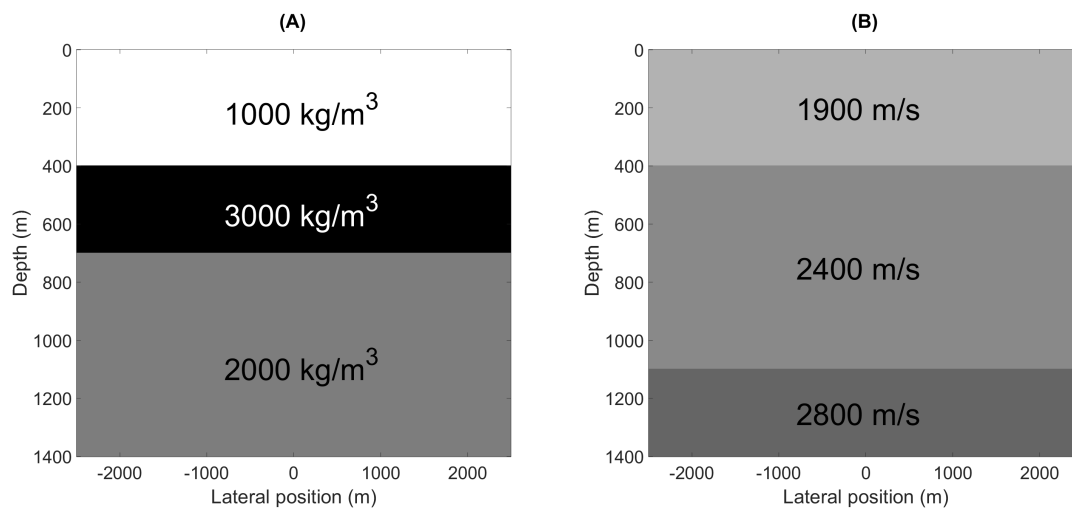


Figure 4-36: The models from which the truncated media are extracted in section 4-5. (A) Correct density model. (B) Wrong velocity model.

4-6 Imaging reflectivity using smooth velocity and density models

In the previous examples, the velocity and density models used to estimate the direct arrivals were composed of different homogeneous layers separated by interfaces. In practice, however, the velocity and density models are often estimated as smooth versions of the exact models. Here, the example in section 4-2 is repeated, but now the truncated media are extracted from the models shown in Figure 4-42. The velocity and density models are smooth versions of the models in Figure 4-19. This was done by applying a moving average filter with a length of 100 m. The direct arrival, in this case, will have smooth ray paths and smooth reflectivity. Therefore, there will be some errors in the amplitudes and arrival times of the direct arrivals.

As established in section 4-4, the error in the amplitude is compensated in the deconvolution process. Similar to section 4-5, the imaging process are applied recursively through the subsurface using the spectral division with a depth step of 5 m. The image of the real part of the angle-dependent reflectivity is shown in Figure 4-43. It can be seen that the image of the first and second reflectors are placed at the

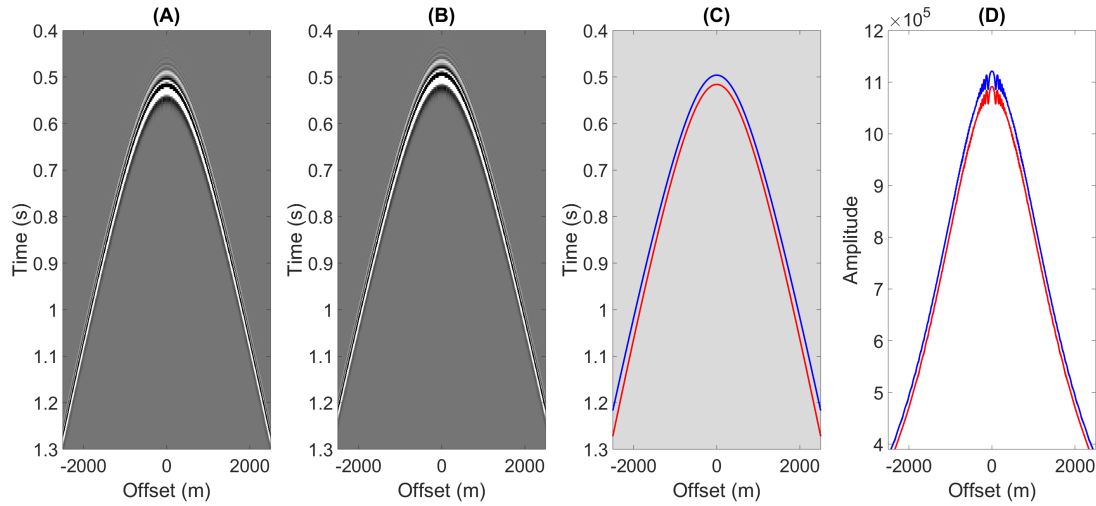


Figure 4-37: Comparison between the direct arrivals estimated from the wrong velocity model and correct velocity model. The focal point is located at $x = 0$ and $z_i = 1100$ m. (A) Direct arrival based on a correct velocity model. (B) Direct arrival based on a wrong velocity model. (C) Projection of the travel time from (A) and (B). The blue curve refers to the incorrect velocity model while the red curve refers to the correct velocity model. (D) Amplitude of the direct arrival as a function of offset.

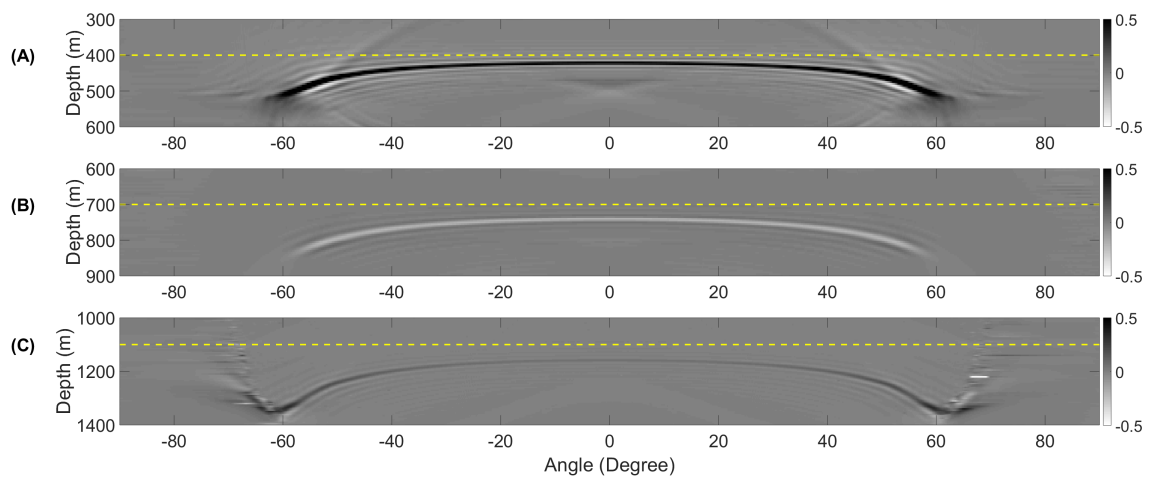


Figure 4-38: Real part of the angle-dependent reflection coefficient as a function of depth obtained using direct arrivals modeled from a wrong velocity model. (A) First reflector. (B) Second reflector. (C) Third reflector. The horizontal yellow dashed line represents the true depth of the reflector.

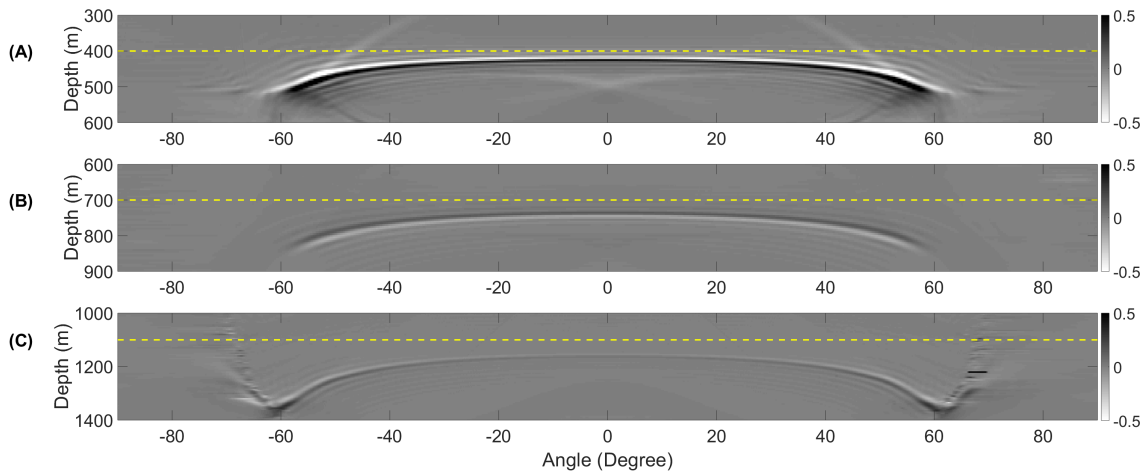


Figure 4-39: Imaginary part of the angle-dependent reflection coefficient as a function of depth obtained using direct arrivals modeled from a wrong velocity model. (A) First reflector. (B) Second reflector. (C) Third reflector. The horizontal yellow dashed line represents the true depth of the reflector.

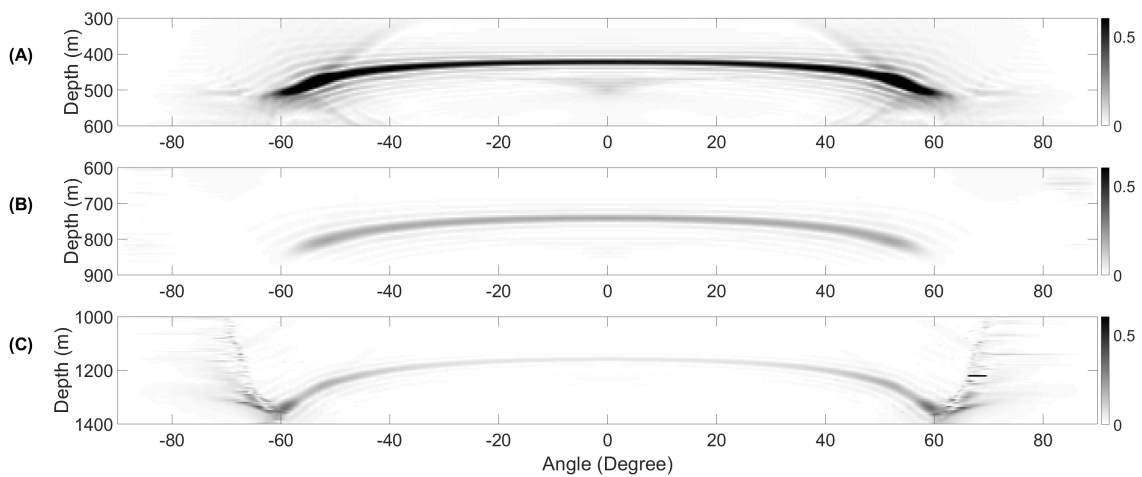


Figure 4-40: Modulus of the angle-dependent reflection coefficient as a function of depth obtained using direct arrivals modeled from a wrong velocity model. (A) First reflector. (B) Second reflector. (C) Third reflector.

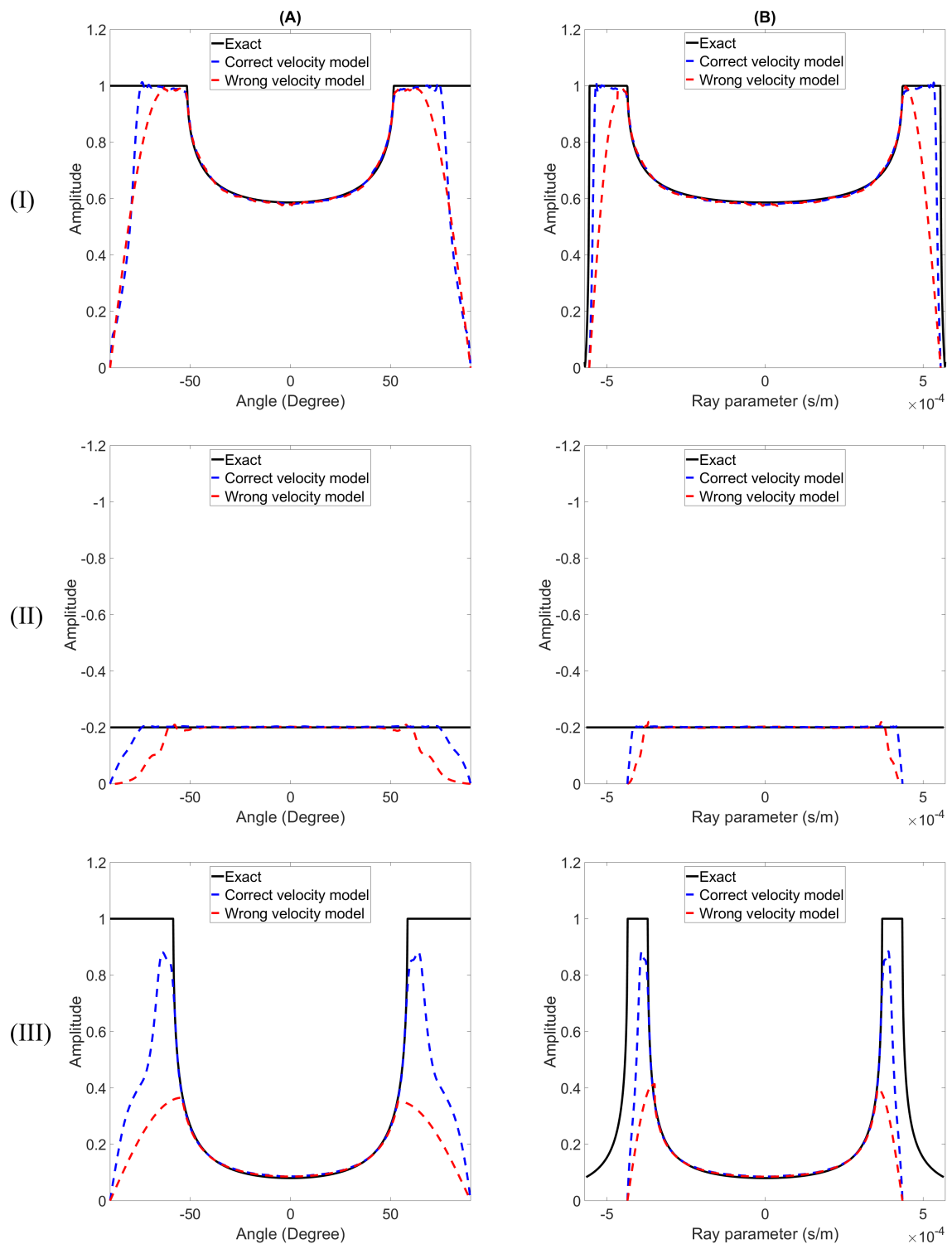


Figure 4-41: The angle-dependent reflectivity obtained using the direct arrivals modeled in the wrong velocity model and correct velocity model. (I) First reflector. (II). Second Reflector. (III) Third reflector. (A) Reflectivity as a function of angle. (B) Reflectivity as a function of ray parameter.

correct depth levels. However, at the second reflector, the event starts curving up at the very far angles. This could be explained by the inaccuracy in the arrival times of the direct arrival estimated from the smooth models. At the third reflector, the effect is more pronounced with a downward curvature at the far angles. In addition, the third reflector is located 10 m below the true depth level. The image of the modulus is shown in Figure 4-44. By a picking procedure, the angle-dependent reflectivity is obtained, as shown in Figure 4-45. It can be seen that the range of angles that can be covered is almost the same as the one estimated by the correct models. Bear in mind that the smooth density and velocity models are based on these correct models. Therefore, the error is much less than when they are estimated from inaccurate models.

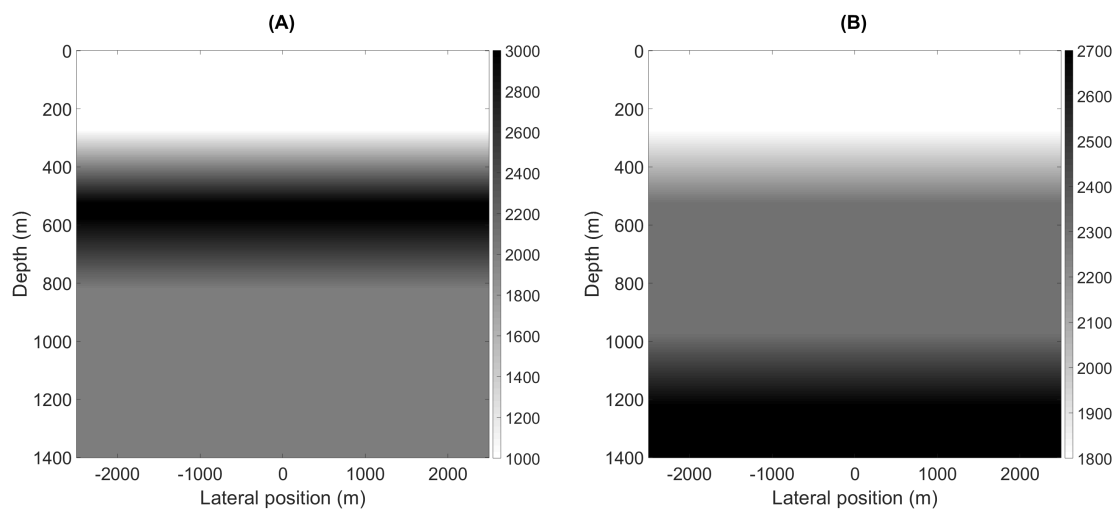


Figure 4-42: Smooth version of the density and velocity models in Figure 4-19. A moving average filter of length 100 m has been applied. (A) Density model. (B) velocity model.

4-7 Imaging reflectivity in the presence of random noise

In this example, the same model in section 4-2 is considered but noise added to the reflection data, see Figure 4-46. The signal-to-noise ratio (SNR) is 20 dB. The noise amplitude distribution is Gaussian. Note that the response from the deepest reflector can barely be seen. The angle-dependent reflectivity results, obtained by the Marchenko method from these noisy data, are shown in Figure 4-47. The effect of the noise can be observed from the deviations around the exact results. At deeper reflectors, the estimation of the reflectivity becomes more uncertain, however, the trend can still be determined from these results.

4-8 Imaging reflectivity in an invisible medium

Following a similar example as Zhang et al. (2019), a horizontally layered model is considered with a constant layer thickness of 200 m and constant velocity of 1500 m/s; only the mass density in the different layers varies, as shown in Figure 4-48. The model parameters are chosen such that the primary reflection of the third reflector cancels the first internal multiple between the first and second

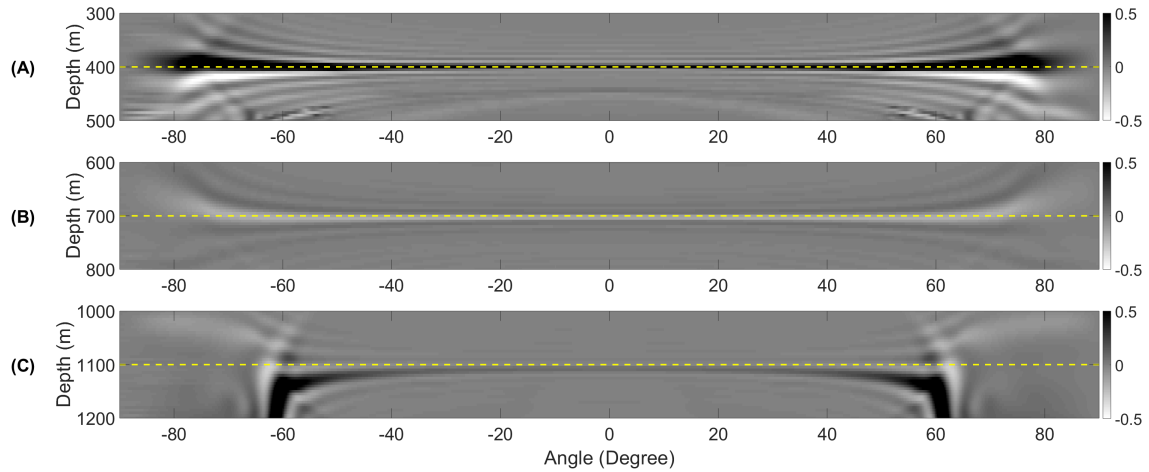


Figure 4-43: Real part of the angle-dependent reflection coefficient as a function of depth obtained using direct arrivals modeled from smooth density and velocity models. (A) First reflector. (B) Second reflector. (C) Third reflector. The horizontal yellow dashed line represents the true depth of the reflector. Note that at the second reflector, the event starts curving up at the very fat angles, while it is curving down in the third reflector. Also, the third reflector is located 10 m below the true depth.

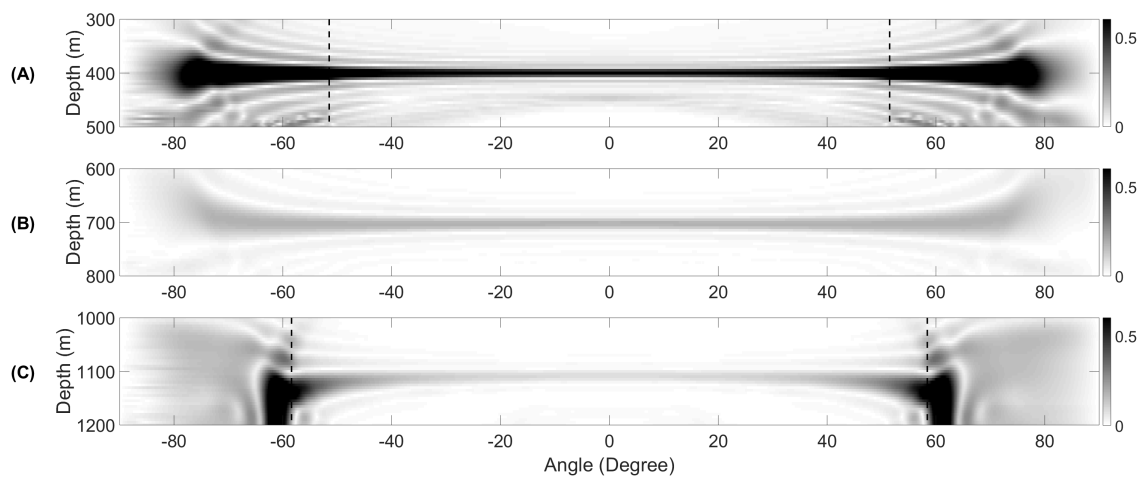


Figure 4-44: Modulus of the angle-dependent reflection coefficient as a function of depth obtained using direct arrivals modeled from smooth density and velocity models. (A) First reflector. (B) Second reflector. (C) Third reflector. The vertical dashed line indicates the critical angle.

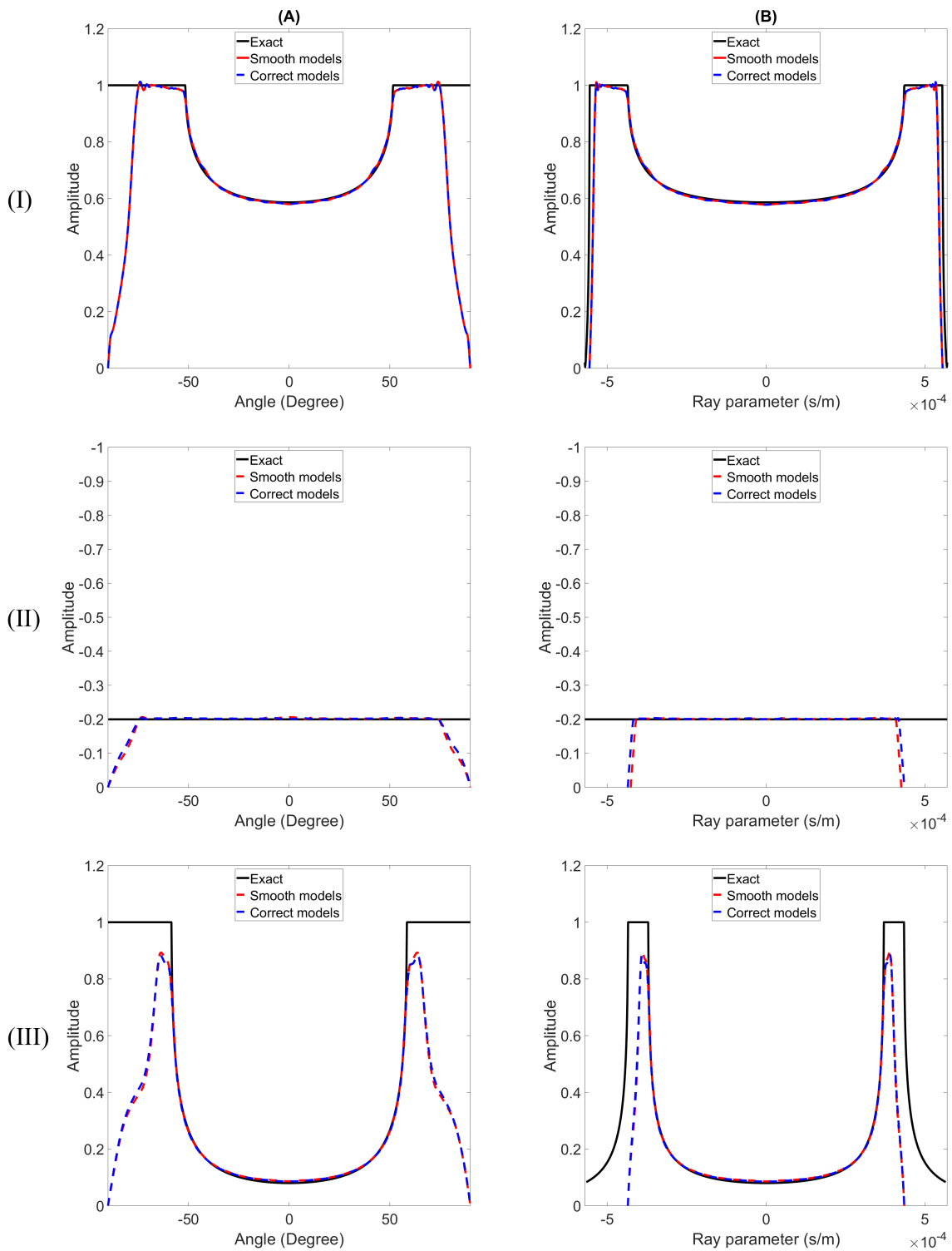


Figure 4-45: The angle-dependent reflectivity obtained using the direct arrivals modeled in the smooth models and correct models. (I) First reflector. (II). Second Reflector. (III) Third reflector. (A) Reflectivity as a function of angle. (B) Reflectivity as a function of ray parameter.

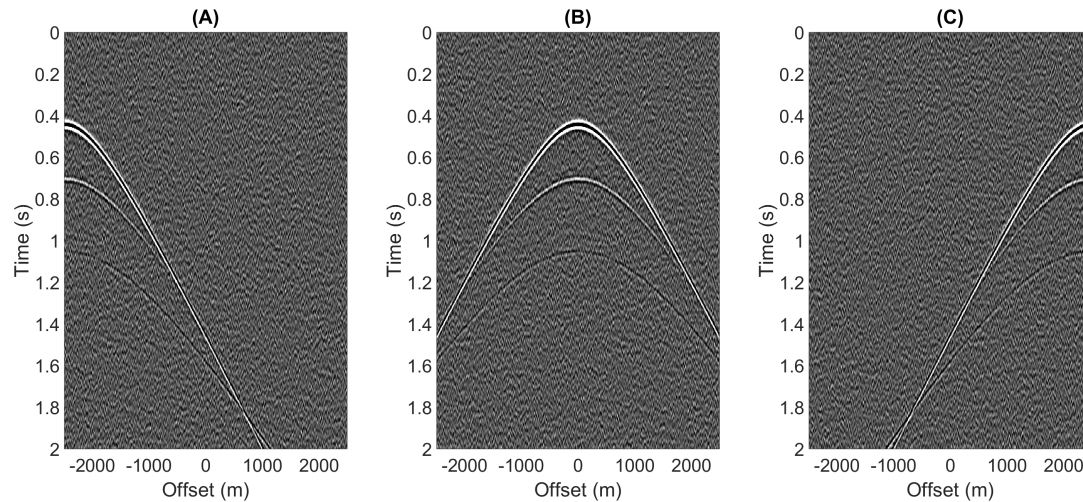


Figure 4-46: The modeled reflection response in Figure 4-20 after adding noise with SNR of 20 dB and Gaussian distribution. The source is located at the surface and (A) $x = -2500$ m, (B) $x = 0$, and (C) $x = 2500$ m.

reflectors. The third reflector causes a new internal multiple, that is canceled by the primary reflection from the fourth reflector, and so on. Consequently, the reflection response is invisible from the third reflector onward, as shown in Figure 4-49.

The approach is tested by applying the imaging process on the first six reflectors. By estimating the redatumed response at the depth of each reflector, it can be seen that the method does not only estimate the redatumed response of the visible reflectors but also recovers the redatumed response of the invisible reflectors, see Figure 4-50. Note that the deeper reflectors require larger number of iterations. For example, the scheme converges at $k = 14$ for the third reflector and $k = 27$ for the sixth reflector. By applying the imaging process on these six reflectors, the angle-dependent reflectivity is correctly obtained, as shown in Figure 4-51.

4-9 Imaging reflectivity in the presence of a dipping interface

In this example, a model is considered with a dipping interface and constant velocity; only the mass density in the different layers varies, as shown in Figure 4-52. The dipping interface has a dip of about 2.2 degrees. Because of the presence of the dipping interface, the surface reflection response $R(\mathbf{x}_0'', \mathbf{x}_0, t)$ is asymmetric with respect to $x = 0$, and the zero-offset travel times are not the same for the different shot records, see Figure 4-53. The imaging process is applied immediately to the reflectors. Note that the spectral division does not work here because the medium is laterally variant. For the dipping interface, the imaging process is applied by placing the sources and receivers parallel to the reflector (i.e. virtual dipping acquisition surface). In this case, the direct arrival $G_d(\mathbf{x}_0'', \mathbf{x}_i', t)$ is modeled from every grid point along the dipping interface, as shown in Figure 4-54. The estimated angle-dependent reflectivity of the three reflectors are depicted in Figure 4-55. It can be seen that the Marchenko method successfully retrieves the angle-dependent reflectivity of the reflectors located below the dipping interface (Figure 4-55II-C and III-C). For the dipping interface, the reflectivity is only recovered around the zero-incidence angle, see Figure 4-55I-C. This shows that redatuming

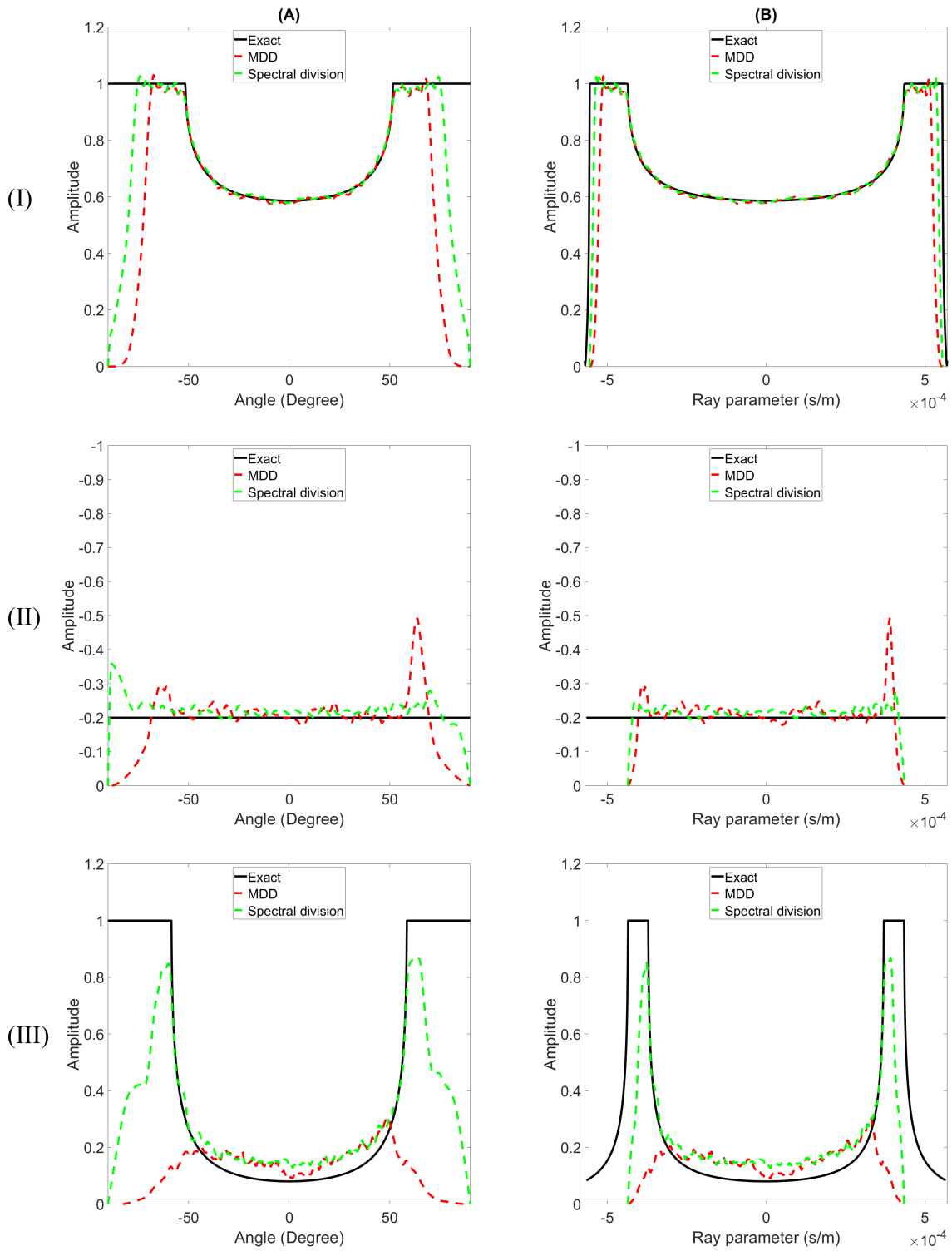


Figure 4-47: The angle-dependent reflectivity in the presence of random noise. (I) $z_i = 400$ m. (II) $z_i = 700$ m. (III) $z_i = 1100$ m. (A) Reflectivity as a function of angle. (B) Reflectivity as a function of ray parameter.

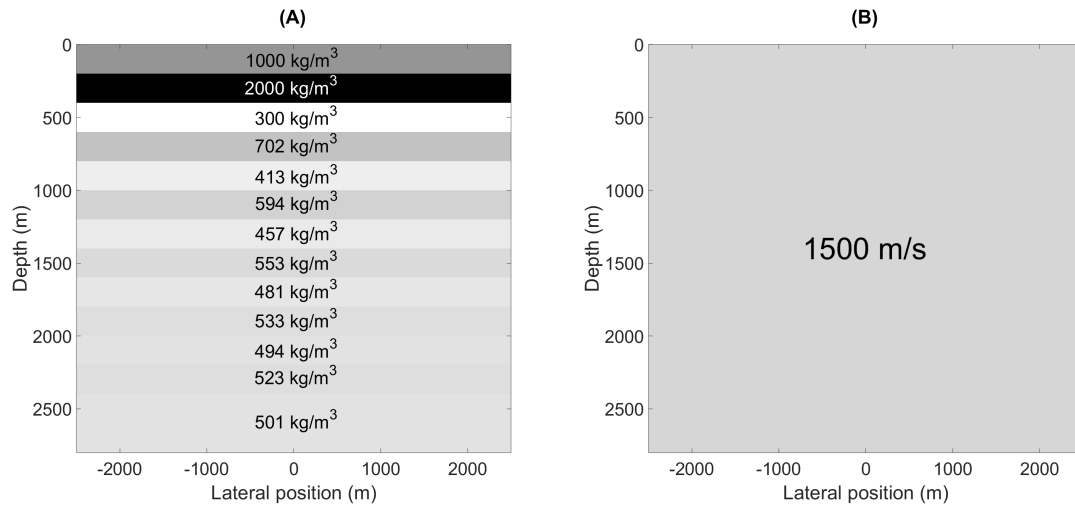


Figure 4-48: Invisible medium with a constant layer thickness of 200 m. (A) Density model. (B) velocity model.

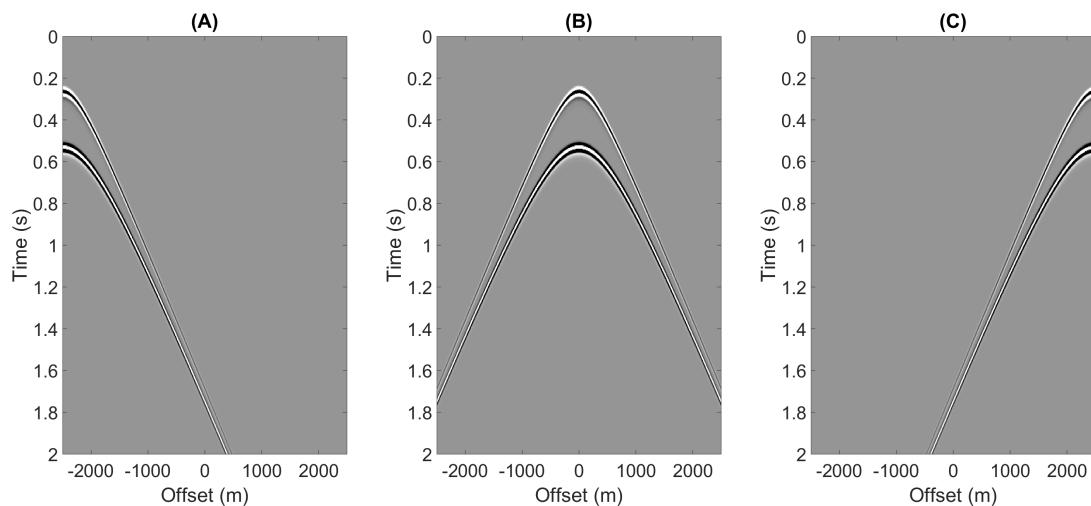


Figure 4-49: The modeled reflection response of the invisible medium. Note that only the primary reflection of the first two reflectors are visible. The source is located at the surface and (A) $x = -2500$ m, (B) $x = 0$, and (C) $x = 2500$ m.

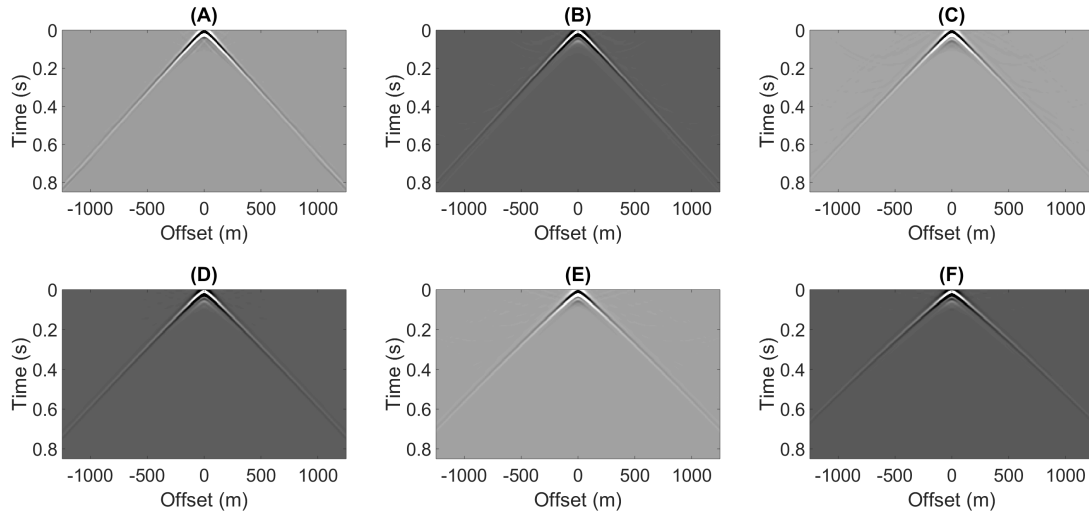


Figure 4-50: Redatumed reflection response $R(\mathbf{x}_i, \mathbf{x}'_i, t)$ obtained by the Marchenko method in the invisible medium. The virtual source is located at $x = 0$ and (A) $z_i = 200$ m, (B) $z_i = 400$ m, (C) $z_i = 600$ m, (D) $z_i = 800$ m, (E) $z_i = 1000$ m, and (F) $z_i = 1200$ m.

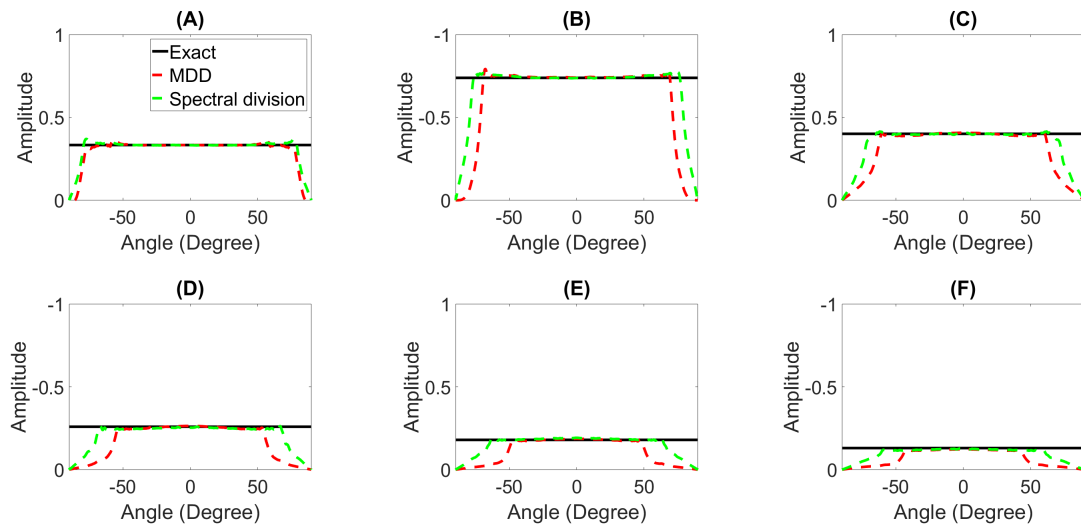


Figure 4-51: Angle-dependent reflectivity obtained by the Marchenko method in the invisible medium. (A) $z_i = 200$ m, (B) $z_i = 400$ m, (C) $z_i = 600$ m, (D) $z_i = 800$ m, (E) $z_i = 1000$ m, and (F) $z_i = 1200$ m.

the reflection data to a dipping acquisition surface is not sufficient to estimate the angle-dependent reflectivity. When considering an inhomogeneous velocity model, as shown in Figure 4-56, the effects of the dipping layer propagates significantly to the deeper horizontal layers, as shown in Figure 4-57. In this case, the reflectivity is only estimated correctly around the zero-incidence angle for all reflectors.

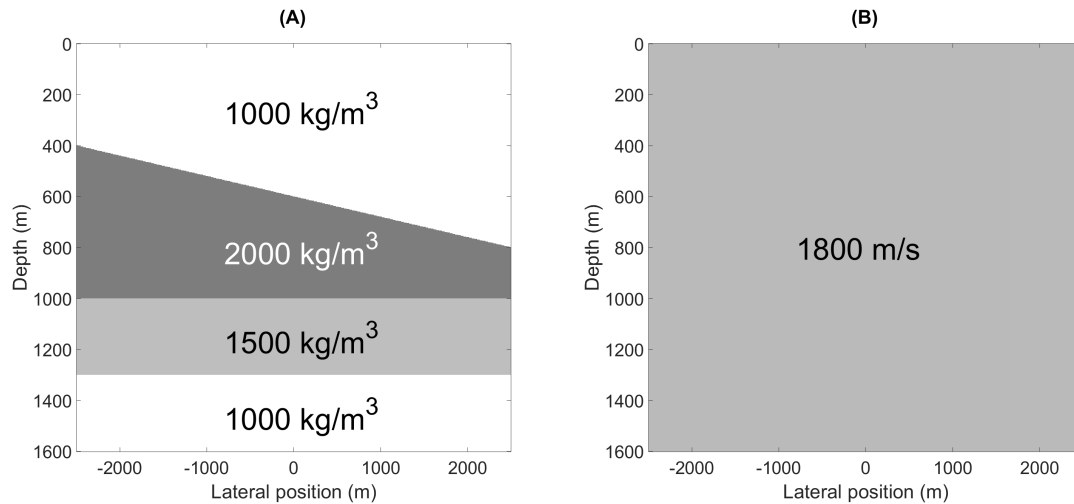


Figure 4-52: Dipping interface in a medium with constant velocity and varying density. (A) Density model. (B) velocity model.

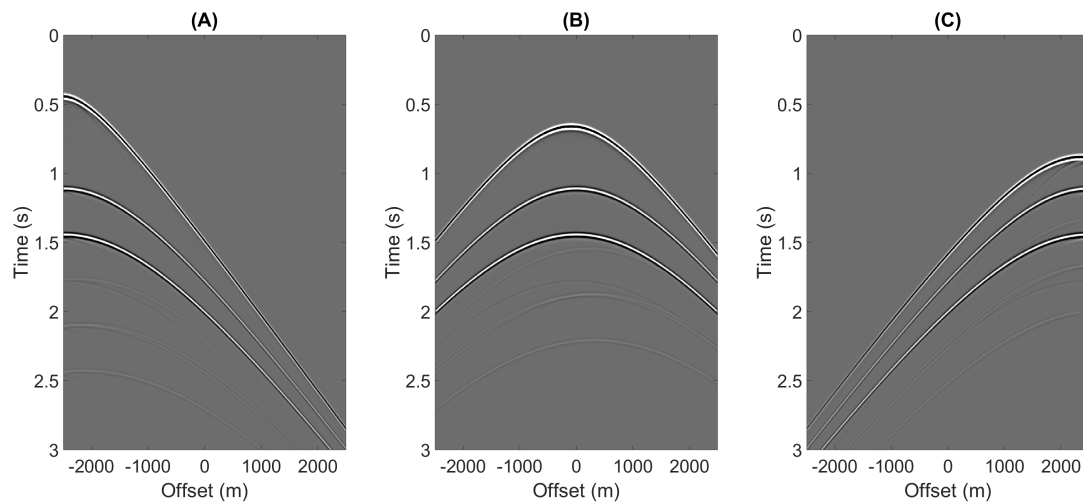


Figure 4-53: The modeled reflection response in the presence of a dipping interface (see Figure 4-52). The source is located at the surface and (A) $x = 2500\text{m}$, (B) $x = 0$, and (C) $x = 2500\text{m}$. Note the reflection response is asymmetric and the zero-offset travel time is not the same for these three shot records.

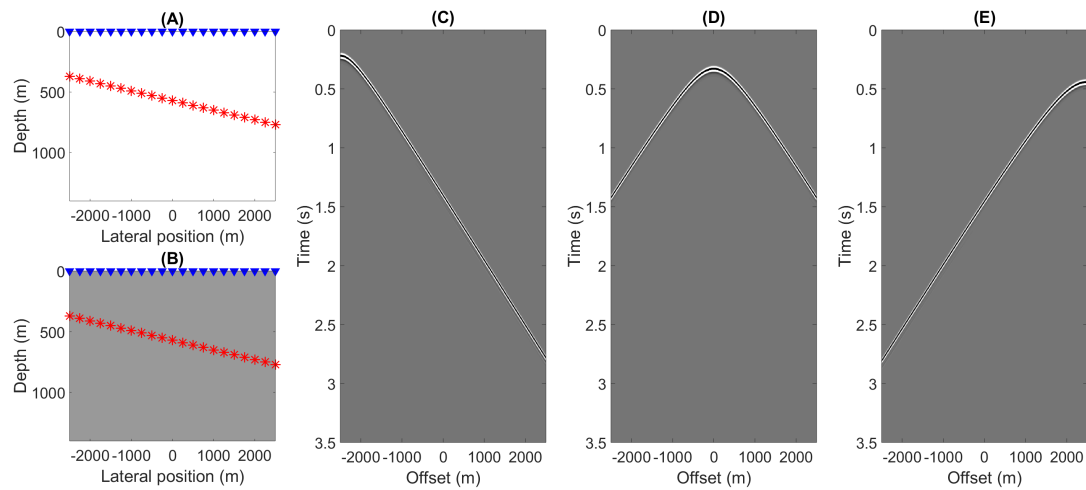


Figure 4-54: Modeled direct arrivals $G_d(\mathbf{x}''_0, \mathbf{x}'_i, t)$ from sources (red asterisks) located along the dipping interface and recorded by receivers (blue triangles) at the surface. The (A) density model and (B) velocity model are extracted from the models in Figure 4-52. (C) $\mathbf{x}'_i = (-2500, 400)$. (D) $\mathbf{x}'_i = (0, 600)$. (E) $\mathbf{x}'_i = (2500, 800)$.

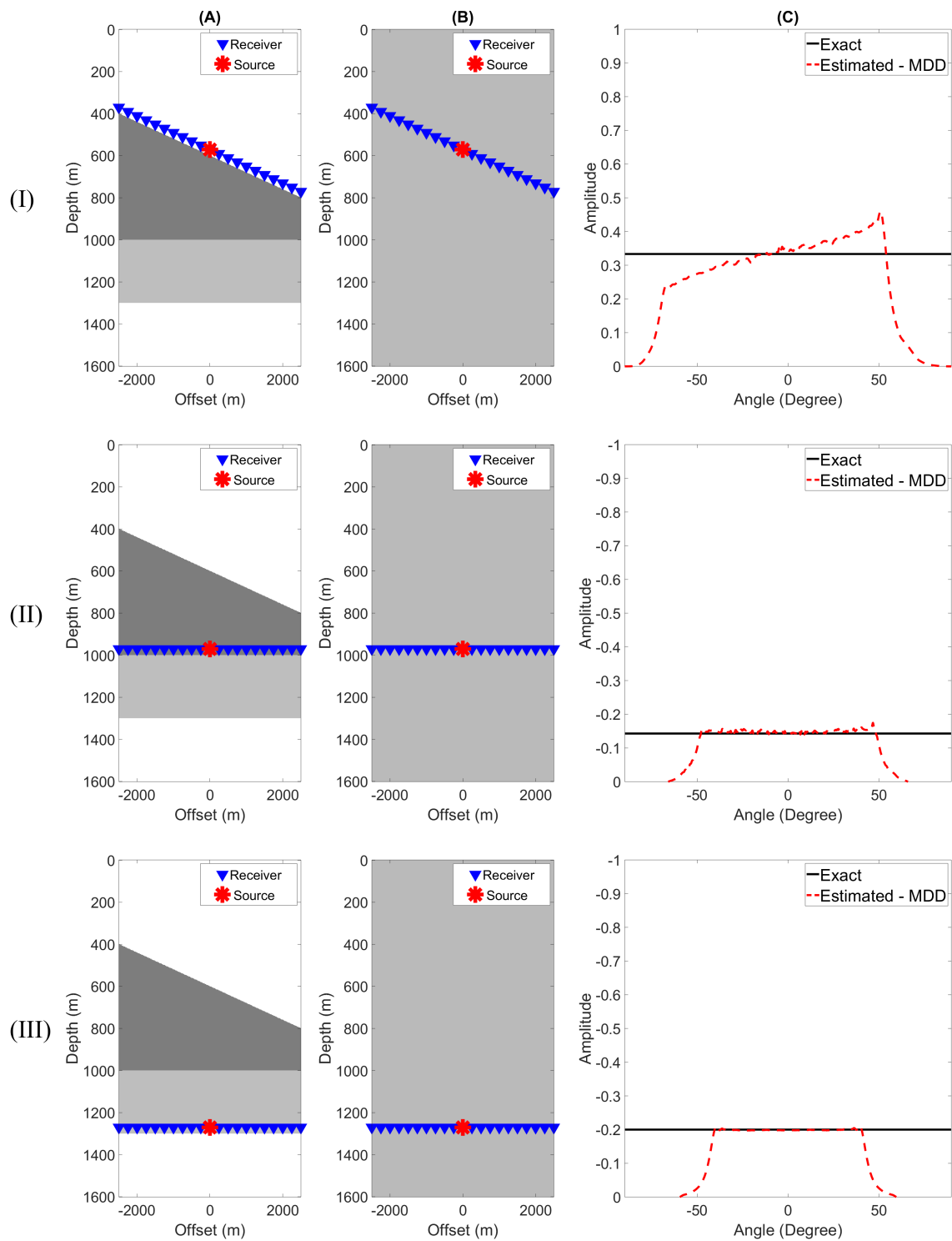


Figure 4-55: Angle-dependent reflectivity in the presence of a dipping interface with constant velocity and varying density. (I) First reflector. (II) Second reflector. (III) Third reflector. (A) Density model. (B) Velocity model. (C) Angle-dependent reflectivity. Bear in mind that the effects of the layers above the redatuming level are removed by the MDD process.

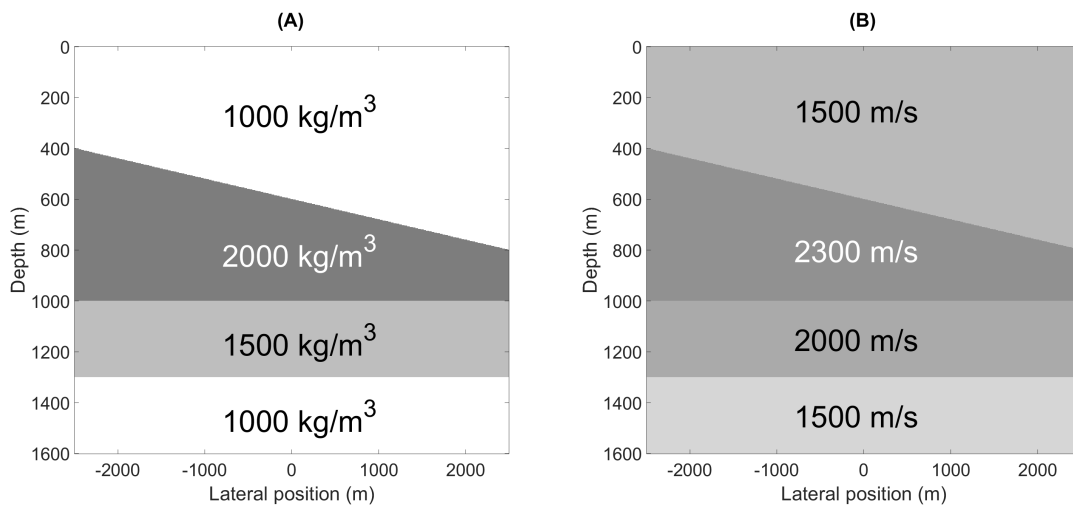


Figure 4-56: Dipping interface in a medium with a varying velocity and density. (A) Density model. (B) velocity model.

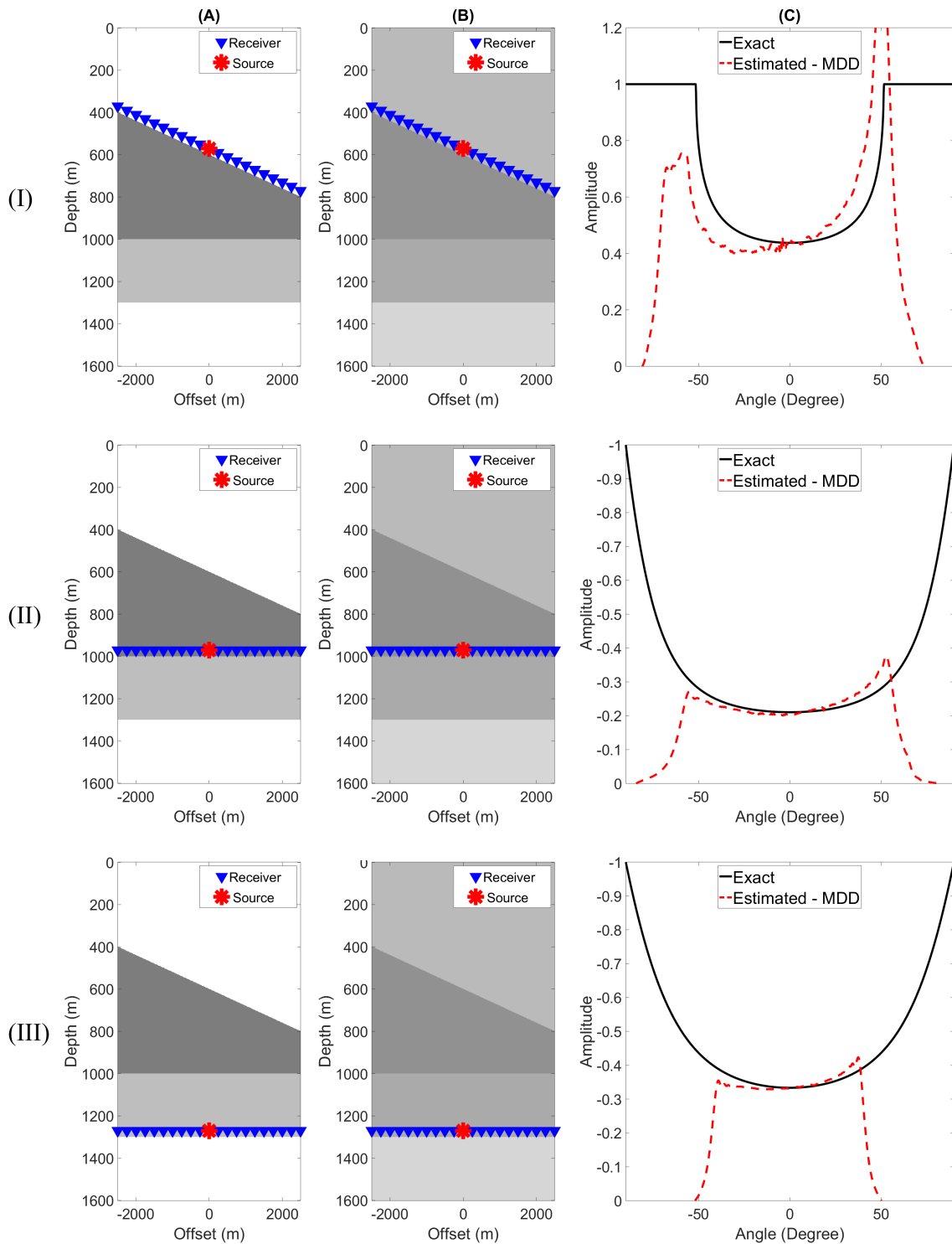


Figure 4-57: Angle-dependent reflectivity in the presence of a dipping interface with varying velocity and density. (I) First reflector. (II) Second reflector. (III) Third reflector. (A) Density model. (B) Velocity model. (C) Angle-dependent reflectivity.

Chapter 5

Discussion and Conclusion

It has been shown that the angle-dependent reflectivity can be correctly retrieved using the Marchenko method. A surface reflection response and an approximation of the direct arrival from the location of the virtual source are required for this method. This information is used as input in the Marchenko iterative scheme to obtain the upgoing and downgoing Green's functions related to a virtual source located in the subsurface. By deconvolving the upgoing Green's function with the downgoing Green's function, a redatumed reflection response is obtained with the correct events and amplitudes. The errors in the Green's functions are significantly eliminated by the deconvolution process, as long as both Green's functions contain the same error. In this case, no correction is necessary for the direct arrival before estimating the Green's functions. The application of the imaging principle allows one to preserve the angle-dependent reflectivity from such a redatumed response by summing all frequency components along lines of constant ray parameter or angle. This information can be potentially used as input in a subsequent AVO inversion process to obtain the medium parameters of the target. These parameters can be linked to geological properties in order to identify the characteristics of the subsurface.

With numerical examples, the approach has shown the potential to retrieve the true angle-dependent reflectivity in the presence of a high-contrast medium. This suggests that the approach can image the angle-dependent reflectivity of a target located below a strongly scattering medium. In addition, the approach can be applied immediately to the target zone without resolving the overburden. In the invisible medium example, the approach has shown that the Marchenko method worked excellent to retrieve the invisible events, which in the data were canceled because of the internal multiples, with the correct reflectivity. In a medium with varying velocity and density, the approach has been able to correctly estimate the angle-dependent reflectivity up to the critical angle. This limitation is due to the fact that the Marchenko method cannot deal with head waves and evanescent waves. In practical situations, the approach had shown that the angle-dependent reflectivity could still be preserved even when the direct arrival was estimated from inaccurate density and velocity models. The use of an inaccurate density model introduced errors to the amplitudes of the direct arrivals, which were canceled by the deconvolution process. However, the presence of random noise could not be completely eliminated by this process because the error was no longer the same for both Green's functions. The random noise effect was more pronounced at deep targets, where the signal-to-noise

ratio is typically low. The use of an inaccurate velocity model, which caused an erroneous time shift and residual moveout, produced an image with wrong depth and reduced the maximum angle for which the reflectivity can be retrieved. Despite these effects, the approach correctly estimated the angle-dependent reflectivity. In the presence of a dipping interface above horizontal layers, the approach obtained the correct reflectivity along the horizontal layers. However, when the velocity varies with depth, the effect of the dipping interface significantly propagates to the horizontal layers. In this case, only the zero-incidence reflectivity is obtained. This shows that the approach is still insufficient for estimating the angle-dependent reflectivity in laterally variant media, and more work is needed.

The Marchenko iterative scheme, which serves as the driving algorithm in the Marchenko method, solves the coupled Marchenko equations for the focusing and Green's functions. At every iteration, the focusing functions are updated, and the Green's functions are subsequently updated. It has been seen that in order to fully retrieve the reflectivity, the scheme had to converge. The number of iterations required for convergence depends on the reflectivity and number of events in the model. For example, the deeper targets in the invisible medium required a larger iteration number. This makes the Marchenko method a costly process, especially when applying the imaging process to many depth levels in the target zone. Alternatively, the imaging process should be applied with relatively small depth steps. Such a solution requires selecting the depth steps with care; otherwise, the angle-dependent reflectivity may be incorrectly estimated.

The maximum angle that can be achieved depends on the design of the surface acquisition. The evaluated integrals in the coupled Marchenko equations contain stationary points that should be recorded at the surface in order to retrieve particular events of the Green's functions and focusing functions. Typically, deep reflectors will require a wide-angle seismic acquisition due to the effect of the wave propagation. If the velocity increases with depth, the refraction of the waves helps with obtaining more angles. The window operator in the Marchenko algorithm plays a fundamental role in the scheme. At the very far angles, the window operator starts intersecting the downgoing Green's function causing a partial removal of the Green's function. Because the MDD approach uses all the downgoing Green's functions instead of only the center one, the lack of the far offset retrieval affects the offset at which the reflectivity can be obtained.

The multidimensional deconvolution (MDD), which was used to resolve the redatumed reflection response, is an inversion process that can be unstable. This inverse problem is fundamentally ill-posed, and it has to be stabilized to be successfully solved. In the numerical examples, the source and receivers used were dense and well-spaced. In practice, the acquisition geometry is sparse and can be irregular, which remarkably contributes to the instability of the MDD method such that it becomes more problematic to obtain a correct solution to the inverse problem.

Bibliography

- Aki, K. and Richards, P. G. (1980). *Quantitative seismology: Theory and methods*. *W.H. Freeman and Co*, 1.
- Avseth, P., Mukerji, T., and Mavko, G. (2005). *Quantitative Seismic Interpretation*. Cambridge University Press, Cambridge, UK.
- Bacon, M. and Simm, R. (2014). *Seismic Amplitude: An Interpreter's Handbook*. Cambridge University Press, Cambridge, UK.
- Berkhout, A. J. (1985). *Seismic migration: Imaging of acoustic energy by wave field extrapolation. A. Theoretical aspects*. Elsevier Science.
- Berkhout, A. J. and Wapenaar, C. P. A. (1989). One-way versions of the Kirchhoff integral. *Geophysics*, 54:460–467.
- Bortfeld, R. (1961). Approximation to the reflection and transmission coefficients of plane longitudinal and transverse waves. *Geophysical Prospecting*, 9:485–502.
- Broggini, F. and Snieder, R. (2012). Connection of scattering principles: A visual and mathematical tour. *European Journal of Physics*, 33(3):593–613.
- Cambois, G. (2000). Can P-wave AVO be quantitative? *Leading Edge (Tulsa, OK)*, 19(11):1246–1251.
- Castagna, J. P. and Backus, M. M. (1993). *Offset-Dependent Reflectivity - Theory and Practice of AVO Analysis*. Society of Exploration Geophysicists, Tulsa.
- Chopra, S., Castagna, J. P. (2014). *No Title*. Society of Exploration Geophysicists, Tulsa, Oklahoma.
- Claerbout, J. F. (1971). Toward a Unified Theory of Reflector Mapping. *Geophysics*, 36(3):467–481.
- Claerbout, J. F. (1978). *Fundamentals of geophysical data processing: With applications to petroleum prospecting*, volume 15. Blackwell Scientific Publications, New York.
- Cohen, J. K. and Stockwell, J. W. (2016). CWP/SU: Seismic Un*x Release No. 43R4: An open source software package for seismic research and processing.

- De Bruin, C. (1992). *Linear avo inversion by prestack depth migration: Imaging angle dependent reflectivity as a tool for litho-stratigraphic inversion*. PhD thesis, Delft University of Technology.
- De Bruin, C. G., Wapenaar, C. P., and Berkhout, A. J. (1990). Angle-dependent reflectivity by means of prestack migration. *Geophysics*, 55(9):1223–1234.
- Dukalski, M., Mariani, E., and de Vos, K. (2018). Short Period Internal De-multiple Using Energy and Causality Constrained Bandlimited Marchenko Redatuming. In *88th Annual International Conference and Exhibition, EAGE*, London, The United Kingdom.
- Fink, M., Cassereau, D., Arnaud, D., Prada, C., Roux, P., Tanter, M., Thomas, J.-L., and Wu, F. (2000). Time-reversed acoustics. *Reports On Progress In Physics*, 63:1933–1995.
- Hatchell, P. J. (2000). Fault whispers: Transmission distortions on prestack seismic reflection data. *Geophysics*, 65(2):377–389.
- Mildner, C., Dukalski, M., Elison, P., De Vos, K., Brogгинi, F., and Robertsson, J. (2019). True Amplitude-Versus-Offset Green’s Function Retrieval Using Augmented Marchenko Focusing. In *81st EAGE Conference Exhibition 2019*, London, The United Kingdom.
- Minato, S., Matsuoka, T., and Tsuji, T. (2013). Singular-value decomposition analysis of source illumination in seismic interferometry by multidimensional deconvolution. *GEOPHYSICS*, 78(3):Q25–Q34.
- Morse, P. and Feshbach, H. (1953). *Methods of theoretical physics*. McGraw-Hill Book Company, Inc.
- Shuey, R. T. (1985). Simplification of the Zoeppritz Equations. *Geophysics*, 50(4):609–614.
- Slob, E., Wapenaar, K., Brogгинi, F., and Snieder, R. (2014). Seismic reflector imaging using internal multiples with Marchenko-type equations. *Geophysics*, 79(2):S63–S76.
- Thorbecke, J. (2017). GitHub repository of Source code.
- Thorbecke, J. and Draganov, D. (2010). Finite-difference modeling experiments for seismic interferometry. *Society of Exploration Geophysicists International Exposition and 80th Annual Meeting 2010, SEG 2010*, 76(6):4013–4018.
- Thorbecke, J., Slob, E., Brackenhoff, J., van der Neut, J., and Wapenaar, K. (2017). Implementation of the marchenko method. *Geophysics*, 82(6):WB29–WB45.
- van der Neut, J., Vasconcelos, I., and Wapenaar, K. (2015). On Green’s function retrieval by iterative substitution of the coupled Marchenko equations. *Geophysical Journal International*, 203(2):792–813.
- Van Der Neut, J., Wapenaar, K., Thorbecke, J., and Vasconcelos, I. (2014). Marchenko redatuming below a complex overburden. In *2nd International KAUST-KACST-JCCP Workshop on Surface and Subsurface 4D Monitoring*, number March, pages 4–6, King Abdullah University of Science and Technology (KAUST), Saudi Arabia.
- Wapenaar, C. P. A. and Berkhout, A. J. (1989). *Elastic Wave Field Extrapolation: Redatuming of Single- and Multi-Component Seismic Data*. Elsevier Science, Amsterdam.

- Wapenaar, K., Ruigrok, E., van der Neut, J., Draganov, D., Hunziker, J., Slob, E., Thorbecke, J., and Snieder, R. (2010). *Green's function representation for seismic interferometry by deconvolution*, pages 3972–3978.
- Wapenaar, K., Thorbecke, J., van der Neut, J., Brogini, F., Slob, E., and Snieder, R. (2014a). Green's function retrieval from reflection data, in absence of a receiver at the virtual source position. *The Journal of the Acoustical Society of America*, 135(5):2847–2861.
- Wapenaar, K., Thorbecke, J., Van der Neut, J., Brogini, F., Slob, E., and Snieder, R. (2014b). Marchenko imaging. *Geophysics*, 79(3):WA39–WA57.
- Yilmaz, O. (2001). *Seismic Data Analysis: Processing, Inversion, and Interpretation of Seismic Data*. Society of Exploration Geophysicists, Tulsa, Oklahoma, second edition.
- Yu, G. (1985). Offset-amplitude variation and controlled-amplitude processing. *Geophysics*, 50:2697–2708.
- Zhang, L., Thorbecke, J., Wapenaar, K., and Slob, E. (2019). Data-driven internal multiple elimination and its consequences for imaging: A comparison of strategies. *Geophysics*, 84(5):S365–S372.
- Zoeppritz, K. (1919). VII b. Über Reflexion und Durchgang seismischer Wellen durch Unstetigkeitsflächen [VIIb. On reflection and transmission of seismic waves by surfaces of discontinuity],. *Nachrichten von der Gesellschaft der Wissenschaften zu Göttingen, Mathematisch-Physikalische Klasse*, pages 66–84.

Appendix A

Derivation

A-1 Derivation of the Shuey approximation in acoustic media

The 3-term Shuey equation can be written as (Avseth et al., 2005)

$$A(\theta) = A_0 + G \sin^2 \theta + B (\tan^2 \theta - \sin^2 \theta), \quad (\text{A-1})$$

with

$$A_0 = \frac{1}{2} \left(\frac{\Delta c}{\bar{c}} + \frac{\Delta \rho}{\bar{\rho}} \right), \quad (\text{A-2})$$

$$G = \frac{1}{2} \frac{\Delta c}{\bar{c}} - 2 \frac{\Delta c_s^2}{\Delta c^2} \left(2 \frac{\Delta c_s}{\bar{c}_s} + \frac{\Delta \rho}{\bar{\rho}} \right), \quad (\text{A-3})$$

$$B = \frac{1}{2} \frac{\Delta c}{\bar{c}}, \quad (\text{A-4})$$

where A is the reflection amplitude coefficient at a certain angle of incidence θ , A_0 is the zero-incidence reflection amplitude coefficient, also known as the intercept, B is the gradient that describes how A varies with θ , Δc and Δc_s are the differences of compressional and shear velocities across the boundary, respectively, $\Delta \rho$ is the difference of density across the boundary, \bar{c} and \bar{c}_s are the average compressional and shear velocities across the boundary, respectively, and $\bar{\rho}$ is the average density across the boundary. Assuming acoustic media, the shear velocity becomes zero. As a result,

$$G = \frac{1}{2} \frac{\Delta c}{\bar{c}} = B. \quad (\text{A-5})$$

By substituting Equation A-5 into Equation A-1, the Shuey approximation in acoustic media is obtained as follows

$$A(\theta) = A_0 + B \tan^2 \theta. \quad (\text{A-6})$$

Appendix B

Monopole-to-dipole conversion

The estimated Green's functions $G^{-,+}(\mathbf{x}''_0, \mathbf{x}'_i, t)$ and $G^{-,-}(\mathbf{x}''_0, \mathbf{x}'_i, t)$ will behave with a monopole signature since the direct arrival $G_d(\mathbf{x}''_0, \mathbf{x}'_i, t)$ is modeled with a monopole source. In order to have a redatumed reflection response $R(\mathbf{x}_i, \mathbf{x}'_i, t)$ as if there is a dipole source at \mathbf{x}'_i , a monopole-to-dipole conversion has to be applied, according to

$$\hat{P}_2^{-,+}(\mathbf{x}''_0, \mathbf{x}'_i, \omega) = \frac{2}{j\omega\rho} \partial_z \hat{P}_1^{-,+}(\mathbf{x}''_0, \mathbf{x}'_i, \omega) |_{z=z_i}, \quad (\text{B-1a})$$

$$\hat{P}_2^{-,-}(\mathbf{x}''_0, \mathbf{x}'_i, \omega) = \frac{2}{j\omega\rho} \partial_z \hat{P}_1^{-,-}(\mathbf{x}''_0, \mathbf{x}'_i, \omega) |_{z=z_i}, \quad (\text{B-1b})$$

where $\hat{P}_2(\mathbf{x}''_0, \mathbf{x}'_i, \omega)$ is the wavefield with a dipole signature,

$$\hat{P}_1^{-,+}(\mathbf{x}''_0, \mathbf{x}'_i, \omega) = \hat{G}^{-,+}(\mathbf{x}''_0, \mathbf{x}'_i, \omega) \hat{S}(\omega), \quad (\text{B-2a})$$

$$\hat{P}_1^{-,-}(\mathbf{x}''_0, \mathbf{x}'_i, \omega) = \hat{G}^{-,-}(\mathbf{x}''_0, \mathbf{x}'_i, \omega) \hat{S}(\omega), \quad (\text{B-2b})$$

with $\hat{S}(\omega)$ as the source signature, and ρ is the local density. The conversion can be sufficiently carried out in the wavenumber-frequency domain by applying the rule $\partial_z \rightarrow jk_z$ for a source radiating downward:

$$\tilde{P}_2^{-,+}(k_x, z_i, \omega) = \frac{2k_z}{\omega\rho} \tilde{P}_1^{-,+}(k_x, z_i, \omega), \quad (\text{B-3a})$$

$$\tilde{P}_2^{-,-}(k_x, z_i, \omega) = \frac{2k_z}{\omega\rho} \tilde{P}_1^{-,-}(k_x, z_i, \omega), \quad (\text{B-3b})$$

where k_z is the vertical wavenumber given by

$$k_z = \sqrt{\frac{\omega^2}{c^2} - k_x^2}, \quad (\text{B-4})$$

with c as the local velocity and k_x as the horizontal wavenumber (Equation 3-6a).

Appendix C

Deconvolution and stabilization

The deconvolution process can produce unstable results that require stabilization before estimating the reflectivity. Here, the process is demonstrated step by step using the spectral division (Equation 2-38). Similar steps can also be implemented for the MDD (Equation 2-36). The example in section 4-1 is considered with a focal level located at $z_i = 1100$ m. Figure C-1 shows the result after applying deconvolution and mapping into the angle-frequency domain. Note the artifacts in the very low frequencies (below approximately 7 Hz) and very high frequencies (above approximately 100 Hz), see Figure C-1B. Moreover, there are other artifacts at the very far angles, see Figure C-1A. All of these artifacts are due to the very small values outside the bandwidth of the signal. Division by these very small values produces a very large noisy spectrum that contaminates the whole signal. The problem can be reduced either by filtering or by adding a small positive non-zero constant ϵ to the denominator (see Equation 2-38). Also, the two methods can be combined to solve the problem. First, the problem is stabilized by trying different values of ϵ . Figure C-2 shows the result after adding a value of $\epsilon = 10^{-5}$. Note that the high frequencies and the artifacts at the very far angles are reduced notably without affecting the other frequencies. However, the very low frequencies are still amplified. In order to stabilize the very low frequencies, the value of ϵ has to be increased. Figure C-3 shows the result after increasing the constant to $\epsilon = 10^{-4}$. In this case, the very high frequencies are reduced even further, and the very low frequencies are also reduced to some extent. However, it can be seen that the other frequencies are affected slightly, see Figure C-3B. This will affect the estimation of the angle-dependent reflectivity. Alternatively, the problem should be stabilized first by applying tapering in both frequency and angle domains. This can be done by defining a band-pass filter in both domains, see Figure C-4. Beyond the limits of the filter, a sinusoidal taper is applied, see Figure C-5. Note that the very low frequencies and very high frequencies are stabilized without affecting the other frequencies. There are still some small artifacts at the very far angles which could not be reduced by the filter. However, these small artifacts can be reduced by applying a small value of $\epsilon = 10^{-6}$, see Figure C-6. It can be seen that the small artifacts are eliminated without causing any impact on the other frequencies. This solution is considered to be suitable for estimating angle-dependent reflectivity.

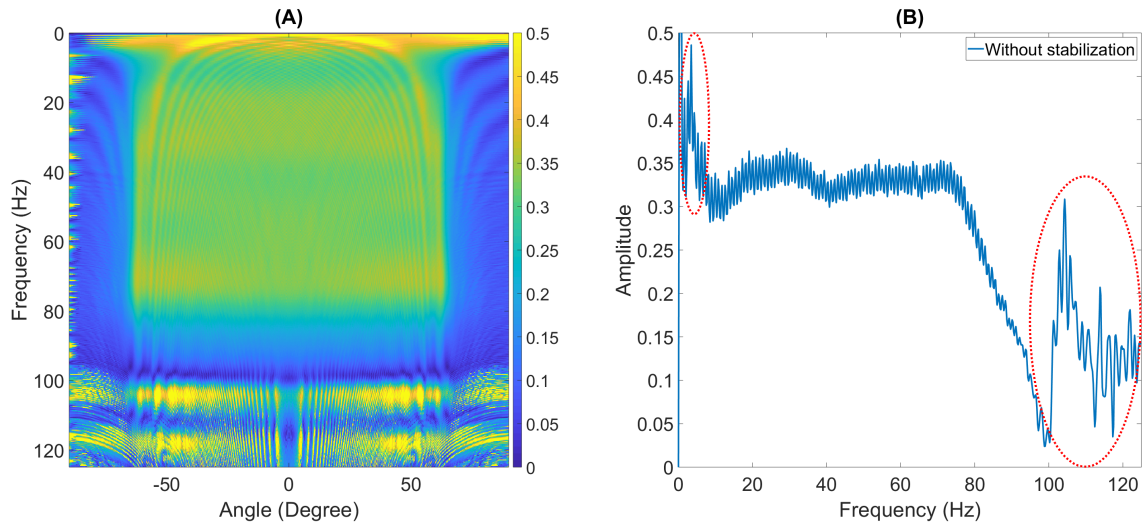


Figure C-1: The result of the deconvolution process before applying stabilization. (A) The redatumed reflection response after mapping into the angle-frequency domain. Note the artifacts at the very low frequency and very high frequency. Also, there are artifacts at the very far angles (at the left edge of the panel). (B) The frequency domain for $\theta = 0$. The dotted red ellipses highlight the artifacts.

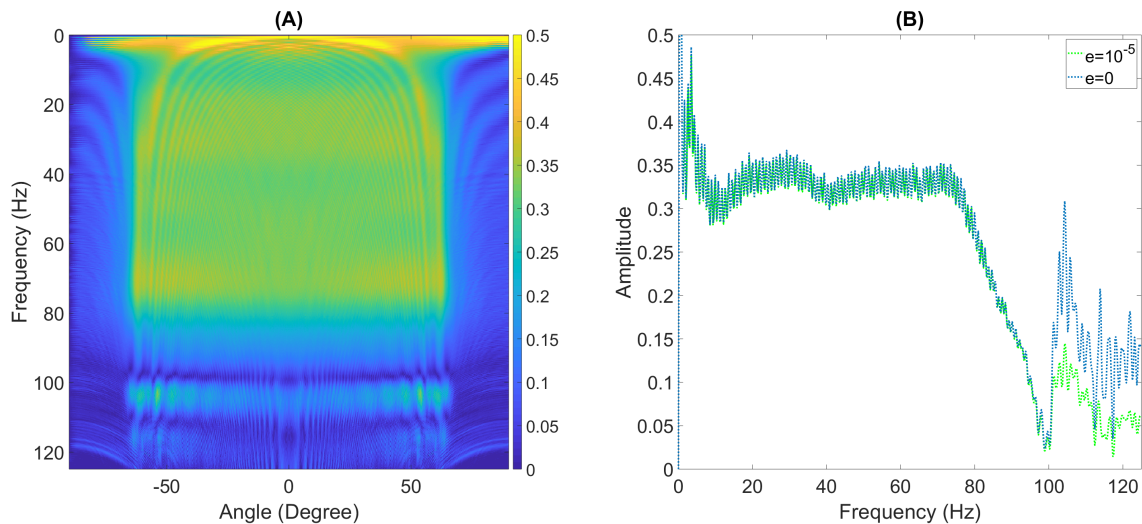


Figure C-2: The impact of the stabilization parameter ϵ on the deconvolution result. (A) The redatumed reflection response after applying stabilization using $\epsilon = 10^{-5}$. Note the artifacts are reduced notably except the very low frequency. (B) The frequency domain for $\theta = 0$ before and after adding ϵ . Note the impact on the high frequencies.

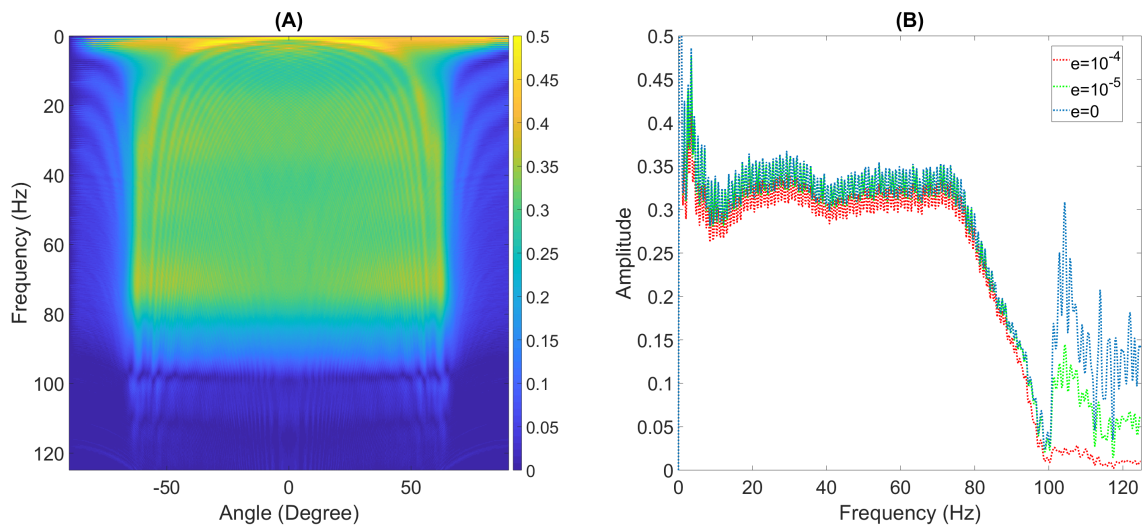


Figure C-3: The impact of using a larger value of e on the deconvolution result. (A) The redatumed reflection after applying stabilization using $e = 10^{-4}$. Note the the very high frequency are reduced significantly and the very low frequency are also reduced to some extent. (B) The frequency domain for $\theta = 0$ after increasing e . Note that the other frequencies (7Hz to 80Hz) have slightly decreased.

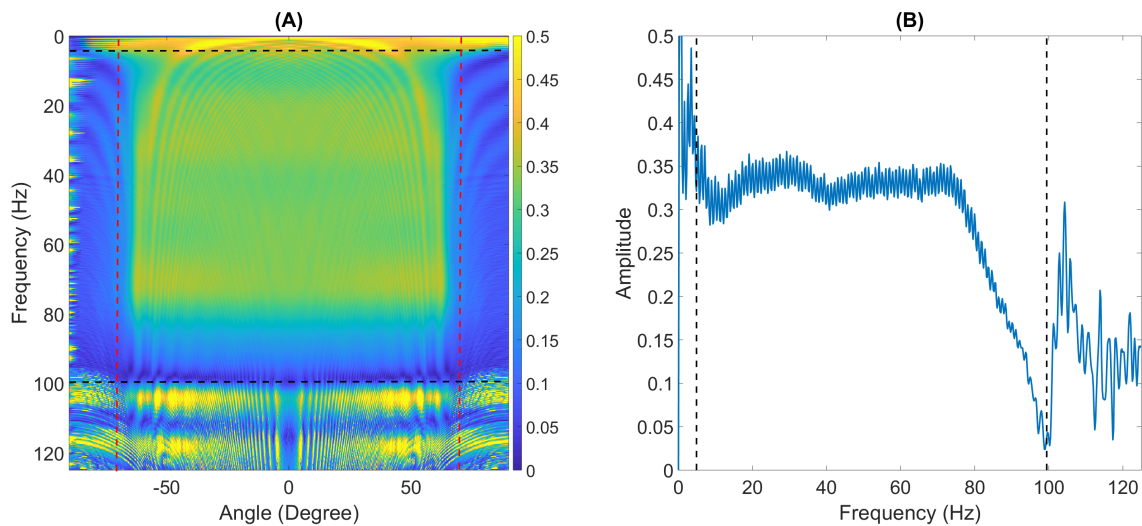


Figure C-4: Defining the limits of the band-pass filter. (A) The redatumed reflection response in the angle-frequency domain with no stabilization. The horizontal black dashed lines represent the limits of the band-pass filter in the frequency domain while the vertical red dashed lines indicate the limits of the band-pass filter in the angle domain. (B) The frequency domain for $\theta = 0$. The vertical black dashed lines represent the limits of the band-pass filter.

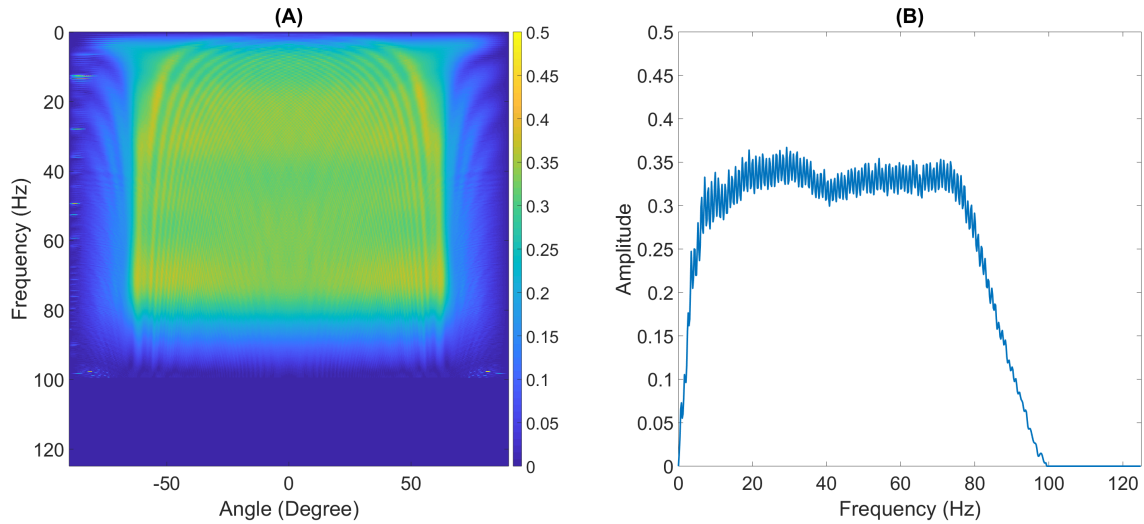


Figure C-5: The impact of the band-pass filter. (A) The redatumed reflection response after applying the band-pass filter. Note that the artifacts in both low and high frequencies are eliminated except small artifacts in the far angles. (B) The frequency domain for $\theta = 0$ after applying the band-pass filter.

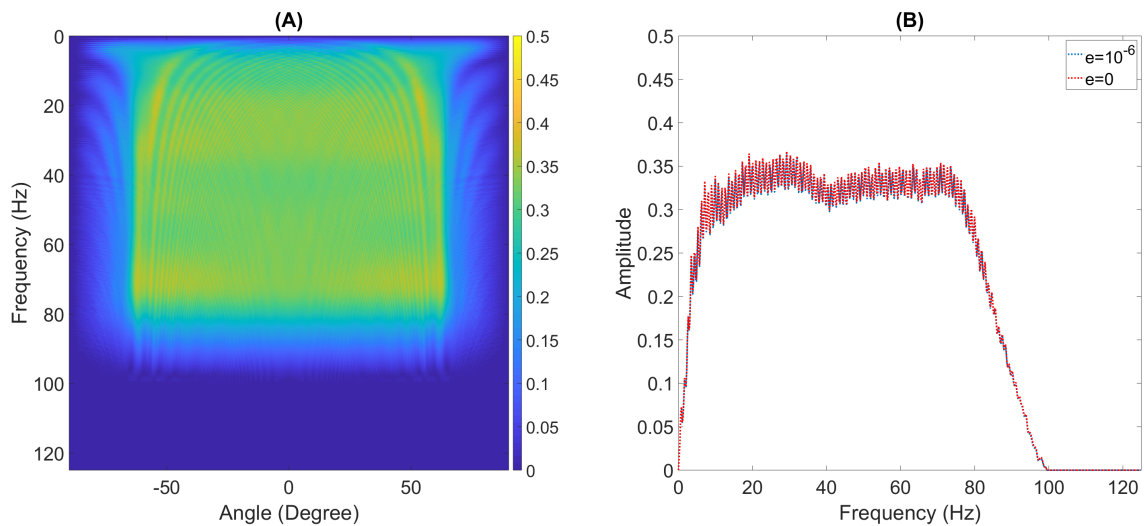


Figure C-6: The impact of combining the stabilization parameter e and filtering. (A) The redatumed reflection response after applying e and filtering. Note that the small artifacts in Figure C-5A are removed after adding $e = 10^{-6}$. (B) The frequency domain for $\theta = 0$. Note that the other frequencies are not affected by the stabilization parameter e .

Appendix D

Amplitude picking procedure

The amplitude picking procedure is applied after obtaining the image of the angle-dependent reflectivity. This can be done using the functions `envelope` and `max` in Matlab (or any similar functions in other programming languages). [Figure D-1A](#) shows an image of a reflector located at 400 m with $c_1 = 1800$ m/s, $c_2 = 2300$ m/s, $\rho_1 = 1000$ kg/m³, and $\rho_2 = 3000$ kg/m³. The envelope is estimated for every depth level as shown in [Figure D-1B](#). After that, the envelope with the maximum amplitude is considered for the reflectivity. Compared to the exact reflectivity, see [Figure D-1C](#), it can be seen that the reflectivity is estimated correctly up to the critical angle. The procedure can also be applied when the image contains downward curvature (i.e. non-flat event) due to estimating the direct arrival from a wrong velocity model, see [Figure D-2](#).

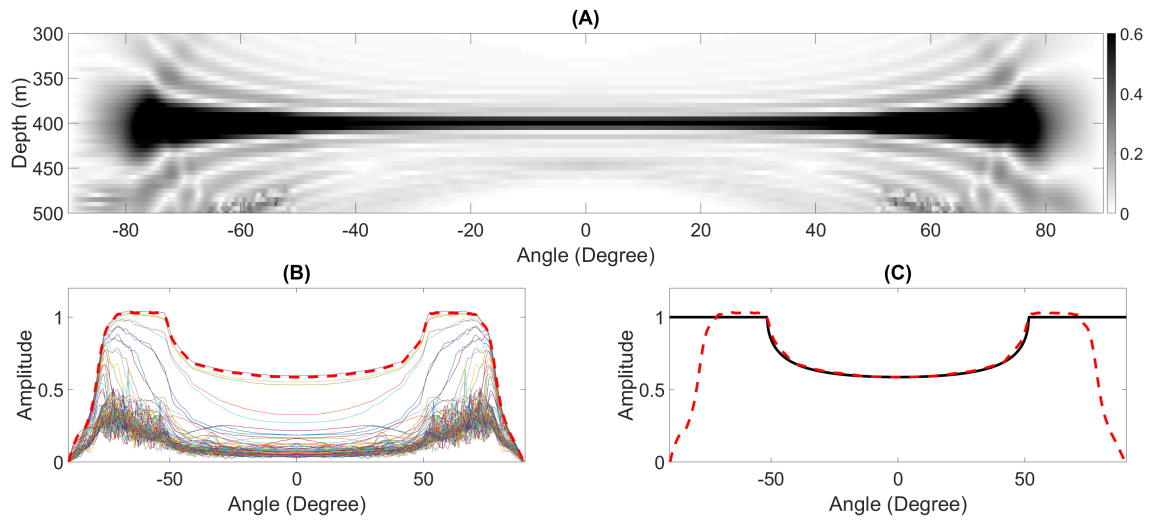


Figure D-1: Amplitude picking procedure on a flat event, with $c_1 = 1800$ m/s, $c_2 = 2300$ m/s, $\rho_1 = 1000$ kg/m³, and $\rho_2 = 3000$ kg/m³. (A) Image of the reflector (modulus). (B) The envelope for every depth level (solid thin curves with different colors) and maximum envelope (red dashed curve). The maximum envelope represents the modulus of the angle-dependent reflectivity. (C) Plotting the maximum envelope with the exact reflectivity.

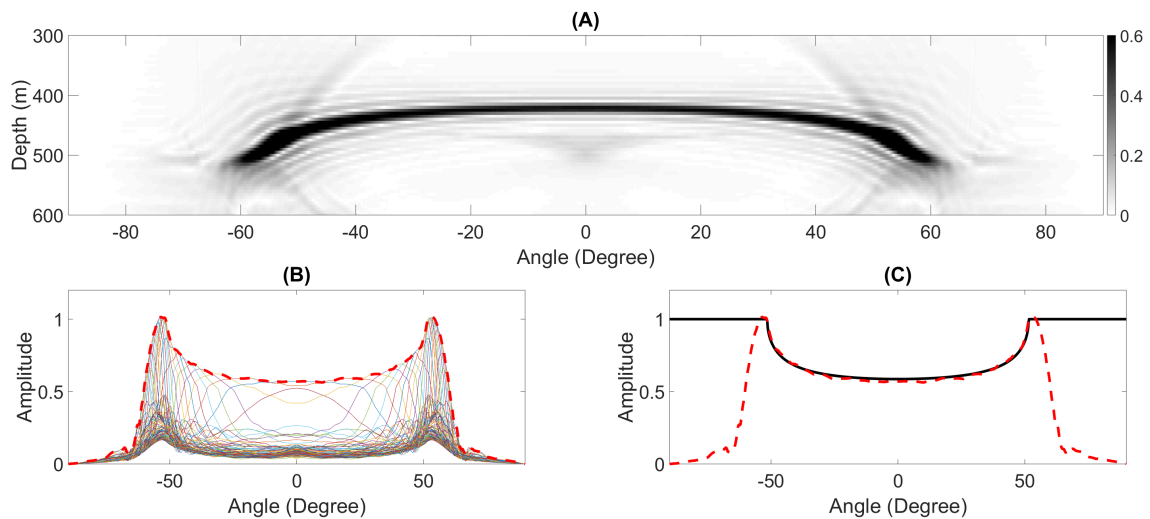


Figure D-2: Amplitude picking procedure on a non-flat event, with $c_1 = 1800$ m/s, $c_2 = 2300$ m/s, $\rho_1 = 1000$ kg/m³, and $\rho_2 = 3000$ kg/m³. (A) Image of the reflector (modulus). (B) The envelope for every depth level (solid thin curves with different colors) and maximum envelope (red dashed curve). The maximum envelope represents the modulus of the angle-dependent reflectivity. (C) Plotting the maximum envelope with the exact reflectivity.

Appendix E

Matlab scripts

E-1 1D Marchenko

E-1-1 Marchenko redatuming in 1D

Forward modelling

```
function [T,R]=layerc(cp,rho,dz,nt,dt,np,dp,p0,norm,mul)           1
% LAYERCODE    Compute the response of
%              an 1D acoustic medium
%
% syntax: [T,R]=layercode(Cp,Rho,dz,nt,dt,np,dp,p0,norm)
%
% R = Reflection response (t,p)
% T = Transmission response (t,p)
%
% Cp    = Velocity log                                           11
% Rho   = Density log
% dz    = depth step
% nt    = number of time samples
% dt    = time sampling
% np    = number of rayparameters                                 16
% dp    = rayparameter sampling
% p0    = first rayparameter
% norm  = 0: flux normalization; 1: pressure normalization
% mul   = 0: no multiples; 1: multiples                           21
%

%number of layers
%-----
if length(cp)~=length(rho)                                     26
    disp('WARNING: discrepancy between density and velocity log');
    disp(' Smallest is chosen!');
end;
N = min([length(cp) length(rho)]);                             31

%frequencies
%-----
om = (0:(nt/2)).*(2*pi/(nt*dt));
om = om.';
nf = (nt/2)+1;
p  = (0:np-1).*dp + p0;                                         36

%initialise the GLOBAL quantities
%-----
Rd = zeros(nf,np); % Upgoing Reflection response                41
Ru = zeros(nf,np); % Downgoing Reflection response
Td = ones(nf,np); % Downgoing Transmission response
Tu = ones(nf,np); % Upgoing Transmission response
T2 = ones(nf,np); % Two-way Transmission response ????
```

```

%start the recursion loop over the N-1 layers
for n=1:N-1
%   if 10*round(n/10) == n
%       fprintf('n = %g\n',n)
%   end
%calculate the local operators
%-vertical slowness- (number of layers (N), number of p(np))
q1 = sqrt(cp(n).^(-2)-p.^2);
q2 = sqrt(cp(n+1).^(-2)-p.^2);
%-reflection coefficients- and
%-flux normalised transmission coefficients-
r = (rho(n+1).*q1-rho(n).*q2)./(rho(n+1).*q1+rho(n).*q2);
if norm == 0
td = sqrt(rho(n+1).*q1.*rho(n).*q2)./(0.5.*(rho(n+1).*q1+rho(n).*q2));
tu = td;
else
td = 1 + r;
tu = 1 - r;
end
if mul==0
td=1;
tu=1;
end
t2 = tu.*td;
% calculate the phase shift operator
q = ones(nf,1)*q1;
q = real(q) + 1i*(sign(real(om))*ones(1,np)).*imag(q);
r = ones(nf,1)*r;
td = ones(nf,1)*td;
tu = ones(nf,1)*tu;
t2 = ones(nf,1)*t2;
om1 = om*ones(1,np);
w = exp(1i*om1.*q*dz);
w2 = w.^2;
%calculate the multiple operator
if mul == 1
M = (1-w2.*r.*Ru).^(-1);
else
M = 1;
end
%calculate the R downgoing
Rd = Rd + T2.*w2.*r.*M;
%calculate the R upgoing
Ru = -r + t2.*w2.*Ru.*M;
%calculate the T downgoing
Td = td.*w.*Td.*M;
%calculate the T upgoing
Tu = tu.*w.*Tu.*M;
%calculate the T square
T2 = Td.*Tu;
end
%calculate the inverse fft's
T = [Td(1:nt/2,:) ;real(Td(nt/2+1,:)) ;conj(Td(nt/2:-1:2,:))];
T = real(ifft(conj(T)));
R = [Rd(1:nt/2,:) ;real(Rd(nt/2+1,:)) ;conj(Rd(nt/2:-1:2,:))];
R = real(ifft(conj(R)));

```

Ricker wavelet

```

function s=rickerJ(npts,freq,dt,nsw)
% Function ricker.m computes a symmetric Ricker wavelet of predominant
% frequency freq. The number of points in the wavelet is npts. The
% sampling interval is dt (be sure npts and dt are large enough to
% adequately represent the entire wavelet). Be sure dt is small enough
% to avoid aliasing. nsw is the number of points on each end of the
% wavelet for applying a taper to smooth any possible edge effects of the
% wavelet. In general, to determine dt and npts for a given frequency:
% dt >= 1/(10*freq); npts ~ (3/freq)/dt
% The wavelet is shifted by half the wavelet length so that the travel
% times for reflections are located at the center of the wavelet.
timesh=npts*dt/2;
pi2=sqrt(pi)/2;
b=sqrt(6)/(pi*freq);

```

```

const=2*sqrt(6)/b;
s=zeros(npts,1);
for i=1:npts
    tim1=(i-1)*dt;
    tim2=tim1-timesh;
    u=const*tim2;
    amp=((u^2)/4)-(0.5)*pi2*(exp(-u^2/4));
    s(i)=amp;
end
sm=max(abs(s));
s=s/sm;
if nsw>0
    for i=1:nsw
        j=nsw-i;
        fac=0.5*(cos((pi*j)/nsw)+1);
        s(i)=s(i)*fac;
    end
    for i=1:nsw
        j=i-1;
        fac=0.5*(cos((pi*j)/nsw)+1);
        k=npts-nsw+i;
        s(k)=s(k)*fac;
    end
end
end

```

1D Marchenko

```

function [Gp,Gm,f1p,f1m,f2p,f2m,a] = Marchenko(x,k,R,Rs,T,P,Pd,Dw,D0w,td,dt)
% Preparation for the scheme
FFC = @(x) ifft(conj(fft(x)));
Om = @(x) T.*Rs(T.*R(x));
Oms = @(x) T.*R(T.*Rs(x));
Gp = zeros(length(x),k+1);
Gm = Gp;
f1p = Gm;
f1m = f1p;
f2p = f1m;
f2m = f2p;
% Determine the scaling factor for the first arrival
z = Dw;
xi = -Pd.*R(T.*Rs(Dw));
for n1=1:k
    z = Oms(z);
    xi = xi - Pd.*R(T.*Rs(z));
end
xi = circshift(xi,-round(td/dt));
xi = ifft(fft(D0w) + fft(xi));
a = sqrt(max(D0w)/max(xi));
scale the first arrival
% Start the Marchenko scheme
Gm(:,1) = P.*R(x);
events
Gp(:,1) = FFC(x);
f1p(:,1) = x;
f1m(:,1) = T.*R(x);
f2p(:,1) = -FFC(f1m(:,1));
f2m(:,1) = f1p(:,1);
y = x;
x1 = x;
for n=1:k
    Gp(:,n+1) = FFC(x1 - P.*Rs(T.*R(y)));
    x = Om(x);
    y = y + x;
    Gm(:,n+1) = P.*R(y);
    f1p(:,n+1) = y;
    f1m(:,n+1) = T.*R(y);
    f2p(:,n+1) = -FFC(f1m(:,n+1));
    function
    f2m(:,n+1) = f1p(:,n+1);
end
end

```

E-2 Imaging angle-dependent reflectivity

E-2-1 Mapping the wavenumber into the angle domain

```

function [df,faxis,dk,kaxis,datafk,dataftheta,m,re,im] = kx2theta(data,nx,dx,nt,dt,c1,c2,rho1,rho2)

```

```

% This program maps the horizontal wavenumber into angle in
% the wavenumber-frequency domain using linear interpolation. The program
% also estimates the angle-dependent reflectivity and compares the results
% to the exact ones.
6

% For theory, the user can refer to De Bruin, C. G., Wapenaar, C. P., and Berkhout, A.
% J. (1990). Angle-dependent reflectivity by means of prestack migration.
% Geophysics, 55(9): 1223-1234.
11

% Note: the program is designed for a 2D medium (x-z) only. Also, the
% results may need stabilization before estimating the reflectivity
16

%% Inputs
% data: input data in the space-time domain
% nx: number of samples in the space domain
% dx: spatial sampling in m
% nt: number of samples in the time domain
% dt: temporal sampling in s
% c1: velocity of the upper layer in m/s
% c2: velocity of the lower layer in m/s
% rho1: density of the upper layer in kg/m3
% rho2: density of the lower layer in kg/m3
21

%% Outputs
% df: frequency sampling
% faxis: frequency axis
% dk: wavenumber sampling
% kaxis: wavenumber axis
% datafk: data in wavenumber-frequency domain
% dataftheta: data in angle-frequency domain
% m: Moduli
% re: real part
% im: imaginary part
26

%% The Program starts from this line
41

% Estimate the frequency sampling in Hz
df = 1/(nt*dt);
46

% Generate the frequency axis in Hz
faxis = 0:df:(nt-1)*df;
46

% Estimate the spatial sampling in the wavenumber-frequency domain in 1/m
dk = 2*pi/(nx*dx);
51

% Generate the wavenumber axis in 1/m
kaxis = zeros(1, nx);
kaxis(1:(nx-1)/2+1) = -((nx-1)/2)*dk:dk:0;
kaxis((nx-1)/2+2:end) = dk:dk:((nx-1)/2)*dk;
56

% Apply 2D Fourier transform
datafk = fftshift(fft2(data), 2)*dx*dt*2;
61

% Find the size of the datafk
[v h] = size(datafk);

% Estimate the angular frequency
omega = faxis*2*pi;
66

% Initiate the matrix of the angle of incidence
theta = zeros(v, h);
71

% Generate the angle axis using a linear spacing with nx
phi = linspace(-90, 90, nx);
76

% Estimate the angle of incidence for every frequency
for i = 1:v/2
    theta(i, :) = asind(c1*kaxis/omega(i));
81
end

% Map kx into theta using positive frequency only
86

for i = 2:v/2
    % Select real part
    X = real(theta(i, :));
91

```

```

% Select frequency contributions
V = datafk(i,:);

% Exclude repeated angle.
[x, index] = unique(X);

dataftheta(i,:) = 2*interp1(X(index),V(index),phi,'linear','extrap');

end

% Estimate the modulus of the reflectivity
m=abs(sum(dataftheta)/nt);

% Estimate the real part of the reflectivity
re=real(sum(dataftheta)/nt);

% Estimate the imaginary part of the reflectivity
im=imag(sum(dataftheta)/nt);

% Estimate the exact reflectivity
for j=1:length(phi)
R(j) = abs((rho2*c2*cosd(phi(j))-rho1*sqrt(c1^2-c2^2*sind(phi(j))^2))/(rho2*c2*cosd(phi(j))+rho1*sqrt(c1^2-c2^2*sind(phi(j))^2)));
end

figure

subplot(1,3,1)
imagesc(kaxis, faxis, abs(datafk))
xlabel('Wavenumber (1/m)', 'FontSize', 18)
ylabel('frequency (Hz)', 'FontSize', 18)
title('Wavenumber-frequency (Modulus)')
xlim([min(kaxis) max(kaxis)])
ylim([0 max(faxis(1:v/2))])
ax = gca;
ax.FontSize = 25;

subplot(1,3,2)
imagesc(phi, faxis(1:v/2), abs(dataftheta))
xlabel('Angle (Degree)', 'FontSize', 18)
ylabel('frequency (Hz)', 'FontSize', 18)
title('Angle-frequency (Modulus)')
xlim([-90 90])
ylim([0 max(faxis(1:v/2))])
ax = gca;
ax.FontSize = 25;

subplot(1,3,3)
plot(phi,R,'k','linewidth',5)
hold on
plot(phi,m,'r','linewidth',5)
xlabel('Angle (Degree)', 'FontSize', 18)
ylabel('Amplitude', 'FontSize', 18)
xlim([-90 90])
title('Modulus as function of ray parameter')
ylim([0 1.2])
ax = gca;
ax.FontSize = 25;

end

```

E-2-2 Mapping the wavenumber into the ray parameter domain

```

function [df, faxis, dk, kaxis, datafk, paxis, datafp, m, re, im] = kx2p(data, nx, dx, nt, dt, c1, c2, rho1, rho2, vmin)

% This program maps the horizontal wavenumber into ray parameter (slowness) in
% the wavenumber-frequency domain using linear interpolation. The program
% also estimates the angle-dependent reflectivity and compares the results
% to the exact ones.

% For theory, the user can refer to De Bruin, C. G., Wapenaar, C. P., and Berkhout, A.
% J. (1990). Angle-dependent reflectivity by means of prestack migration.
% Geophysics, 55(9): 1223-1234.

% Note: the program is designed for a 2D medium (x-z) only. Also, the
% results may need stabilization before estimating the reflectivity

%% Inputs

```

```

% data: input data in the space-time domain
% nx: number of samples in the space domain
% dx: spatial sampling in m
% nt: number of samples in the time domain
% dt: temporal sampling in s
% c1: velocity of the upper layer in m/s
% c2: velocity of the lower layer in m/s
% rho1: density of the upper layer in kg/m3
% rho2: density of the lower layer in kg/m3
% vmin: minimum velocity in the data

%% Outputs
% df: frequency sampling
% faxis: frequency axis
% dk: wavenumber sampling
% kaxis: wavenumber axis
% datafk: data in wavenumber-frequency domain
% paxis: ray parameter axis
% datafp: data in ray parameter-frequency domain
% m: Moduli
% re: real part
% im: imaginary part

%% The Program starts from this line

% Estimate the frequency sampling in Hz
df = 1/(nt*dt);

% Generate the frequency axis in Hz
faxis = 0:df:(nt-1)*df;

% Estimate the spatial sampling in the wavenumber-frequency domain in 1/m
dk=2*pi/(nx*dx);

% Generate the wavenumber axis in 1/m
kaxis=zeros(1,nx);
kaxis(1:(nx-1)/2+1)=-((nx-1)/2)*dk:dk:0;
kaxis((nx-1)/2+2:end)=dk:dk:((nx-1)/2)*dk;

% Apply 2D Fourier transform
datafk=fftshift(fft2(data),2)*dx*dt*2;

% Find the size of the datafk
[v h] = size(datafk);

% Estimate the angular frequency
omega = faxis*2*pi;

% Compute the ray parameter domain
pmin=0;
pmax=1/vmin;
dp = (pmax-pmin)/(500);
paxis=-pmax:dp:pmax;

for i=2:nt/2
    p(i,:)=kaxis/omega(i);
end
for i=2:nt/2
    X = (p(i,:));
    V = datafk(i,:);
    [x, index] = unique(X);
    datafp(i,:) = 2*interp1(X(index),V(index),paxis,'linear','extrap');
end

% Estimate the modulus of the reflectivity
m=abs(sum(datafp)/nt);

% Estimate the real part of the reflectivity
re=real(sum(datafp)/nt);

% Estimate the imaginary part of the reflectivity
im=imag(sum(datafp)/nt);

```

```

% Estimate the exact reflectivity
for j=1:length(paxis)
R(j) = abs((rho2*sqrt((1/c1)^2-paxis(j)^2)-rho1*sqrt((1/c2)^2-paxis(j)^2))/(rho2*sqrt((1/c1)^2-paxis(j)^2)+rho1*sqrt((1/c2)^2-paxis(j)^2)));
end

figure

subplot(1,3,1)
imagesc(kaxis, faxis, abs(datafk))
xlabel('Wavenumber (1/m)', 'FontSize', 18)
ylabel('frequency (Hz)', 'FontSize', 18)
title('Wavenumber-frequency (Modulus)')
xlim([min(kaxis) max(kaxis)])
ylim([0 max(faxis(1:v/2))])
ax = gca;
ax.FontSize = 25;

subplot(1,3,2)
imagesc(paxis, faxis(1:v/2), abs(datafp))
xlabel('Ray parameter (1/m)', 'FontSize', 18)
ylabel('frequency (Hz)', 'FontSize', 18)
title('Ray parameter-frequency (Modulus)')
xlim([min(paxis) max(paxis)])
ylim([0 max(faxis(1:v/2))])
ax = gca;
ax.FontSize = 25;

subplot(1,3,3)
plot(paxis, R, 'k', 'linewidth', 5)
hold on
plot(paxis, m, 'r', 'linewidth', 5)
xlabel('Ray parameter (1/m)', 'FontSize', 18)
ylabel('Amplitude', 'FontSize', 18)
xlim([min(paxis) max(paxis)])
title('Modulus as function of angle')
ylim([0 1.2])
ax = gca;
ax.FontSize = 25;

end

```

E-2-3 Imaging condition

```

function [image_m_theta, image_re_theta, image_im_theta] = imaging(Gmin, Gplus, nz, dz, nx, dx, nt, dt, c1, c2, e)

% This program carried out the imaging process in the angle-frequency
% domain and produce the image of the angle-dependent reflectivity as a
% function of depth

%% Inputs
% Gmin: Upgoing Green's function in the space-time domain
% Gplus: Downgoing Green's function in the space-time domain
% nz: number of samples in the depth domain
% dz: spatial sampling in the vertical direction m
% nx: number of samples in the space domain
% dx: spatial sampling in the horizontal direction m
% nt: number of samples in the time domain
% dt: temporal sampling in s
% c1: velocity of the upper layer in m/s
% c2: velocity of the lower layer in m/s
% e: stabilization parameter (small positive constant)

%% Outputs
% image_m_theta: image of the modulus of the reflectivity
% image_re_theta: image of the real part of the reflectivity
% image_im_theta: image of the imaginary part of the reflectivity

%% The Program starts from this line

% Generate depth axis in m
zaxis=0:dz:nz*dx;

% Estimate the frequency sampling in Hz
df = 1/(nt*dt);

% Generate the frequency axis in Hz
faxis= 0:df:(nt-1)*df;

% Estimate the spatial sampling in the wavenumber-frequency domain in 1/m
dk=2*pi/(nx*dx);

% Generate the wavenumber axis in 1/m

```

```

kaxis=zeros(1,nx);
kaxis(1:(nx-1)/2+1)=-((nx-1)/2)*dk:dk:0;
kaxis((nx-1)/2+2:end)=dk:dk:((nx-1)/2)*dk;
45

for i=1:length(zaxis)
50

% Apply 2D Fourier transform
Gminfk=fftshift(fft2(Gmin{i}),2);
Gplusfk=fftshift(fft2(Gplus{i}),2);
55

divide=((data1_fk).*conj(data2_fk))./((data2_fk).*conj(data2_fk))+e);
60

% Find the size of the datafk
[v h] = size(divide);

% Estimate the angular frequency
65
omega = faxis*2*pi;

% Initiate the matrix of the angle of incidence
theta=zeros(v,h);
70

% Generate the angle axis using a linear spacing with nx
phi = linspace(-90,90,nx);

75

% Estimate the angle of incidence for every frequency
for i=1:v/2

    theta(i,:)=asind(c1*kaxis/omega(i));
80
end

% Map kx into theta using positive frequency only
85

for i=2:v/2

    % Select real part
    X = real(theta(i,:));
90

    % Select frequency contributions
    V = divide(i,:);

    % Exclude repeated angle.
    [x, index] = unique(X);
95

    dataftheta(i,:) = 2*interp1(X(index),V(index),phi,'linear','extrap');
end
100

% Estimate the modulus of the reflectivity
m=abs(sum(dataftheta)/nt);
105

% Estimate the real part of the reflectivity
re=real(sum(dataftheta)/nt);
110

% Estimate the imaginary part of the reflectivity
im=imag(sum(dataftheta)/nt);
115

% Image of the modulus
image_m_theta{i} = m;

% Image of the real part
120
image_re_theta{i} = re;

% Image of the imaginary part
image_im_theta{i} = im;
125

end
130

end

```